

# Numerical Study of Carreau Fluid Flow with Infinite Shear Rate Viscosity



By

*Humara Sardar*

Department of Mathematics  
Quaid-I-Azam University  
Islamabad, Pakistan  
2020

# Numerical Study of Carreau Fluid Flow with Infinite Shear Rate Viscosity



By

*Humara Sardar*

Supervised by

*Prof. Dr. Masood Khan*

Department of Mathematics  
Quaid-I-Azam University  
Islamabad, Pakistan  
2020

Department of Mathematics  
Quaid-I-Azam University

# **Numerical Study of Carreau Fluid Flow with Infinite Shear Rate Viscosity**

By

*Humara Sardar*

*A Thesis  
Submitted in the Partial Fulfillment of the  
Requirements for the Degree of  
DOCTOR OF PHILOSOPHY  
IN  
MATHEMATICS*

Supervised by

*Prof. Dr. Masood Khan*

**Department of Mathematics  
Quaid-I-Azam University  
Islamabad, Pakistan  
2020**

## **Author's Declaration**

I, **Humara Sardar**, hereby state that my PhD thesis titled **Numerical Study of Carreau Fluid Flow with Infinite Shear Rate Viscosity** is my own work and has not been submitted previously by me for taking any degree from the Quaid-I-Azam University Islamabad, Pakistan or anywhere else in the country/world.

At any time if my statement is found to be incorrect even after my graduate the university has the right to withdraw my PhD degree.

*Humara Sardar*

Name of Student: **Humara Sardar**

Date: **27 January, 2020**

## **Plagiarism Undertaking**

I solemnly declare that research work presented in the thesis titled “**Numerical Study of Carreau Fluid Flow with Infinite Shear Rate Viscosity**” is solely my research work with no significant contribution from any other person. Small contribution/help wherever taken has been duly acknowledged and that complete thesis has been written by me.

I understand the zero tolerance policy of the HEC and **Quaid-i-Azam University** towards plagiarism. Therefore, I as an Author of the above titled thesis declare that no portion of my thesis has been plagiarized and any material used as reference is properly referred/cited.

I undertake that if I am found guilty of any formal plagiarism in the above titled thesis even afterward of PhD degree, the University reserves the rights to withdraw/revoke my PhD degree and that HEC and the University has the right to publish my name on the HEC/University Website on which names of students are placed who submitted plagiarized thesis.

  
Student/Author Signature

Name: **Humara Sardar**

# Numerical Study of Carreau Fluid Flow with Infinite Shear Rate Viscosity

By

**Humara Sardar**

CERTIFICATE

A THESIS SUBMITTED IN THE PARTIAL FULFILLMENT OF THE  
REQUIREMENTS FOR THE DEGREE OF THE

**DOCTOR OF PHILOSOPHY IN MATHEMATICS**

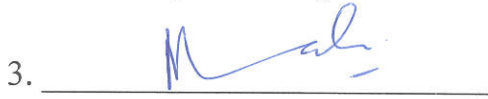
We accept this thesis as conforming to the required standard

1. 

**Prof. Dr. Sohail Nadeem**  
(Chairman)

2. 

**Prof. Dr. Masood Khan**  
(Supervisor)

3. 

**Dr. Nasir Ali**  
(External Examiner)

4. 

**Dr. Meraj Mustafa Hashmi**  
(External Examiner)

Department of Mathematics & Statistics  
International Islamic University, Sector H-10  
Islamabad.

School of Natural Sciences (SNS), National  
University of Sciences and Technology  
(NUST), Islamabad 44000 Pakistan.

**Department of Mathematics**

**Quaid-I-Azam University**

**Islamabad, Pakistan**

**2020**

## Certificate of Approval

This is to certify that the research work presented in this thesis entitled **Numerical Study of Carreau Fluid Flow with Infinite Shear Rate Viscosity** was conducted by **Ms. Humara Sardar** under the kind supervision of **Prof. Dr. Masood Khan**. No part of this thesis has been submitted anywhere else for any other degree. This thesis is submitted to the Department of Mathematics, Quaid-i-Azam University, Islamabad in partial fulfillment of the requirements for the degree of Doctor of Philosophy in field of Mathematics from Department of Mathematics, Quaid-i-Azam University Islamabad, Pakistan.

Student Name: **Humara Sardar**

Signature: Humara Sardar

External committee:

a) **External Examiner 1:**

Name: **Dr. Nasir Ali**

Designation: Associate Professor

Office Address: Department of Mathematics & Statistics, Faculty of Basic & Applied Sciences, International Islamic University, Islamabad.

Signature: Nasir Ali

b) **External Examiner 2:**

Name: **Dr. Meraj Mustafa Hashmi**

Designation: Associate Professor

Office Address: School of Natural Sciences (SNS), National University of Sciences and Technology (NUST), Islamabad 44000 Pakistan.

Signature: Meraj Hashmi

c) **Internal Examiner**

Name: **Prof. Dr. Masood Khan**

Designation: Professor

Office Address: Department of Mathematics, QAU Islamabad.

Signature: Masood Khan

**Supervisor Name:**

**Prof. Dr. Masood Khan**

Signature: Masood Khan

**Name of Dean/ HOD**

**Prof. Dr. Sohail Nadeem**

Signature: Sohail Nadeem

# *Dedication*

*To my sweet Mother*

*whose wisdom and patience will never be forgotten.*

*To my dear father*

*for their tender love and support have put me where I am now.*

*To my husband*

*for immense support and encouragements.*

*§*

*My daughters*

*For keeping my life full of joy*



# **Acknowledgement**

*All praise for **Allah**, the creator, the Glorious and the Merciful Lord, who guides me in darkness, helps me in difficulties and enables me to view stumbling blocks as stepping stones to the stars to reach the ultimate stage with courage. I am nothing without my **Allah** but I can achieve everything with His assistance. All of my veneration and devotion goes to our beloved **Prophet Hazrat Muhammad** the source of humanity, kindness and guidance for the whole creatures and who declared it an obligatory duty of every Muslim to seek and acquire knowledge. May **Allah** shower His countless blessings upon **Muhammad**, His family and companions.*

*My special thanks to **Prof. Dr. Masood Khan**, my supervisor for his cooperation, valuable instructions and beneficial remarks in the whole process of this research work. His guidance and encouragement broadened my vision of the subject. It is an honor for me to work with him. And I also want to say thanks to **Prof. Dr. Malik Muhammad Yousaf**, Ex Chairman of department of mathematics QAU for their support and guidance.*

*I wish to express my heartiest thanks and gratitude to my parents **Mr. and Mrs. Sardar Muhammad** the one who can never ever be thanked enough for the overwhelming love, kindness and care they bestow upon me. They support me financially as well as morally and without their proper guidance it would not been possible for me to complete my higher education. I would also like to thank **Mr. and Mrs. Abdul Rasheed**, my parent's in-laws, for their support.*

My deepest thanks to my husband Farooq Rasheed who supported me throughout my PhD studies. He was my wing man whose presence was the source of my strength. Thanks to my daughters Manal and Eshall, for keeping my life full of joy.

I am also thankful to each and every member of my family. Special thanks to my sister and my brother in law **Mr. and Mrs Mohsin.**

I would like to express my gratitude to respected teachers **Prof. Dr. Muhammad Ayub, Prof. Dr. Tasawar Hayat, Prof. Dr. Sohail Nadeem, Prof. Dr. Tariq Shah, Dr. Asif Ali, Dr. Khalid Saifullah, Dr. Babar Majeed Mirza, Dr. Umar Hayat and Dr. Muhammad Aslam.** These are all those people who made me what I am today, they polished me at different stages of my life and taught me whatever I am today.

For this dissertation I would like to thank my oral defense committee, **Prof. Dr. Mairaj Mustafa and Prof. Dr. Nasir Ali,** for letting my defense be an enjoyable moment, and for your brilliant comments and suggestions, thanks to you.

I gratefully acknowledge my co-advisor **Dr. Muhammad Azam** my seniors **Dr. Waqar Azeem khan, Dr. Hashim** and Ph.D fellows **Dr. Aamir Hamid, Dr Muhammad Irfan, Dr Tanzeela, Dr. Latif, Dr Maryam Subhani, Ms Nuzhat, Ms Madiha, Mr. Kaleem, Mr. Jawad Ahmed** for their brilliant ideas and important contribution in refining my research work. Their professional guidance has nourished and polished my intellectual skills and I will always remain thankful to them.

*I enact my heartiest and deepest thanks to all my lab fellows who were there in lab during my Ph.D session (03-3-2016 to 27-1-2020).*

*I am also grateful to Mr. Sheraz, Mr. Zahoor Jan, Mr. Sajid Mehmood, Mr. Muhammad Sajid, Mr. Safdar, Mr. Bilal and Mr. Irfan for their support at every time.*

*In the end thanks to all my research fellows and to those people who directly and indirectly helped me during my research work.*

***Humara Sardar***

***27-1-2020***

## ABSTRACT

A wider survey of the literature confesses that a significant attention has been given to the boundary layer flows and heat transfer analysis over the stretching surfaces. In most of these cases the fluids under consideration are Newtonian fluids. However, to the best of our knowledge very few studies have been reported on the boundary layer flows of non-Newtonian fluids. Particularly, boundary layer flow with heat and mass transfer of the Carreau fluid in the presence of infinite shear rate viscosity over the stretching surface is not being addressed properly. The study of boundary layer flows with heat and mass transfer over stretching surface is such a classic problem in fluid dynamics that it has been structured to a great extent over the years. The main aim of the research presented in this thesis is to explore and analyze the boundary layer flow of Carreau viscosity model in the presence of infinite shear rate viscosity. Additionally, the heat and mass transfer characteristics are also explored. For this purpose, boundary layer equations for steady two and three dimensional flows of Carreau fluid model in the presence of infinite shear rate viscosity have been derived.

In general the boundary layer equations of non-Newtonian fluid models are highly nonlinear and complicated. This complexity becomes more difficult when we consider the flow over complex geometries with various boundary conditions. To obtain the solutions of such problems we have employed the two different numerical schemes namely Runge-Kutta Fhelberg method along with shooting technique and Matlab built-in routine `bvp4c`. The obtained numerical results of velocity, temperature and concentration fields are presented graphically for various physical parameters. Generally the results disclose a minor dependence of the velocity, temperature and concentration distributions on the viscosity ratio parameter. It is interesting to note that the graphs of velocity and temperature disclose quite the opposite trends with uplifting viscosity ratio parameter for both shear thinning and thickening fluids. Additionally, the momentum and thermal boundary layers thickness become thick in shear thinning fluid with the increase of viscosity ratio parameter. However, quite the opposite is true for shear thickening fluid. It is further found that the temperature and concentration disclose the same trends with enhancing viscosity ratio parameter. Furthermore, graphical and tabular results are presented to verify the numerical analysis.

# Contents

<b>1</b>	<b>Introduction</b>	<b>6</b>
1.1	Research Context . . . . .	6
1.1.1	RK-Fehlberg (Runge-Kutta) Method . . . . .	12
1.1.2	MATLAB Routine (bvp4c) . . . . .	13
1.2	Basic Conservations Laws . . . . .	14
1.2.1	The Mass Conservation . . . . .	14
1.2.2	The Momentum Conservation . . . . .	15
1.2.3	The Energy Conservation . . . . .	15
1.2.4	The Concentration Conservation . . . . .	16
1.2.5	The Energy Conservation for Nanoparticles . . . . .	16
1.2.6	The Concentration Conservation for Nanoparticles . . . . .	17
1.3	The Carreau Rheological Model . . . . .	17
1.4	Objective and Contributions in this Thesis . . . . .	18
<b>2</b>	<b>Two Dimensional Carreau Fluid Flow over a Wedge with Infinite Shear Rate</b>	
	<b>Viscosity</b>	<b>21</b>
2.1	Mathematical Modelling . . . . .	22
2.2	Flow Model for Wedge . . . . .	26
2.3	Mathematical Description . . . . .	26
2.4	Friction and Heat Transport Coefficients . . . . .	29
2.5	Numerical Simulation and Validation . . . . .	30
2.6	Results and Discussion . . . . .	31

<b>3</b>	<b>Steady Two-Dimensional Flow of Carreau Nanofluid</b>	<b>41</b>
3.1	Geometry of the Physical Model . . . . .	42
3.2	Governing Problem . . . . .	42
3.2.1	Physical Parameters of Engineering Significance . . . . .	44
3.3	Solution Methodology . . . . .	45
3.4	Results and Discussion . . . . .	47
<b>4</b>	<b>Radiative Heat Transfer in Stagnation Point Flow of MHD Carreau Fluid over a Stretched Surface</b>	<b>58</b>
4.1	Description of the Problem . . . . .	59
4.1.1	Physical Parameters of Engineering Significance . . . . .	61
4.2	Solution Methodology . . . . .	62
4.3	Results and Discussion . . . . .	64
<b>5</b>	<b>On Multiple Solutions of Carreau Fluid Flow over an Inclined Shrinking Sheet</b>	<b>73</b>
5.1	Mathematical Formulation . . . . .	74
5.1.1	Engineering Parameters of Interest . . . . .	75
5.2	Numerical Method and Validation . . . . .	76
5.3	Results and Discussion . . . . .	77
<b>6</b>	<b>Dual Solutions of Carreau Nanofluid Flow over an Inclined Shrinking Sheet</b>	<b>86</b>
6.1	Geometry of the Physical Model . . . . .	87
6.2	Mathematical Formulation . . . . .	87
6.2.1	Engineering Parameters of Interest . . . . .	89
6.3	Numerical Results and Discussion . . . . .	90
6.3.1	Flow Characteristics . . . . .	90
6.3.2	Thermal characteristics . . . . .	92
6.3.3	Concentration characteristics . . . . .	93
<b>7</b>	<b>Multiple Solutions with Cattaneo–Christov Double-Diffusion Model of Carreau Fluid Flow</b>	<b>100</b>

7.1	Geometry of the Physical Model . . . . .	101
7.2	Problem Formulation . . . . .	101
7.2.1	Flow Equation . . . . .	101
7.2.2	Energy and Concentration Equations . . . . .	103
7.2.3	Engineering Parameters of Interest . . . . .	104
7.3	Results Validation and Discussion . . . . .	105
7.3.1	Validation of Numerical Outcomes . . . . .	105
7.3.2	Flow Characteristics . . . . .	106
7.3.3	Thermal Characteristics . . . . .	106
7.3.4	Concentration Characteristics . . . . .	108
<b>8</b>	<b>Heat Generation/Absorption and Thermal Radiation Impacts on Three Di-</b>	
	<b>mensional Flow of Carreau Fluid</b>	<b>115</b>
8.1	Geometry of the Physical Model . . . . .	116
8.2	Mathematical Formulation . . . . .	116
8.2.1	Parameters of Engineering Interest . . . . .	119
8.3	Validation of the Code . . . . .	119
8.4	Analysis of the Results . . . . .	120
<b>9</b>	<b>Local Non-similar Solutions of Convective Flow of Carreau Fluid</b>	<b>130</b>
9.1	Problem Statement . . . . .	131
9.2	Local Non-similar Solution Method . . . . .	133
9.2.1	Parameters of Engineering Interest . . . . .	139
9.3	Validation of Results and Discussion . . . . .	140
9.3.1	Flow and Thermal Characteristics . . . . .	140
<b>10</b>	<b>Conclusions and Future Research</b>	<b>153</b>
10.1	Conclusions . . . . .	153
10.2	Future Research Directions . . . . .	155

Nomenclature			
$(x, y)$	Cartesian coordinates	$n$	power law index
$\tau$	shear stress	$\Gamma$	relaxation parameter
$\dot{\gamma}^*$	shear rate	$\mathbf{A}_1$	Rivlin-Erickson tensor
$\mathbf{V}$	velocity field	$\mu$	apparent viscosity
$\mu_0$	zero shear rate viscosities	$\mu_\infty$	infinite shear rate viscosities
$\beta^*$	viscosity ratio parameter	$\mathbf{I}$	identity tensor
$p$	pressure	$\nu$	kinematic viscosity
$\alpha_1$	thermal diffusivity	$k$	thermal conductivity
$\rho$	fluid density	$c_p$	specific heat
$T$	temperature of fluid	$C$	nanoparticles volume fraction
$T_w$	temperature at the wall	$C_w$	concentration at the wall
$T_\infty$	ambient temperature	$C_\infty$	ambient concentration
$\tau_w$	surface shear stress	$(u, v)$	velocity components
$q_w$	wall heat flux	$U_0$	constant velocity
$q_m$	surface mass flux	$v_0$	constant suction velocity
$\psi$	stream function	$\eta$	dimensionless variable
$\beta$	wedge angle parameter	$We, We_1, We_2,$	local Weissenberg numbers
$\alpha^*$	velocity ratio parameter	$M$	magnetic parameter



$C_{fx}$	skin friction coefficient	$q_r$	radiative heat flux
$Nu_x$	Nusselt number	$\sigma^*$	stefan-Boltzman constant
$Sh_x$	local Sherwood number	$k^*$	mean absorption coefficient
$Gr_x$	Grashof number	$N_R$	thermal radiation parameter
$Re_x$	local Reynolds number	$\alpha$	inclination angle
$g$	acceleration due to gravity	Pr	Prandtl number
$\theta$	dimensionless temperature	$s$	suction parameter
$\xi$	buoyancy parameter	$Le$	Lewis number
$T_f$	temperature of hot fluid	$h_f$	heat transfer coefficient
$\sigma$	electric conductivity	$C_f$	concentration near the fluid
$D_B$	Brownian diffusion coefficient	$Nt$	thermophoresis parameter
$D_T$	thermophoresis diffusion coefficient	$Nb$	Brownian motion parameter
$\delta$	internal heat parameter	$Gr_1$ & $Gr_2$	local Grashof numbers
$\delta_e$	non dimensional thermal relaxation time	$q$	normal heat flux
$\delta_c$	non dimensional solutal relaxation time	$\lambda$	stretching/shrinking parameter
$\beta_c$	volumetric coefficient of concentration expansion	$\gamma_1$	concentration Biot number
$\theta_w$	temperature ratio parameter	$\delta_1$	velocity slip parameter
$\lambda_e$	relaxation time of heat flux	$\lambda_c$	relaxation time of mass flux
$\beta_T$	volumetric coefficient of thermal expansion	$Sc$	Schmidt number
$\beta$	volumetric coefficient of thermal expansion	$\gamma$	thermal Biot number

# Chapter 1

## Introduction

This chapter provides the motivation and literature review associated with the boundary layer flow and heat transfer involving non-Newtonian fluids. Moreover it highlights the importance of studying such fluids, especially the Carreau fluid. Additionally, a brief description of all chapters of the thesis are included in this chapter.

### 1.1 Research Context

The motivation for this thesis has been stemmed from the widespread applications of non-Newtonian fluids in industry and engineering. The main reason behind is the abundant existence of such fluids in nature as well. Non-Newtonian behavior is also used in the mining industry, where slurries and muds are often handled and in applications such as lubrication and biomedical flows. The simulation of non-Newtonian fluid flows phenomena is therefore of importance to industry. A considerable amount of work has been done in the regime of non-Newtonian fluids and much more is needed in a variety of non-Newtonian fluid models. Due to relative simplicity of the power-law model it has been studied by a number of researchers in order to investigate non-Newtonian fluid with physical effects. But the power-law model has its limitations. In view of the limitations of the power-law model, especially for very low and very high shear rates, here we consider another viscosity model known as Carreau fluid model. Carreau fluid is a type of generalized Newtonian fluids where viscosity depends upon the shear rate.

A modern rheologist, Carreau [1] in the year 1972, developed a non-Newtonian fluid model,

called Carreau fluid model. This model is an importance model of non-Newtonian fluids which is useful in chemical engineering industry and fits well with the suspensions of polymers behavior in various flow situations. It further depicts the behavior of several industrial fluids at both low and high shear rates. Moreover, four parametric Carreau model is the generalization of Newtonian fluid which has the tendency to characterize the shear thinning as well as shear thickening nature of fluid. Considering the significance of Carreau rheological model in innovative technological processes, several researchers have dedicated their time to investigate the features of such model. Tshehla [2] evaluated the flow problem past an inclined surface by taking Carreau fluid model. He further incorporated the energy equation in his study and obtained both asymptotic and numerical solutions. Olajuwon [3] estimated the convective heat transfer during the flow of an electrically conducting Carreau fluid over a vertical plate. Numerical solutions for governing problem in the presence of thermal radiation and heat generation/absorption have been computed via Runge-Kutta method. The flow of Carreau nanofluid with Ohmic heating and viscous dissipation over a non-linear stretching surface is numerically analyzed by Reddy et al. [4]. In another investigation of Carreau fluid flow past a circular cylinder by Hashim and Khan [5]. It was noted dual solutions for flow field are possible to acquire in the presence of uniform suction. In open literature, during the recent times, several researchers have evaluated the flow and heat transfer attributes of Carreau fluid, for example, Animasaun and Pop [6], Hayat *et al.* [7] and so forth.

In present era the study of nanofluid technology is used to control the heat transfer mechanism in different energy systems. The idea of nanofluids by hanging nanoparticles in base fluids to improve their thermal conductivity was presented by Choi and Eastmann [8]. It is a renowned fact that the traditional base fluids, including water, lubricants and organic fluids possess limited heat transfer characteristics due to their low thermal properties. An experimental study [9] has reported that nanofluids need only 5% volumetric fraction of the nanoparticles for an effective heat transfer enhancement. Due to recently developed technology, nanofluids encompass practical applications [10 – 12] in diverse fields inducing thermal absorption, heating and cooling processing of energy, nuclear reactor and so forth. Recently, Buongiorno [13] presented a model which includes the effect of thermophoresis and Brownian motion in the convective transport of nanofluids in boundary layer flows and developed a new correla-

tion structure (based on this explanation of the heat transfer mechanism) that can reproduce nanofluid heat transfer data responsibly well. Many researchers investigated the characteristics of nanofluids flow by incorporating the effects of Brownian motion and thermophoretic forces [14–16]. Notably, Sheikholeslami *et al.* [17] examined the MHD flow and heat transfer analysis of nanofluid by considering the natural convection and viscous dissipation. He performed the numerical simulation for the velocity and temperature distributions of nanofluid.

Researchers now a days have shown great interest in the flows of non-Newtonian liquids in the presence of magnetic field over a stretching sheet. The common examples of such magneto fluids include plasmas, salt water and electrolytes. The basic concept behind magnetohydrodynamic is that magnetic field which can induce current in a moving conductive fluid, which in turn polarizes the fluid and reciprocally changes the magnetic field itself. The pioneer work on MHD flow past a stretching surface was done by Palov [18]. After that, Andersson [19] inspected the MHD flow of a viscous fluid. Moreover few latest studies in this direction can be seen through the attempts [20–22]. Sakiadis [23] discussed the boundary layer behavior on a moving surface and he applied similarity transformations to the boundary layer equations and then numerically solved. Later on, Crane [24] simplified the work of Sakiadis.

In recent state of the art, investigations concerning the heat transfer phenomenon under the influence of thermal radiation have attracted several researchers because of its enormous applications in engineering and industrial processes. As an example, it arises in space technology, nuclear power plants, gas turbines, missiles, the chemical engineering, polymer industry and the biomedicine, etc. It is important to mention that in high temperature difference process the linear radiation is not valid because the non-dimensional parameter that is utilized as a part of the linearized Rosseland approximation is merely the effective Prandtl number. However, in case of non-linear approximation, we have three main parameters, like, Prandtl number, the temperature ratio parameter and the radiation parameter. Till date, lots of work have been done on the response of mechanism involving non-linear radiation. Cortell [25] modelled an incompressible flow of viscous liquid with heat transfer by incorporating non-linear radiation. He employed the Rosseland approximation to formulate the radiation term and obtained the numerical solutions via Runge-Kutta method. Prasad *et al.* [26] evaluated the laminar buoyancy driven flow from a spherical body with radiative heat transport phenomenon. Keller-box

method based on implicit finite difference technique is implemented to solve the governing flow problem. Sheikholeslami *et al.* [27] studied about the impacts of non-linear thermal radiation on MHD fully developed flow and heat transfer of nanofluids due to rotating plates. Lin *et al.* [28] proposed a numerical analysis to see the impact of nanoparticles shape on Marangoni boundary layer flow and heat transfer of nanofluid with thermal radiation. They studied the problem by considering five different types of nanoparticle shapes. The latest studies about flow and heat transfer with thermal radiation include the works of Atles *et al.* [29], Rashid *et al.* [30], Usman *et al.* [31] and Somro *et al.* [32], etc.

The boundary layer flows involving a variety of non-Newtonian fluids over stretching surfaces have received considerable attention in the literature. Here we provide just a brief overview of more notable studies. Initially, Mukhopadhy *et al.* [33] talked about the boundary layer flows with impact of nonlinear radiation and heat transfer characteristics across a permeable plate. Bird *et al.* [34], Gupta and Gupta [35] have studied the heat and mass transfer over stretching sheets with constant surface temperature. The boundary layer flow on an inextensible continuous flat sheet having constant velocity in a non-Newtonian power-law fluid was examined by Erickson *et al.* [36]. The classical problem of two-dimensional flow induced by a nonlinearly stretching sheet was investigated by Vajravelu [37]. Cortell [38] modified the problem by considering the nonlinear radiative heat transfer and fluid flow over a stretching sheet. In another study, Cortell [39] discussed viscous flow and heat transfer over a nonlinearly stretching sheet. Similarity solutions to viscous flow and heat transfer of nanofluid over nonlinearly stretching sheet are presented by Hamad and Ferdows [40]. Akbar *et al.* [41] found the dual solutions of MHD stagnation point flow over a Carreau fluid with shrinking sheet. Also Khan *et al.* [42] discussed the multiple solutions of slip-flow and heat transfer performance of nanofluids from a permeable shrinking surface with thermal radiation. Improvements in the study of non-Newtonian fluids have been made by different authors [43 – 46]. From the last few years, heat transfer over a shrinking sheet has a significant role due to its wide application in all most all fields of science and engineering. The most common use of shrinking sheet occur in different type of industrial processes like metallurgy and polymer industry. Another important application in engineering industry is shrinking film. If flow is induced by shrinking sheet the fluid is dragged towards a slot and consequently, it exhibits totally different physical properties from

that of a stretching sheet because of its extremely complex physical character and structure. From a physical perception, the vorticity produced at the shrinking surface is not constrained inside the boundary layer and along these lines a condition shows up where some outside forces are to be controlled. Identically, steady flow is possible only when some opposed force is applied to escape the vorticity diffusion. Hashim *et al.* [47] investigated the dual solutions in flow of a non-Newtonian fluid with homogeneous-heterogeneous reactions. Moreover, Khan *et al.* [48] discussed the dual solutions of numerical simulation for flow and heat transfer to Carreau fluid with magnetic field effect.

During the last few decades, the fluid flows across wedge shaped bodies are of fundamental importance in numerous engineering applications. It has a vital importance in the fields of geothermal industries, aerodynamics, enhanced oil recovery, heat exchangers and geothermal systems, etc. Historically, a numerous literature on Falkner and Skan flow over a static wedge can be found in the books of Gersten and Schlichting [49] and Leal [50]. In the last few years, experts have taking much interest in the Falkner-Skan flow by considering the impacts of numerous parameters. The solutions and their dependence on  $\beta$  (the wedge angle) were latterly examined by Hartree [51]. He developed the solutions and velocity profile for different approximations of pressure gradient parameter. The influence of suction/injection on forced convective wedge flow with uniform heat flux was examined by Yih [52]. His numerical study cast out that the flow separation only happens for the pressure gradient parameter  $m = 0$ . Ishaq *et al.* [53] discussed the steady 2D magnetohydrodynamic wedge flow of micropolar fluid in the presence of variable wall temperature. The study of Falkner-Skan flow of Carreau fluid over a wedge in the presence of crossed diffusion and magnetic field was investigated by Raju and Sandeep [54]. An analysis on MHD Falkner-Skan flow of Casson fluid past a wedge was also performed by Raju and Sandeep [55]. Khan and Azam [56] discussed the unsteady heat and mass transfer mechanisms in MHD Carreau nanofluid flow. Further, Khan and Azam [57] studied the unsteady Falkner-Skan flow of MHD Carreau nanofluid past a static/moving wedge with convective surface condition. Rajagopal *et al.* [58] discussed the Falkner-Skan flows of a non-Newtonian fluid. Kuo [59] discussed the application of the differential transformation method to the solutions of Falkner-Skan wedge flow. Recently, Khan and Hashim [60] explored the boundary layer flow and heat transfer to Carreau fluid over a nonlinear stretching sheet.

Additionally, Khan and Hashim [61] investigated the impact of heat transfer on Carreau fluid flow past a static/moving wedge.

A stagnation point flow happens when a flow imposes on a solid body. The initial task related to stagnation point for two dimensional flows was completed by Hiemenz [62]. Nazar *et al.* [63] studied the steady flow with two dimensional stagnation point in presence of micropolar fluid passes over a sheet. MHD stagnation point in nano-fluid in presence of non-linear radiation was discussed by Farooq *et al.* [64]. Heat transfer over a porous sheet by means of variable thermal conductivity and thermal radiation was deliberated by Cortell [65]. Furthermore, the numerical inspection of flow and heat transfer in cylindrical type axes was exposed by Lauriat and Khellaf [66]. The Carreau fluid effects with inclined sheet were discovered by Tshela [67]. Abbasi *et al.* [68] revealed the MHD Carreau fluid flow in curved channel.

Numerous aspects in boundary layer flow and heat transfer are non-similar. Non similarity related to boundary layers originate an assortment for example variety in wall temperature, variety in velocity of free-stream, suction/injection of fluid outcome at wall, surface mass transfer, outcome of buoyancy force and effects of inclination angle. The non-similarity of boundary layer can happen by in excess of one reason. There are numerous numerical techniques which are suggested to treat with such problems of non-similar boundary layers and between them; the famous technique is local non-similarity technique which is introduced by Sparrow *et al.* [69]. After them, many agents realize different problems of non-similar boundary layer. Muhaimin and Kandasamy [70] exhibited an examination tends to the magnetic effects and chemical reaction over a wedge with porosity. Chen [71] discussed the parabolic system with local non similarity method. After that, Massoudi [72] discovered the local nonsimilar solutions for the flow of a non-Newtonian fluid over a wedge.

# Numerical Methodologies

## 1.1.1 RK-Fehlberg (Runge-Kutta) Method

An investigation of numerical solution for ordinary differential equations (ODEs) has been a field of great interest within the fluid dynamics community for the past few decades. For that reasons, several authors employed various numerical procedures to tackle fluid flow behavior. Generally, many methods are available in literature for solving the initial value problems (IVPs) comprising of ODEs. Here, we present a versatile and greatly implemented integration scheme for IVPs, known as RK-Fehlberg (Runge-Kutta) method. The RK–Fehlberg is a numerical method which can be applied to solve the IVPs. Let an IVP be specified as follows

$$\frac{dz}{dx} = f(x, z), \quad z(x_0) = z_0. \quad (1.1)$$

We are interested to find an approximation to the continuously differentiable solution  $z$  of IVP (1.1) which may be the function of  $x$ . The function  $f(x, z)$  and the data  $x_0, z_0$  are known to us. The RK–Fehlberg formula is given by

$$z_{i+1} = z_i + h \left( \frac{16}{135}c_0 + \frac{6656}{12825}c_2 + \frac{28561}{56430}c_3 - \frac{9}{50}c_4 + \frac{2}{55}c_5 \right), \quad (1.2)$$

where the coefficients  $c_0$  to  $c_5$  are, respectively defined as:

$$\left. \begin{aligned} c_0 &= hf(x_i, z_i), \\ c_1 &= hf\left(x_i + \frac{1}{4}h, z_i + \frac{1}{4}c_0\right), \\ c_2 &= hf\left(x_i + \frac{3}{8}h, z_i + \frac{3}{32}c_0 + \frac{9}{32}c_1\right), \\ c_3 &= hf\left(x_i + \frac{12}{13}h, z_i + \frac{1932}{2197}c_0 - \frac{7200}{2197}c_1 + \frac{7296}{2197}c_2\right), \\ c_4 &= hf\left(x_i + h, z_i + \frac{439}{216}c_0 - 8c_1 + \frac{3860}{513}c_2 - \frac{845}{4104}c_3\right), \\ c_5 &= hf\left(x_i + \frac{1}{2}h, z_i - \frac{8}{27}c_0 + 2c_1 - \frac{3544}{2565}c_2 + \frac{1859}{4104}c_3 - \frac{11}{40}c_4\right). \end{aligned} \right\} \quad (1.3)$$

Before employing the RK–Fehlberg scheme, at a very first step, we alter the non-linear equations into a system of first order ODEs along with associated boundary conditions. The new



variables are introduced as follows:

$$f = y_1, \quad f' = y_2, \quad f'' = y_3, \quad \theta = y_4, \quad \theta' = y_5, \quad \phi = y_6, \quad \phi' = y_7. \quad (1.4)$$

### 1.1.2 MATLAB Routine (bvp4c)

The MATLAB routine `bvp4c` is a built-in technique for solving two-point boundary value problems (BVPs). This solver uses finite difference method and make use of 3-stage Labatto IIIa formula. It is a well-known fact that the BVPs are much difficult to tackle than IVPs. Hence, any solver might fail, even with good guesses for the solution and unknown parameters. The error control and mesh selection are supported by the residual of the continuous solution. As `bvp4c` is a kind of residual methods which requires some initial guess to acquire the numerical solutions. These guesses must fulfill the proposed boundary conditions. We often called this method as ‘continuation’ and the detail of this technique is provided in a book by Shampine *et al.* [73].

To implement this method, the leading equations are converted into a system of first order ODEs. This followed performs a collocation method to solve the BVP involving:

$$z'(x) = f(x, z, p), \quad a \leq x \leq b, \quad (1.5)$$

with general boundary condition (BC) given by:

$$g(z(a), z(b), p) = 0. \quad (1.6)$$

The argument  $p$  represents a vector of unknown parameters. We know that the approximated solution  $S(x)$  being a continuous function is given in the form of a third degree polynomial over each subinterval  $[x_n, x_{n+1}]$  of a mesh  $a = x_0 < x_1 < \dots < x_N = b$ . This also satisfies the given BC

$$g(S(a), S(b)) = 0. \quad (1.7)$$

With the fourth-order interpolant of `bvp4c`,  $S(x)$  further satisfies the differential equations

(collocates) at the corresponding end points and at the mid-point of these subinterval

$$S'(x_n) = f(x_n, S(x_n)), \quad (1.8)$$

$$S'((x_n + x_{n+1})/2) = f((x_n + x_{n+1})/2, S((x_n + x_{n+1})/2)), \quad (1.9)$$

$$S'(x_{n+1}) = f(x_{n+1}, S(x_{n+1})). \quad (1.10)$$

The elementary scheme of `bvp4c`, which is known as Simpson's method is renowned and present in numerous codes. As  $S(x)$  is a fourth order guess to a separate solution  $z(x)$ , i.e.,  $\|z(x) - S(x)\| \leq ch^4$ , where,  $h$  denotes the maximum of step sizes  $h_n = x_{n+1} - x_n$  and  $c$  represents a constant. After the evaluation of  $S(x)$  at a given mesh with `bvp4c`, we can estimate it at each  $x$ , or set of  $x$ , in  $[a, b]$  using `bvp4c` routine. In this routine the error estimation and mesh selection are based on the residual of  $S(x)$  defined by

$$r(x) = S'(x) - f(x, S(x)). \quad (1.11)$$

## 1.2 Basic Conservations Laws

The mechanics of fluid is highly dependent on basic conservation laws, i.e., mass, momentum, energy and concentration conservations. Mathematical formulation of these laws is given in the form of PDEs.

### 1.2.1 The Mass Conservation

According to this law, the rate of change of mass in an arbitrary material volume  $\Omega(t)$  is equal to the rate of mass production in  $\Omega(t)$ . This relation can be written as:

$$\int_{\Omega(t)} \left( \frac{\partial \rho}{\partial t} + \nabla \cdot (\rho \mathbf{V}) \right) d\Omega = 0. \quad (1.12)$$

Because this is true all  $\Omega(t)$ , so the integrand identically vanishes:

$$\frac{\partial \rho}{\partial t} + \nabla \cdot (\rho \mathbf{V}) = 0. \quad (1.13)$$

Expression (1.13) is the law of conservation of mass, also known as the continuity equation. Here  $\rho$  represents the density of fluid,  $t$  the time and  $\mathbf{V}$  the velocity field.

For an incompressible flow, we have

$$\nabla \cdot \mathbf{V} = 0. \quad (1.14)$$

This is titled as continuity equation for an incompressible flow.

### 1.2.2 The Momentum Conservation

In accordance with Newton's second law, which states that the rate of change of momentum of a material volume equals the total force on the volume. Mathematically, it is given by

$$\int_{\Omega(t)} \left[ \frac{\partial \rho \mathbf{V}_\alpha}{\partial t} + (\rho \mathbf{V}_\alpha \mathbf{V}_\beta)_{,\beta} \right] d\Omega = \int_{\Omega(t)} [\rho \mathbf{B} + \boldsymbol{\tau}_{\alpha\beta,\beta}] d\Omega. \quad (1.15)$$

We have from Eq. (1.15)

$$\frac{\partial \rho \mathbf{V}_\alpha}{\partial t} + (\rho \mathbf{V}_\alpha \mathbf{V}_\beta)_{,\beta} = \rho \mathbf{B} + \boldsymbol{\tau}_{\alpha\beta,\beta}, \quad (1.16)$$

which is the momentum conservation law. In Eq. (1.16),  $\boldsymbol{\tau}_{\alpha\beta}$  is the stress tensor and  $\mathbf{B}$  the body forces per unit volume.

In a more convenient way, the conservation of linear momentum takes the form:

$$\rho \left[ \frac{\partial \mathbf{V}}{\partial t} + (\mathbf{V} \cdot \nabla) \mathbf{V} \right] = \text{div } \boldsymbol{\tau} + \rho \mathbf{B}. \quad (1.17)$$

### 1.2.3 The Energy Conservation

In physics, the conservation of energy is originated from the first law of thermodynamics. It is mathematically composed as

$$\rho c_p \frac{dT}{dt} = \boldsymbol{\tau} \cdot \mathbf{L} - \text{div } \mathbf{q} - \text{div } \mathbf{q}_r. \quad (1.18)$$

In above expression,  $c_p$  is the specific heat of fluid and  $T$  the fluid temperature. Moreover, the left-hand side (L.H.S) of Eq. (1.18) represents internal energy, first term on the right-hand

side (R.H.S) depicts viscous dissipation and terms ( $\text{div } \mathbf{q}$  and  $\text{div } \mathbf{q}_r$ ) elucidate the thermal and radiative heat fluxes, respectively.

The energy flux  $\mathbf{q}$  is given as

$$\mathbf{q} = -k\nabla T, \quad (1.19)$$

with  $k$  denotes the fluid thermal conductivity.

#### 1.2.4 The Concentration Conservation

This law expresses that the aggregate concentration of the framework under perception remains constant. Its expression is derived by Fick's second law. In the presence of chemical reaction, it takes the form

$$\frac{\partial C}{\partial t} + (\mathbf{V} \cdot \nabla) C = -\nabla \cdot \mathbf{j} + R. \quad (1.20)$$

Here,  $C$  being the concentration of the fluid and  $\mathbf{j}$  the normal mass flux and  $R$  "source" or "sink" for  $C$ .

The normal mass flux is usually given by the Fick's first law

$$\mathbf{j} = -D\nabla C, \quad (1.21)$$

where  $D$  denotes the mass diffusivity.

#### 1.2.5 The Energy Conservation for Nanoparticles

The conservation of energy for an incompressible nanofluid are expressed as

$$\rho c_p \frac{dT}{dt} = -h_p \nabla \cdot \mathbf{j}_p - \text{div } \mathbf{q}_p. \quad (1.22)$$

In the above equation,  $\mathbf{q}_p$  be the thermal flux of nanofluids,  $h_p$  the specific enthalpy for nanofluid and  $\mathbf{j}_p$  the diffusive mass flux of nanoparticles.

Mathematical relations for  $\mathbf{q}_p$  and  $\mathbf{j}_p$  are as follows:

$$\mathbf{q}_p = -k\nabla T + h_p \mathbf{j}_p, \quad (1.23)$$

$$\mathbf{j}_p = -\rho_p D_B \nabla C - \rho_p D_T \frac{\nabla T}{T_\infty}. \quad (1.24)$$

Here,  $\rho_p$  denotes the density of nanoparticle,  $D_B$  and  $D_T$  are the Brownian and thermophoretic diffusion coefficients.

Substituting Eqs. (1.23) and (1.24) into Eq. (1.22), we have the following form of energy equation for nanofluid

$$\rho c_p \frac{dT}{dt} = k \nabla^2 T + \rho_p c_p \left[ D_B \nabla C \cdot \nabla T + D_T \frac{\nabla T \cdot \nabla T}{T_\infty} \right]. \quad (1.25)$$

### 1.2.6 The Concentration Conservation for Nanoparticles

Mathematical form of the concentration equation for nanofluid is written by

$$\frac{\partial C}{\partial t} + (\mathbf{V} \cdot \nabla) C = -\frac{1}{\rho_p} \nabla \cdot \mathbf{j}_p. \quad (1.26)$$

Making use of Eq. (1.24), we finally have

$$\frac{\partial C}{\partial t} + (\mathbf{V} \cdot \nabla) C = D_B \nabla^2 C + D_T \frac{\nabla^2 T}{T_\infty}. \quad (1.27)$$

## 1.3 The Carreau Rheological Model

In this thesis, we mainly study the flow and heat transfer problems for Carreau rheological model over different stretched geometries. The constitutive relation for apparent viscosity in Carreau fluid model is given as [4]:

$$\mu(\dot{\gamma}^*) = \mu_\infty + (\mu_0 - \mu_\infty) \left[ 1 + (\Gamma \dot{\gamma}^*)^2 \right]^{\frac{n-1}{2}}. \quad (1.28)$$

The two parameters,  $\Gamma$  and  $n$  appearing in the above relation are the relaxation time and the power-law index respectively. Additionally,  $\mu_0$  and  $\mu_\infty$  are the zero and infinite shear rate viscosities, respectively. Further, the shear rate  $\dot{\gamma}^*$  is defined by

$$\dot{\gamma}^* = \sqrt{\frac{1}{2} \sum_i \sum_j \dot{\gamma}_{ij}^* \dot{\gamma}_{ji}^*} = \sqrt{\frac{1}{2} \text{tr}(\mathbf{A}_1^2)}. \quad (1.29)$$

The Rivlin-Erickson tensor  $\mathbf{A}_1$  is written as:

$$\mathbf{A}_1 = (\text{grad } \mathbf{V}) + (\text{grad } \mathbf{V})^\top, \quad (1.30)$$

where  $\mathbf{V}$  represents the velocity field and  $\top$  denotes the transpose.

Note that the power-law index characterizes the fluid behavior and fluid is characterized as shear thinning for  $0 < n < 1$ , shear thickening for  $n > 1$ , Newtonian fluid for  $n = 1$  and/or  $\Gamma = 0$  and for large values of  $\Gamma$  the power-law model can be obtained. In the present work, we follow [96] wherein the zero and infinite shear rate viscosities were set to 1 and 0.001, respectively. Thus, the apparent viscosity  $\mu$  for Carreau fluid model can be expressed as

$$\mu = \mu_0[\beta^* + (1-\beta^*)[1 + (\Gamma\dot{\gamma}^*)^2]^{\frac{n-1}{2}}], \quad (1.31)$$

where  $\beta^* = \frac{\mu_\infty}{\mu_0}$  is the dimensionless ratio of the infinite shear-rate viscosity to the zero shear-rate viscosity and chosen to be less than unity in the present analysis.

Thus extra stress tensor is described as

$$\boldsymbol{\tau} = \mu_0[\beta^* + (1-\beta^*) \left[1 + (\Gamma\dot{\gamma}^*)^2\right]^{\frac{n-1}{2}}] \mathbf{A}_1. \quad (1.32)$$

## 1.4 Objective and Contributions in this Thesis

The purpose of this thesis is to recognize and understand the boundary layer flows of heat and mass transfer of Carreau fluid in the presence of infinite shear rate viscosity. In reality, before this commencement, there had been no current investigations concerning the Carreau fluid model along with infinite shear rate viscosity. This thesis includes ten chapters, overall covering numerous aspects of Carreau fluid in different circumstances. The foremost contributions in this thesis include the mathematical modeling and numerical simulations for the boundary layer flows concerning Carreau fluid with infinite shear rate viscosity. A generous measure of the work done in this thesis has just been published. Whatever is left of the thesis is sorted out as follows:

**Chapter 1:** This chapter comprises the motivation, background and structure of the thesis.

**Chapter 2:** The basic intent in this chapter is to formulate a mathematical model for two

dimensional Carreau fluid flow over a static/moving wedge in the presence of infinite shear rate viscosity. The governing equations of momentum and energy conservations are formulated by using the boundary layer theory. RK-Fehlberg integration scheme along with shooting technique is used for numerical computation. These findings are published in "**Results Phys.**, **8 (2018) 516 – 523**".

**Chapter 3:** In this chapter, we carried out the consequence of Carreau nano fluid flow with infinite shear rate viscosity induces by a stretching sheet. The Buongiorno's model for nanofluids which integrate the effects of Brownian motion and thermophoresis are developed. Moreover, the convective condition is utilized. The numerical results are plotted to see the impacts of leading physical parameters on the flow fields. The results of chapter 3 are published in "**Can. J. Phys.**, (2017) <https://doi.org/10.1139/cjp> – 0222".

**Chapter 4:** The motivation of this chapter is to achieve the numerical simulation of MHD Carreau fluid flow determined by a stretching sheet. In addition, the impacts of convective boundary condition and magnetic field for radiative heat transfer are analyzed. The problem becomes more complex with the addition of non-linear thermal radiation and viscous dissipation effects in the energy equation. Again RK-Fehlberg method is used solve the reduced system of ODEs. The results of this chapter are published in "**Results Phys.**, **8 (2018) 524 – 531**".

**Chapter 5:** In this chapter we consider the problem of fluid flow due to a shrinking sheet. The governing boundary layer equations are derived for a Carreau fluid flow with infinite shear rate viscosity. Here multiple solutions are obtained. Heat transfer analysis is taken to examine the thermal boundary layer. Non-dimensional variables are presented to reduce the governing equations to a systems of coupled ODEs, which are then solved by RK method. The contents of this research have been published in "**Results Phys.**, **8 (2018) 926 – 932**".

**Chapter 6:** This chapter provides dual solutions of Carreau nano fluid flow over an inclined shrinking sheet. The heat transfer analysis is studied by considering non-linear thermal radiation and heat generation/absorption at the sheet. Moreover, nano-particles with the Brownian motion and thermophoresis parameter are considered with convective boundary and new mass flux conditions. The computed results exhibit the existence of dual solutions (first and second) for both velocity and temperature fields. The consequences of this chapter have been submitted in "Physica Scripta".

**Chapter 7:** This chapter considered the characteristics of Cattaneo-Christov heat flux model involving Carreau fluid flow. In addition multiple solutions are obtained near the stagnation point flow of Carreau viscosity model by considering velocity slip at the surface. The emerging leading non-linear equations have been solved numerically by means of RK Fehlberg method. The outcomes of this chapter have been submitted in "J. Braz. Soci. Mech. Sci. Eng., (BMSE)".

**Chapter 8:** Current chapter investigates the three dimensional Carreau fluid flow. Moreover, the influences of convective boundary condition and magnetic field for radiative heat transfer are analyzed. In energy equation, non-linear thermal radiation and heat generation/absorption effects are also taken into account. The numerical technique, namely, RK-Fehlberg method is utilized to solve the reduced system of ODEs. The results of this chapter are published in "**J. Mol. Liq., 272 (2018) 474 – 480**".

**Chapter 9:** This chapter explores the local non-similar solutions of steady, MHD and mixed convective flow of Carreau fluid. In addition flow is considered near a stagnation point. Energy equation is evaluated in the presence of non-linear radiation effects. Moreover comparisons between similar and non-similar solutions are also presented. The leading PDEs of the article are converted into an organization of nonlinear ODEs by using the local non-similarity method (LNM). Moreover, final resulting non-dimensional set of coupled nonlinear ODEs are solved with the help of bvp4c function in MATLAB. The outcomes of this chapter have been published in "**J. Braz. Soci. Mech. Sci. Eng., (BMSE) 41 (69) (2019) <https://doi.org/10.1007/s40430-018-1561-2>**".

**Chapter 10:** Finally, in this chapter, the main conclusions are summarized, followed by several recommendations intended to identify future research directions.



## Chapter 2

# Two Dimensional Carreau Fluid Flow over a Wedge with Infinite Shear Rate Viscosity

This chapter investigates the steady two-dimensional flow over a moving/static wedge for a Carreau viscosity model with infinite shear rate viscosity. Additionally, heat transfer analysis is performed. Using suitable transformations, nonlinear PDEs are transformed into ODEs and solved numerically using the Runge-Kutta Fehlberg method coupled with shooting technique. The effects of various physical parameters on the velocity and temperature distributions are displayed graphically and discussed qualitatively. A comparison with the earlier reported results has been made with an excellent agreement. It is important to note that the increasing values of the wedge angle parameter enhance the fluid velocity while the opposite trend is observed for the temperature field for both shear thinning and thickening fluids. Generally, our results reveal that the velocity and temperature distributions are marginally influenced by the viscosity ratio parameter. Further, it is noted that augmented values of viscosity ratio parameter thin the momentum and thermal boundary layer thickness in shear thickening fluid and reverse is true for shear thinning fluid.

## 2.1 Mathematical Modelling

This section provides the derivation of boundary layer equations governing the steady two-dimensional flow of an incompressible Carreau fluid flow with infinite shear rate viscosity. To obtain such equations in the Cartesian coordinates  $(x, y)$ , we utilize the fundamental laws given by Eqs. (1.16) and (1.19) (cf. Chapter 1). The extra stress tensor is defined as

$$\boldsymbol{\tau} = -p\mathbf{I} + \mu\mathbf{A}_1. \quad (2.1)$$

The constitutive relation for apparent viscosity in Carreau fluid model is given as

$$\mu(\dot{\gamma}^*) = \mu_\infty + (\mu_0 - \mu_\infty) \left[ 1 + (\Gamma\dot{\gamma}^*)^2 \right]^{\frac{n-1}{2}}, \quad (2.2)$$

where  $\dot{\gamma}^*$  is defined as

$$\dot{\gamma}^* = \sqrt{\frac{1}{2} \sum_i \sum_j \dot{\gamma}_{ij}^* \dot{\gamma}_{ji}^*} = \sqrt{\frac{1}{2} \text{tr}(\mathbf{A}_1^2)}, \quad (2.3)$$

so

$$\boldsymbol{\tau} = -p\mathbf{I} + \left[ \mu_\infty + (\mu_0 - \mu_\infty) \left[ 1 + (\Gamma\dot{\gamma}^*)^2 \right]^{\frac{n-1}{2}} \right] \mathbf{A}_1, \quad (2.4)$$

or

$$\boldsymbol{\tau} = -p\mathbf{I} + \mu_0 \left[ \beta^* + (1 - \beta^*) \left[ 1 + (\Gamma\dot{\gamma}^*)^2 \right]^{\frac{n-1}{2}} \right] \mathbf{A}_1, \quad (2.5)$$

Let us assume the velocity vector as

$$\mathbf{V} = (u(x, y), v(x, y), 0). \quad (2.6)$$

The shear rate, given by Eq. (1.31) (cf. Chapter 1) in terms of velocity components becomes

$$\dot{\gamma}^* = \left[ 4 \left( \frac{\partial u}{\partial x} \right)^2 + \left( \frac{\partial u}{\partial y} + \frac{\partial v}{\partial x} \right)^2 \right]^{1/2}. \quad (2.7)$$

Upon substitution of Eq. (2.6), Eqs. (1.16) and (1.19) (cf. Chapter 1) turn into

$$\frac{\partial u}{\partial x} + \frac{\partial v}{\partial y} = 0, \quad (2.8)$$

$$\rho \left( u \frac{\partial u}{\partial x} + v \frac{\partial u}{\partial y} \right) = -\frac{\partial p}{\partial x} + \frac{\partial \tau_{xx}}{\partial x} + \frac{\partial \tau_{xy}}{\partial y}, \quad (2.9)$$

$$\rho \left( u \frac{\partial v}{\partial x} + v \frac{\partial v}{\partial y} \right) = -\frac{\partial p}{\partial y} + \frac{\partial \tau_{yx}}{\partial x} + \frac{\partial \tau_{yy}}{\partial y}, \quad (2.10)$$

where stress components  $\tau_{xx}$ ,  $\tau_{xy}$  and  $\tau_{yy}$  can be taken from Eq. (2.5).

Making use of Eqs. (1.30) (cf. Chapter 1) in (2.6) and (2.7), one can have these components in the form

$$\tau_{xx} = 2\mu_0 \frac{\partial u}{\partial x} \left[ \beta^* + (1 - \beta^*) \left[ 1 + \Gamma^2 \left\{ 4 \left( \frac{\partial u}{\partial x} \right)^2 + \left( \frac{\partial u}{\partial y} + \frac{\partial v}{\partial x} \right)^2 \right\} \right]^{\frac{n-1}{2}} \right], \quad (2.11)$$

$$\tau_{xy} = \tau_{yx} = \mu_0 \left( \frac{\partial u}{\partial y} + \frac{\partial v}{\partial x} \right) \left[ \beta^* + (1 - \beta^*) \left[ 1 + \Gamma^2 \left\{ 4 \left( \frac{\partial u}{\partial x} \right)^2 + \left( \frac{\partial u}{\partial y} + \frac{\partial v}{\partial x} \right)^2 \right\} \right]^{\frac{n-1}{2}} \right], \quad (2.12)$$

$$\tau_{yy} = 2\mu_0 \frac{\partial v}{\partial x} \left[ \beta^* + (1 - \beta^*) \left[ 1 + \Gamma^2 \left\{ 4 \left( \frac{\partial u}{\partial x} \right)^2 + \left( \frac{\partial u}{\partial y} + \frac{\partial v}{\partial x} \right)^2 \right\} \right]^{\frac{n-1}{2}} \right]. \quad (2.13)$$

Invoking Eqs. (2.11) – (2.13) into Eqs. (2.9) and (2.10), a straightforward calculation yields the following governing equations:

$$\begin{aligned} & \rho \left( u \frac{\partial u}{\partial x} + v \frac{\partial u}{\partial y} \right) = -\frac{\partial p}{\partial x} \\ & + \mu_0 \left( \frac{\partial^2 u}{\partial x^2} + \frac{\partial^2 u}{\partial y^2} \right) \left[ \beta^* + (1 - \beta^*) \left[ 1 + \Gamma^2 \left\{ 4 \left( \frac{\partial u}{\partial x} \right)^2 + \left( \frac{\partial u}{\partial y} + \frac{\partial v}{\partial x} \right)^2 \right\} \right]^{\frac{n-1}{2}} \right] \\ & + \mu_0 \left( \frac{\partial u}{\partial y} + \frac{\partial v}{\partial x} \right) \frac{\partial}{\partial y} \left[ \beta^* + (1 - \beta^*) \left[ 1 + \Gamma^2 \left\{ 4 \left( \frac{\partial u}{\partial x} \right)^2 + \left( \frac{\partial u}{\partial y} + \frac{\partial v}{\partial x} \right)^2 \right\} \right]^{\frac{n-1}{2}} \right] \\ & + 2\mu_0 \frac{\partial u}{\partial x} \frac{\partial}{\partial x} \left[ \beta^* + (1 - \beta^*) \left[ 1 + \Gamma^2 \left\{ 4 \left( \frac{\partial u}{\partial x} \right)^2 + \left( \frac{\partial u}{\partial y} + \frac{\partial v}{\partial x} \right)^2 \right\} \right]^{\frac{n-1}{2}} \right], \end{aligned} \quad (2.14)$$

$$\begin{aligned}
& \rho \left( u \frac{\partial v}{\partial x} + v \frac{\partial v}{\partial y} \right) = -\frac{\partial p}{\partial y} \\
& +\mu_0 \left( \frac{\partial^2 v}{\partial x^2} + \frac{\partial^2 v}{\partial y^2} \right) \left[ \beta^* + (1 - \beta^*) \left[ 1 + \Gamma^2 \left\{ 4 \left( \frac{\partial u}{\partial x} \right)^2 + \left( \frac{\partial u}{\partial y} + \frac{\partial v}{\partial x} \right)^2 \right\} \right]^{\frac{n-1}{2}} \right] \\
& +\mu_0 \left( \frac{\partial u}{\partial y} + \frac{\partial v}{\partial x} \right) \frac{\partial}{\partial x} \left[ \beta^* + (1 - \beta^*) \left[ 1 + \Gamma^2 \left\{ 4 \left( \frac{\partial u}{\partial x} \right)^2 + \left( \frac{\partial u}{\partial y} + \frac{\partial v}{\partial x} \right)^2 \right\} \right]^{\frac{n-1}{2}} \right] \\
& +2\mu_0 \frac{\partial v}{\partial y} \frac{\partial}{\partial y} \left[ \beta^* + (1 - \beta^*) \left[ 1 + \Gamma^2 \left\{ 4 \left( \frac{\partial u}{\partial x} \right)^2 + \left( \frac{\partial u}{\partial y} + \frac{\partial v}{\partial x} \right)^2 \right\} \right]^{\frac{n-1}{2}} \right]. \tag{2.15}
\end{aligned}$$

In order to convert these equations into non-dimensional form, let us use the Boussines approximations by assuming  $L$  and  $U$  as characteristics length and velocity. The following non-dimensional quantities are considered

$$u = Uu^*, \quad v = Uv^*, \quad x = Lx^*, \quad y = Ly^* \quad \text{and} \quad p = \rho U^2 p^*. \tag{2.16}$$

In view of non-dimensional quantities (2.16), we can formulate the momentum transport equation as:

$$\begin{aligned}
& u^* \frac{\partial u^*}{\partial x^*} + v^* \frac{\partial u^*}{\partial y^*} = -\frac{\partial p^*}{\partial x^*} \\
& +\epsilon_1 \left( \frac{\partial^2 u^*}{\partial x^{*2}} + \frac{\partial^2 u^*}{\partial y^{*2}} \right) \left[ \beta^* + (1 - \beta^*) \left[ 1 + \epsilon_2 \left\{ 4 \left( \frac{\partial u^*}{\partial x^*} \right)^2 + \left( \frac{\partial u^*}{\partial y^*} + \frac{\partial v^*}{\partial x^*} \right)^2 \right\} \right]^{\frac{n-1}{2}} \right] \\
& +2\epsilon_1 \frac{\partial u^*}{\partial x^*} \frac{\partial}{\partial x^*} \left[ \beta^* + (1 - \beta^*) \left[ 1 + \epsilon_2 \left\{ 4 \left( \frac{\partial u^*}{\partial x^*} \right)^2 + \left( \frac{\partial u^*}{\partial y^*} + \frac{\partial v^*}{\partial x^*} \right)^2 \right\} \right]^{\frac{n-1}{2}} \right] \\
& +\epsilon_1 \left( \frac{\partial u^*}{\partial y^*} + \frac{\partial v^*}{\partial x^*} \right) \frac{\partial}{\partial y^*} \left[ \beta^* + (1 - \beta^*) \left[ 1 + \epsilon_2 \left\{ 4 \left( \frac{\partial u^*}{\partial x^*} \right)^2 + \left( \frac{\partial u^*}{\partial y^*} + \frac{\partial v^*}{\partial x^*} \right)^2 \right\} \right]^{\frac{n-1}{2}} \right], \tag{2.17}
\end{aligned}$$

$$\begin{aligned}
& u^* \frac{\partial v^*}{\partial x^*} + v^* \frac{\partial v^*}{\partial y^*} = -\frac{\partial p^*}{\partial y^*} \\
& + \epsilon_1 \left( \frac{\partial^2 v^*}{\partial x^{*2}} + \frac{\partial^2 v^*}{\partial y^{*2}} \right) \left[ \beta^* + (1 - \beta^*) \left[ 1 + \epsilon_2 \left\{ 4 \left( \frac{\partial u^*}{\partial x^*} \right)^2 + \left( \frac{\partial u^*}{\partial y^*} + \frac{\partial v^*}{\partial x^*} \right)^2 \right\} \right]^{\frac{n-1}{2}} \right] \\
& + 2\epsilon_1 \frac{\partial v^*}{\partial y^*} \frac{\partial}{\partial y^*} \left[ \beta^* + (1 - \beta^*) \left[ 1 + \epsilon_2 \left\{ 4 \left( \frac{\partial u^*}{\partial x^*} \right)^2 + \left( \frac{\partial u^*}{\partial y^*} + \frac{\partial v^*}{\partial x^*} \right)^2 \right\} \right]^{\frac{n-1}{2}} \right] \\
& + \epsilon_1 \left( \frac{\partial u^*}{\partial y^*} + \frac{\partial v^*}{\partial x^*} \right) \frac{\partial}{\partial x^*} \left[ \beta^* + (1 - \beta^*) \left[ 1 + \epsilon_2 \left\{ 4 \left( \frac{\partial u^*}{\partial x^*} \right)^2 + \left( \frac{\partial u^*}{\partial y^*} + \frac{\partial v^*}{\partial x^*} \right)^2 \right\} \right]^{\frac{n-1}{2}} \right], \quad (2.18)
\end{aligned}$$

where the dimensionless variables  $\epsilon_1$  and  $\epsilon_2$  are defined by

$$\epsilon_1 = \frac{\mu_0/\rho}{LU} \quad \text{and} \quad \epsilon_2 = \frac{\Gamma^2}{(L/U)^2}. \quad (2.19)$$

In agreement with the Boussines approximations, we can assume that  $O(u, x) = 1$  and  $O(v, y) = \delta$ . Furthermore, the dimensionless parameter  $\epsilon_1$  and  $\epsilon_2$  have orders  $\delta^2$ , i.e.,  $O(\epsilon_1, \epsilon_2) = \delta^2$ .

Consequently, the boundary layer Eqs. (2.17) and (2.18) are written as

$$\begin{aligned}
& u^* \frac{\partial u^*}{\partial x^*} + v^* \frac{\partial u^*}{\partial y^*} = -\frac{\partial p^*}{\partial x^*} + \epsilon_1 \frac{\partial^2 u^*}{\partial y^{*2}} \left[ \beta^* + (1 - \beta^*) \left[ 1 + \epsilon_2 \left( \frac{\partial u^*}{\partial y^*} \right)^2 \right]^{\frac{n-1}{2}} \right] \\
& + \epsilon_1 \frac{\partial u^*}{\partial y^*} \frac{\partial}{\partial y^*} \left[ \beta^* + (1 - \beta^*) \left[ 1 + \epsilon_2 \left( \frac{\partial u^*}{\partial y^*} \right)^2 \right]^{\frac{n-1}{2}} \right], \quad (2.20)
\end{aligned}$$

$$0 = -\frac{\partial p^*}{\partial y^*}. \quad (2.21)$$

Thus, Eqs. (2.20) and (2.21) seize their new dimensional form:

$$\begin{aligned}
& u \frac{\partial u}{\partial x} + v \frac{\partial u}{\partial y} = -\frac{1}{\rho} \frac{\partial p}{\partial x} + \nu \frac{\partial^2 u}{\partial y^2} \left[ \beta^* + (1 - \beta^*) \left[ 1 + \Gamma^2 \left( \frac{\partial u}{\partial y} \right)^2 \right]^{\frac{n-1}{2}} \right] \\
& + \nu \frac{\partial u}{\partial y} \frac{\partial}{\partial y} \left[ \beta^* + (1 - \beta^*) \left[ 1 + \Gamma^2 \left( \frac{\partial u}{\partial y} \right)^2 \right]^{\frac{n-1}{2}} \right], \quad (2.22)
\end{aligned}$$

$$0 = -\frac{1}{\rho} \frac{\partial p}{\partial y}, \quad (2.23)$$

where  $\nu = \mu_0/\rho$  is the kinematic viscosity.

The above equation in simplified form is

$$\begin{aligned}
 u \frac{\partial u}{\partial x} + v \frac{\partial u}{\partial y} = & -\frac{1}{\rho} \frac{\partial p}{\partial x} + \nu \frac{\partial^2 u}{\partial y^2} \left[ \beta^* + (1 - \beta^*) \left[ 1 + \Gamma^2 \left( \frac{\partial u}{\partial y} \right)^2 \right]^{\frac{n-1}{2}} \right] \\
 & + \nu(n-1)(1-\beta^*)\Gamma^2 \left( \frac{\partial u}{\partial y} \right)^2 \left( \frac{\partial^2 u}{\partial y^2} \right) \left[ 1 + \Gamma^2 \left( \frac{\partial u}{\partial y} \right)^2 \right]^{\frac{n-3}{2}}. \quad (2.24)
 \end{aligned}$$

## 2.2 Flow Model for Wedge

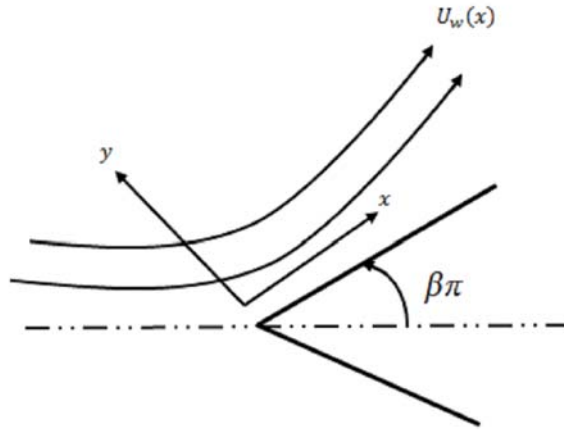


**Fig. 2.1:** The flow geometry of the physical system.

## 2.3 Mathematical Description

Here we have considered the laminar, steady two-dimensional flow of an incompressible Carreau viscosity fluid model past a static/moving wedge as shown through **Fig. 2.1**. We supposed that fluid flow is induced by the stretching wedge with velocity  $U_w(x) = bx^m$  while the free stream velocity is  $U_e(x) = cx^m$ , where  $b, c$  and  $m$  are positive constants. Further  $U_w(x) > 0$  shows

the stretching wedge surface velocity and  $U_w(x) < 0$  for constructing wedge surface velocity. The wedge angle is assumed to be  $\Omega = \beta\pi$ , where  $\beta = \frac{2m}{m+1}$  is related to the pressure gradient. It is anticipated that the surface temperature  $T_w(x)$  at the sheet considered to be higher than the ambient fluid temperature  $T_\infty$  ( $T_w > T_\infty$ ).

On the basis of above assumptions and usual boundary layer approximations, Eq. (1.14), Eqs. (1.15) and (1.18) turn into:

$$\frac{\partial u}{\partial x} + \frac{\partial v}{\partial y} = 0, \quad (2.25)$$

$$u \frac{\partial u}{\partial x} + v \frac{\partial u}{\partial y} = U_e \frac{dU_e}{dx} + \nu \left( \frac{\partial^2 u}{\partial y^2} \right) \left[ \beta^* + (1-\beta^*) \left\{ 1 + \Gamma^2 \left( \frac{\partial u}{\partial y} \right)^2 \right\}^{\frac{n-1}{2}} \right] + \nu(n-1)(1-\beta^*)\Gamma^2 \left( \frac{\partial^2 u}{\partial y^2} \right) \left( \frac{\partial u}{\partial y} \right)^2 \left\{ 1 + \Gamma^2 \left( \frac{\partial u}{\partial y} \right)^2 \right\}^{\frac{n-3}{2}}, \quad (2.26)$$

$$u \frac{\partial T}{\partial x} + v \frac{\partial T}{\partial y} = \alpha_1 \frac{\partial^2 T}{\partial y^2}, \quad (2.27)$$

and the related boundary conditions for the present problem are:

(1) static wedge

$$u = 0, \quad v = 0, \quad T = T_w \quad \text{at} \quad y = 0, \quad (2.28)$$

$$u = U_e(x) = cx^m, \quad T \rightarrow T_\infty \quad \text{as} \quad y \rightarrow \infty, \quad (2.29)$$

(2) moving wedge

$$u = U_w(x) = bx^m, \quad v = 0, \quad T = T_w \quad \text{at} \quad y = 0, \quad (2.30)$$

$$u = U_e(x) = cx^m, \quad T \rightarrow T_\infty \quad \text{as} \quad y \rightarrow \infty. \quad (2.31)$$

Here  $\nu$  is the kinematic viscosity,  $\alpha_1 = \frac{k}{\rho c_p}$  the thermal diffusivity with  $c_p$  the specific heat,  $k$  the thermal conductivity and  $T$  the temperature of the fluid.

Now we introduced the following suitable transformations:

$$\eta = y\sqrt{\frac{c(m+1)}{2\nu}}x^{\frac{m-1}{2}}, \quad \Psi(x, y) = \sqrt{\frac{2\nu c}{m+1}}x^{\frac{m+1}{2}}f(\eta), \quad \theta(\eta) = \frac{T - T_\infty}{T_w - T_\infty}, \quad (2.32)$$

where  $\Psi$  denotes the stream function that satisfies equation of continuity with  $u = \frac{\partial\Psi}{\partial y}$  and  $v = -\frac{\partial\Psi}{\partial x}$  which are defined as

$$u = cx^m f'(\eta),$$

$$v = -\sqrt{\frac{2\nu c}{m+1}}\left(\frac{m+1}{2}\right)x^{\frac{m-1}{2}}f(\eta) - c\left(\frac{m-1}{2}\right)yx^{m-1}f'(\eta), \quad (2.33)$$

Thus the transformed non-linear momentum and energy equations can be described as:

$$\left[\beta^* + (1 - \beta^*) \left\{1 + We^2(f'')^2\right\}^{\frac{n-3}{2}} \left\{1 + nWe^2(f'')^2\right\}\right] f'''$$

$$+ ff'' + \beta \left[1 - (f')^2\right] = 0, \quad (2.34)$$

$$\theta'' + Pr f\theta' = 0, \quad (2.35)$$

with related BCs

$$f(0) = 0, \quad f'(0) = \lambda, \quad \theta(0) = 1, \quad (2.36)$$

$$f'(\infty) \rightarrow 1, \quad \theta(\infty) \rightarrow 0. \quad (2.37)$$

In the above equations, prime denotes the differentiation with respect to variable  $\eta$ ,  $\beta^* = \left(\frac{\mu_\infty}{\mu_0}\right)$  the viscosity ratio parameter with  $\mu_0$  the zero shear rate viscosity and  $\mu_\infty$  the infinite shear rate viscosity and chosen to be less than one in present study,  $We$  the Weissenberg number,  $\lambda$  the stretching/shrinking parameter and  $Pr$  the Prandtl number. These quantities are defined as follows:



$$\beta^* = \frac{\mu_\infty}{\mu_0}, \quad We^2 = \left( c^2 \Gamma^2 \text{Re}_L \frac{(m+1)}{2L^{m+1}} x^{3m-1} \right), \quad \text{Re}_L = \frac{cL^{m+1}}{\nu},$$

$$\Gamma = \Gamma_0 \left( \frac{x}{L} \right)^{\frac{1-3m}{2}}, \quad \lambda = \frac{b}{c}, \quad Pr = \frac{\mu c_p}{k}. \quad (2.38)$$

Here positive values of  $\beta$  show the favorable pressure gradient and negative values of  $\beta$  reveal an opposing pressure gradient. Additionally,  $m = 0$  i.e ( $\beta = 0$ ) implies the fluid flow past a flat plate and  $m = 1$ , i.e, ( $\beta = 1$ ) means the stagnation point flow. Moreover the constant velocity ratio parameter  $\lambda > 0$  and  $\lambda < 0$  classify with a moving wedge in the same and opposite directions to the free stream, respectively; however,  $\lambda = 0$  is related to a static wedge.

## 2.4 Friction and Heat Transport Coefficients

The parameters of engineering interest in the flow and heat transfer problem are the local skin friction coefficient  $C_{fx}$  and the local Nusselt number  $Nu_x$ , characterizing the surface drag and wall heat transfer rate, can be defined as:

$$C_{fx} = \frac{\tau_w}{\rho U_w^2(x)/2}, \quad Nu_x = \frac{xq_w}{k(T_w - T_\infty)}, \quad (2.39)$$

where  $\tau_w$  is the surface shear stress and  $q_w$  the surface heat flux given by

$$\tau_w = \mu_0 \left( \frac{\partial u}{\partial y} \right) \left[ \beta^* + (1-\beta^*) \left\{ 1 + \Gamma^2 \left( \frac{\partial u}{\partial y} \right)^2 \right\}^{\frac{n-1}{2}} \right] \Big|_{y=0}, \quad q_w = -k \left( \frac{\partial T}{\partial y} \right) \Big|_{y=0}. \quad (2.40)$$

Upon using Eq. (2.39), the local skin friction coefficient and local Nusselt number become

$$\text{Re}^{1/2} C_{fx} = \frac{2}{\sqrt{2-\beta}} f''(0) \left[ \beta^* + (1-\beta^*) \left\{ 1 + We^2 (f''(0))^2 \right\}^{\frac{n-1}{2}} \right], \quad (2.41)$$

$$\text{Re}^{-1/2} Nu_x = -\frac{2}{\sqrt{2-\beta}} \theta'(0). \quad (2.42)$$

where  $\text{Re} = \frac{U_w x}{\nu}$  is the local Reynolds number.

## 2.5 Numerical Simulation and Validation

The system of governing equations (Eqs. (2.34) and (2.35)) is highly nonlinear and partially set of coupled ordinary differential equations. To discover the solution of this system along with boundary conditions (2.36) – (2.37), the shooting technique along with fourth order Runge–Kutta integration scheme is developed. Since Runge–Kutta Fehlberg method solves only initial value problem, and so Eqs. (2.34) and (2.35) are converted into set of first order equations. For this purpose, we rewrite the above set of equations as given below:

$$f''' = \frac{-\beta \left(1 - (f')^2\right) - f f''}{\left[\beta^* + (1 - \beta^*) \{1 + nW e^2 (f'')^2\} \{1 + W e^2 (f'')^2\}^{\frac{n-3}{2}}\right]}, \quad (2.43)$$

$$\theta'' = -\text{Pr} f \theta'. \quad (2.44)$$

The new variables defined below are employed to reduce the above higher order equations into system of first order differential equations:

$$\begin{aligned} f &= y_1, \quad f' = y_2, \quad f'' = y_3, \quad f''' = y_3', \\ \theta &= y_4, \quad \theta' = y_5, \quad \theta'' = y_5'. \end{aligned} \quad (2.45)$$

After inserting Eq. (2.45) into Eqs. (2.43) and (2.44), a new system of ordinary differential equations is obtained as:

$$y_1' = y_2, \quad y_2' = y_3, \quad y_3' = \frac{[-\beta (1 - y_2^2) - y_1 y_3]}{\beta^* + (1 - \beta^*) [1 + nW e^2 y_3^2] [1 + W e^2 y_3^2]^{\frac{n-3}{2}}}, \quad (2.46)$$

$$y_4' = y_5, \quad y_5' = -\text{Pr} y_1 y_5. \quad (2.47)$$

together with the boundary conditions

$$\begin{pmatrix} y_1 \\ y_2 \\ y_3 \\ y_4 \\ y_5 \end{pmatrix} = \begin{pmatrix} 0 \\ \lambda \\ u_1 \\ 1 \\ u_5 \end{pmatrix}. \quad (2.48)$$

The above system of equations is solved with shooting method, the following procedure is utilized:

1. Firstly choose the limit of  $\eta_\infty$  the best suited limit for  $\eta_\infty$  is between 5 to 10.
2. Then select suitable initial guesses for  $y_3(0)$  and  $y_5(0)$ . Initially  $y_3(0) = -1$  and  $y_5(0) = 0.5$  are selected.
3. Then set of ODEs are solved with the fourth order Runge–Kutta Fehlberg scheme.
4. Finally, boundary residuals (absolute variations in given and calculated values of  $y_2(\infty)$  and  $y_5(\infty)$ ) is calculated. The solution will converge if the entire values of boundary residuals are less than tolerance error, which is considered  $10^{-5}$ .
5. If values of boundary residuals are larger than tolerance error, then values of  $y_3(0)$  and  $y_5(0)$  will be modified by Newton’s method.

## 2.6 Results and Discussion

This section is simply devoted to exploring the effects of various physical parameters on fluid velocity and temperature. For this purpose, the numerical results are presented graphically to illustrate their physical characteristics.

In order to examine results of the present problem a detailed numerical computation is performed for steady two dimensional flow of Carreau viscosity model generated by a static/moving wedge. The partially coupled set of Eqs. (2.34) – (2.35) with boundary conditions (2.36) and (2.37) are solved numerically using Runge-Kutta fourth order method along with shooting technique. Moreover, representative results for the skin friction and Nusselt number are recorded through tables. The influence of non-dimensional parameters like  $We$ ,  $\lambda$ ,  $n$ ,  $\beta$ ,

$\beta^*$  and  $Pr$  on dimensionless fluid velocity and temperature distribution are determined and presented through graphs. Additionally, the accuracy of our numerical results is verified with earlier published results by Rajgopal *et al.* [58] and Kuo [59] for particular through **Table 2.1**. The good agreement is reported between these results.

**Figs. 2.2** are plotted to examine the influence of velocity ratio parameter  $\lambda$  on temperature  $\theta(\eta)$  and velocity  $f'(\eta)$  profiles, for both shear thickening ( $n > 1$ ) and shear thinning ( $n < 1$ ) fluids. Here temperature and velocity profiles are presented for two different values of  $\beta$ . In detail,  $\beta = 0$  means wedge angle of zero degree relates to the flow over a flat plate and  $\beta = 1$  relates the wedge point of  $90^\circ$ , i.e; stagnation point flow. From **Figs. 2.2(a, b)**, we observed that the fluid velocity is enhanced by uplifting values of the velocity ratio parameter for both cases. Also it is observed that when flow is near the stagnation-point, the velocity profiles are closer to each other. However, these **Figs.** show that the thickness of the momentum boundary layer for shear thickening fluid is higher as compared with shear thinning fluid. **Figs. 2.2(c, d)** depict that by increasing values of the velocity ratio parameter, temperature profile decreases in both cases, i.e., for shear thinning as well as shear thickening fluids. The thermal boundary layer thickness reduces for both the flow over flat plate and near the stagnation-point. However, the temperature profiles are closer to each other if flow is near to the stagnation-point and the thermal boundary layer thickness is higher for shear thickening fluid.

**Figs. 2.3** are designed to observe the effects of the wedge angle parameter  $\beta$  on the velocity  $f'(\eta)$  and temperature  $\theta(\eta)$  profiles in shear thinning and shear thickening fluids. From **Figs. 2.3(a, b)** we observed that the fluid velocity is enhanced by increasing wedge angle parameter in both cases. Physically, it is due to the wedge angle parameter that is related with pressure gradient. Thus, positive values of the wedge angle parameter indicate a favorable pressure gradient which enhance the flow. Further for positive values of  $\beta$  the velocity profile goes nearer to the surface of the wedge, and opposite flow does not occur. Moreover, the momentum boundary layer thickness reduces by increasing wedge angle parameter and then again it is higher in case of shear thickening fluid. **Figs. 2.3(c, d)** describe the impact of the wedge angle parameter on temperature distribution. We observed that the fluid temperature is diminished with increasing the wedge angle parameter. Moreover, the maximum temperature of the fluid occurs for the flow over flat plate ( $\beta = 0$ ). Physically, it is due to the fluid motion i.e., pressure

gradient is zero and due to that fluid temperature increases at the surface of wedge. In the case of static wedge the thermal boundary layer thickness is higher.

**Figs. 2.4** describe the impact of viscosity ratio parameter  $\beta^*$  on velocity and temperature profiles for both shear thinning and thickening cases. Here, profiles are presented for two different values of wedge angle parameter. Here  $\beta = 0$  (wedge of zero degree) and  $\beta = 1$  (wedge point of  $90^\circ$ ). We observe a minor dependence of velocity and temperature distributions on  $\beta^*$ . However, it is interesting to note that graph of velocity and temperature disclose quite the opposite trends with uplifting  $\beta^*$  for the shear thinning and shear thickening fluids. Additionally, these **Figs.** portray that the momentum and thermal layers thickness become thick in shear thinning fluid as we increase the viscosity ratio parameter and quite the opposite is true for shear thickening fluid. **Figs. 2.5** show the impact of viscosity ratio parameter  $\beta^*$  on the velocity and temperature profiles for both shear thinning and thickening cases with two different values of  $\lambda$ . Here  $\lambda = 0$  (static wedge) and  $\lambda > 0$  and  $\lambda < 0$  show the moving wedge in same and inverse directions, respectively. We observe again a little dependence of the velocity and temperature distributions on  $\beta^*$ . Qualitatively, the effects of  $\beta^*$  on the velocity and temperature distributions are same as that of **Figs. 2.4**.

**Figs. 2.6** is a plot of the variation in the temperature distribution for various values of the Weissenberg number  $We$  and Prandtl number  $Pr$  for both shear thinning and shear thickening fluids. These **Figs.** exhibit that the temperature and thermal boundary layer thickness reduce by uplifting the values of  $We$  and  $Pr$  in both shear thinning and shear thickening fluids. Moreover, it can be observed that the maximum difference between the temperature profiles occurs at smaller values of  $Pr$  and it reduces as  $Pr$  increases.

**Table 2.1** is created to prove the authenticity of the given numerical results with the previous published data for shear thinning ( $0 < n < 1$ ) and shear thickening ( $n > 1$ ) fluids and found to be in outstanding agreement.

**Table 2.2** is created to exhibit the influence of the viscosity ratio parameter  $\beta^*$ , velocity ratio parameter  $\lambda$  and wedge angle parameter  $\beta$  on the local skin friction coefficient for both shear thinning and thickening cases. On the basis of this table it is noticed that the skin friction coefficient is decreasing function for the wedge angle parameter and velocity ratio parameter in both cases. It is also observed that the skin friction coefficient is a decreasing function for the

viscosity ratio parameter in shear thinning case and reverse is true for shear thickening case.

**Table 2.3** is constructed to depict the impact of the viscosity ratio parameter  $\beta^*$ , velocity ratio parameter  $\lambda$  and wedge angle parameter  $\beta$  on the Nusselt number for both cases when  $Pr = 1$  and  $We = 3$ . It is observed that the Nusselt number is a decreasing function for velocity ratio parameter and viscosity ratio parameter in both shear thinning and shear thickening cases. It is further discovered that the Nusselt number increasing function for the viscosity ratio parameter in shear thinning case and reverse is true for shear thickening case.

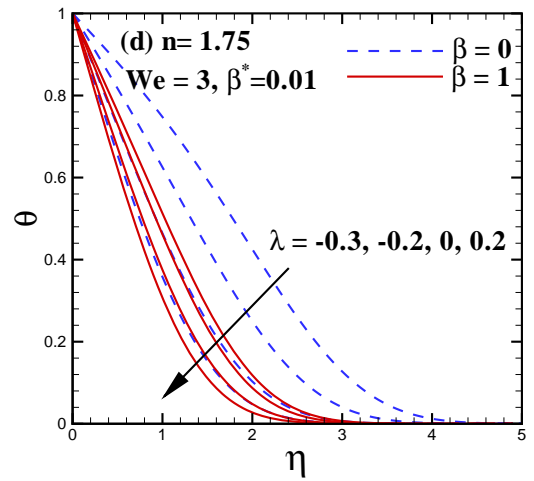
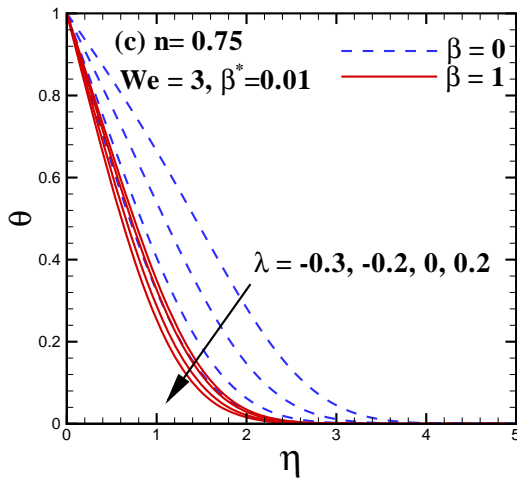
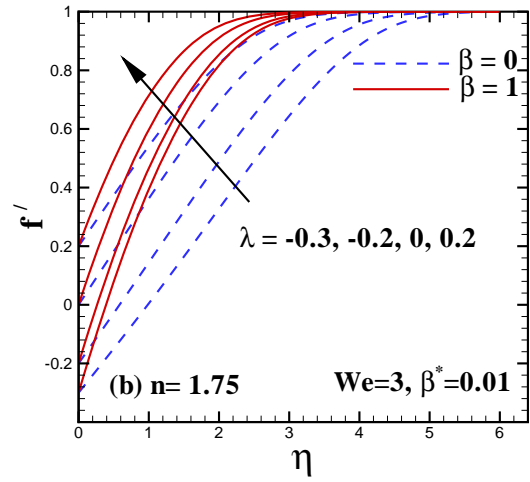
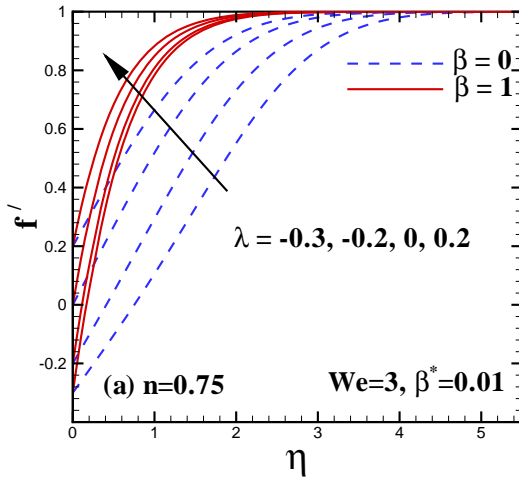


**Fig. 2.2:** Simulated velocity  $f'(\eta)$  and temperature  $\theta(\eta)$  profiles for  $\lambda$  when  $We = 3.0$ .

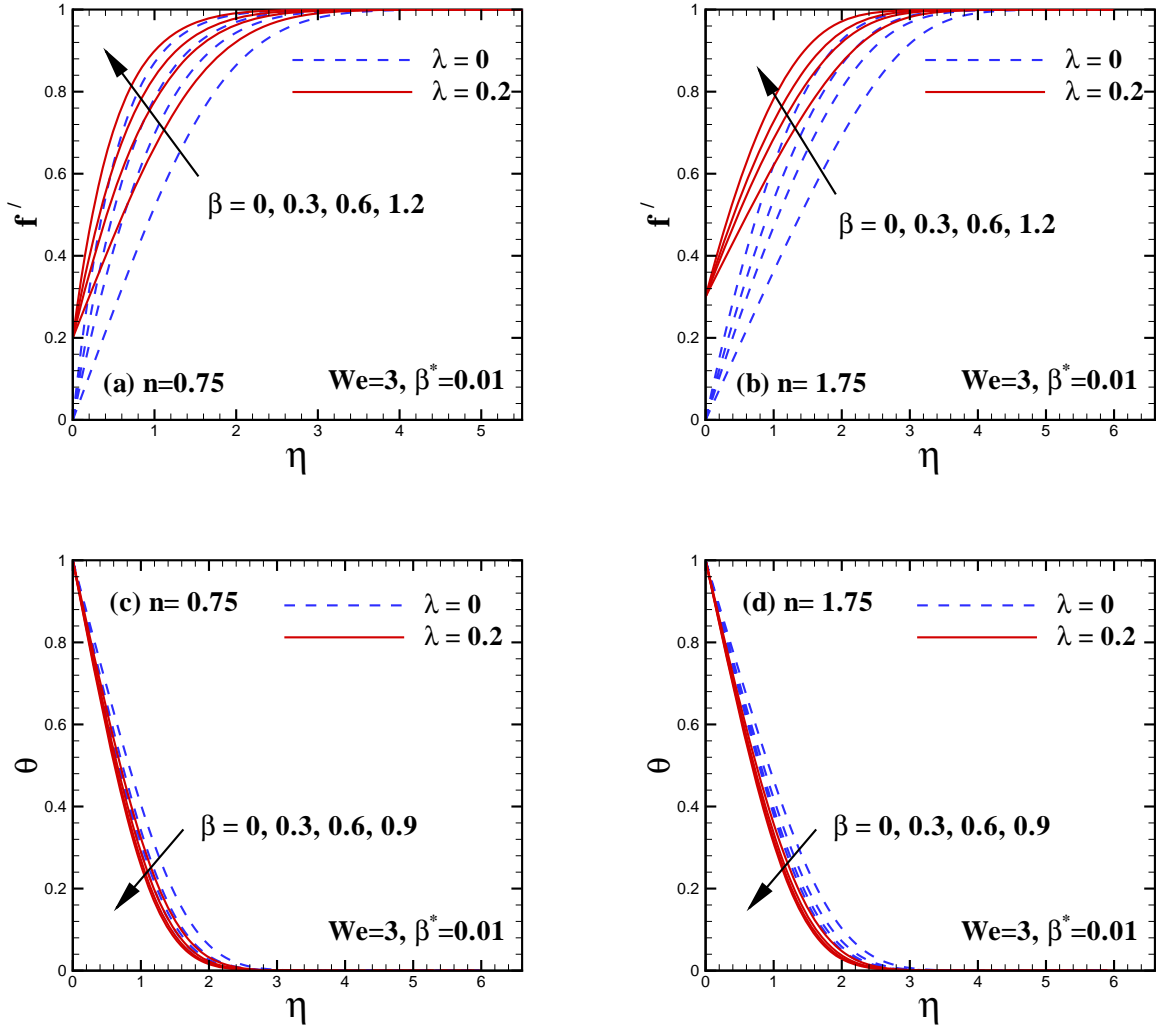


**Fig. 2.3:** Simulated velocity  $f'(\eta)$  and temperature  $\theta(\eta)$  profiles for  $\beta$ , when  $We = 3$ .

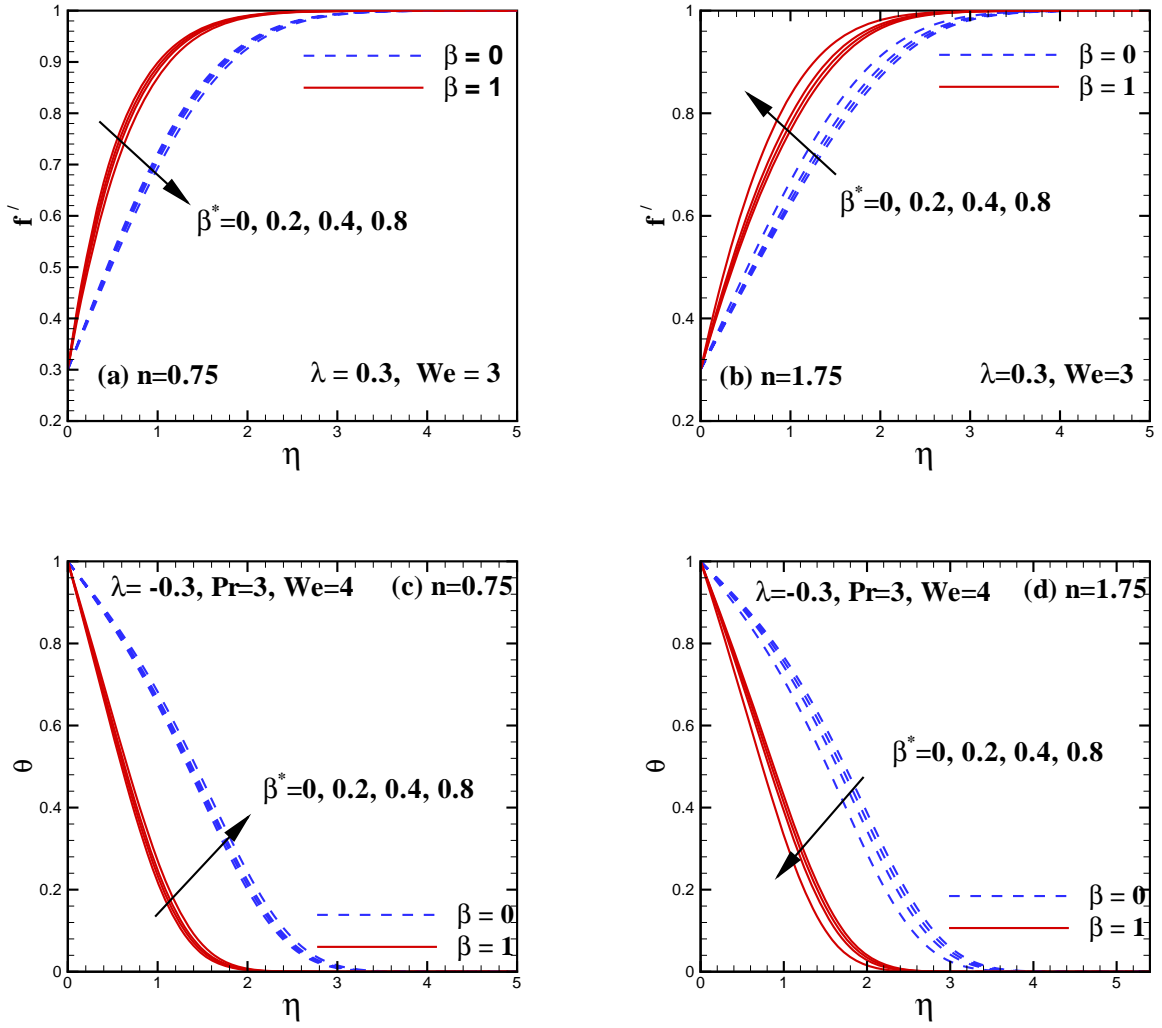


**Fig. 2.4:** Simulated velocity  $f'(\eta)$  and temperature  $\theta(\eta)$  profiles for  $\lambda$  when  $We = 3.0$ ,  $Pr = 1.0$ .



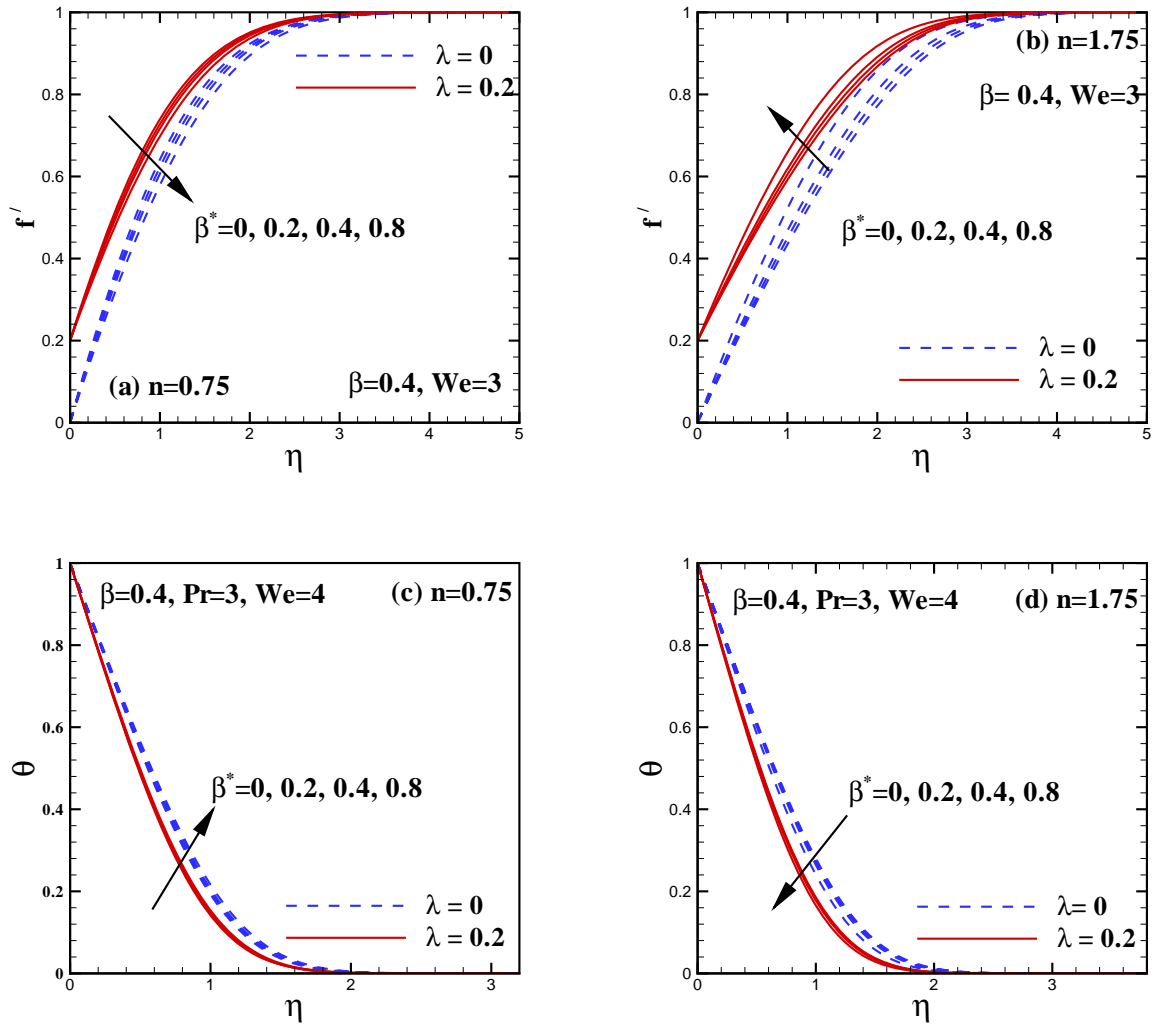


**Fig. 2.5:** Simulated velocity  $f'(\eta)$  and temperature  $\theta(\eta)$  profiles for  $\beta$  when  $We = 3.0$ ,  $Pr = 1.0$ .

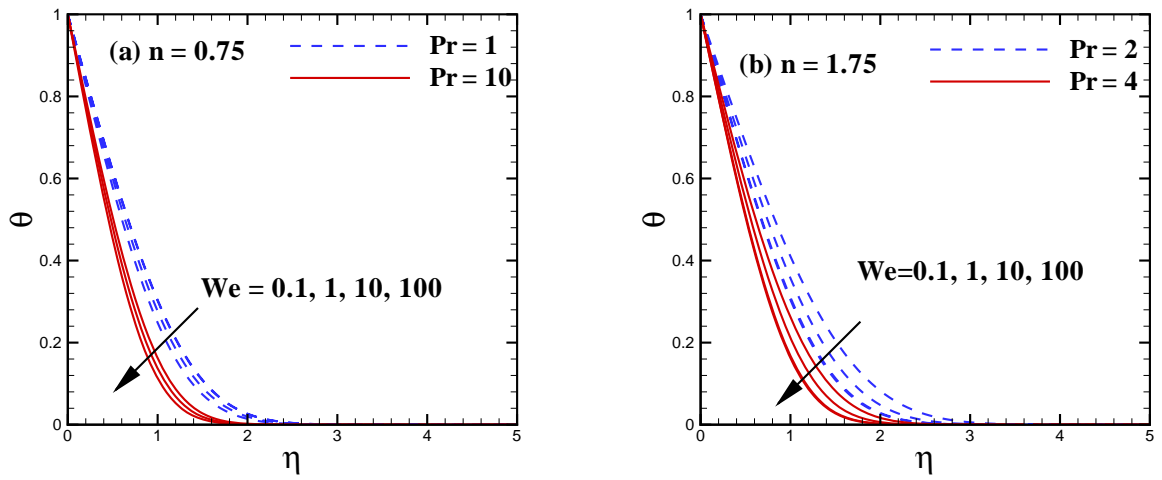


**Fig. 2.6:** Simulated temperature profile  $\theta(\eta)$  for  $We$  when  $\beta = 0.4$ ,  $\lambda = -0.3$ .

**Table 2.1:** Contrast values of  $-f''(0)$  for different  $\beta$ , when  $\beta^* = We = 0$  and  $n = 1$ .

$\beta$	Rajagopal <i>et al.</i> [58]	Kuo [59]	Present study
0	–	0.469600	0.469600
0.3	0.474755	0.775524	0.474755
0.6	0.995836	0.995757	0.995836
1.2	1.335722	1.333833	1.335722

**Table 2.2:** Numerical values of the skin friction coefficient  $Re^{1/2}C_{fx}$  for different  $\beta^*$ ,  $\beta$  and  $\lambda$ , when  $Pr = 1$  and  $We = 3$ .

$\beta^*$	$\beta$	$\lambda$	$Re^{1/2}C_{fx}$	
			$n = 0.75$	$n = 1.75$
0	0.3	0.2	0.961012	1.22977
			0.979278	1.20104
			0.996203	1.16925
			1.026900	1.09174
0.001	0	0.2	0.594385	0.706434
	0.3		0.961107	1.22963
	0.6		1.310680	1.77143
	1.2		2.23300	3.26384
0.001	0.3	-0.3	1.170530	1.56324
		-0.2	1.157030	1.54768
		0	1.084620	1.43226
		0.2	0.961107	1.22963

**Table 2.3:** Numerical values of the local Nusselt number  $Re^{-1/2}Nu_x$  for different  $\beta^*$ ,  $\beta$  and  $\lambda$  when  $Pr = 1$  and  $We = 3$ .

$\beta^*$	$\beta$	$\lambda$	$Re^{-1/2}Nu_x$	
			$n = 0.75$	$n = 1.75$
0	0.3	0.2	0.916605	0.860677
			0.912067	0.865626
			0.90800	0.871354
			0.900932	0.886604
0.001	0	0.2	0.795146	0.758852
	0.3		0.916581	0.860700
	0.6		1.04584	0.973570
	1.2		1.44201	1.33020
0.001	0.3	-0.3	0.664451	0.529774
		-0.2	0.722834	0.605179
		0	0.825856	0.740896
		0.2	0.916581	0.860700

## Chapter 3

# Steady Two-Dimensional Flow of Carreau Nanofluid

The main focus of this chapter is to present the mathematical modelling and solution for steady two-dimensional Carreau nanofluid flow over a stretching surface with infinite shear rate viscosity. The effects of Brownian motion and thermophoresis under the influence of convectively heated surface are analyzed. Using suitable transformations, nonlinear partial differential equations are transformed into ordinary differential equations and solved numerically using the Runge-Kutta Fehlberg method coupled with the shooting technique. The effects of various physical parameters on the temperature and nanoparticles concentration distributions are displayed graphically and discussed quantitatively. Finally, a correlation with accessible results in special cases is performed and found with fabulous consent.

### 3.1 Geometry of the Physical Model

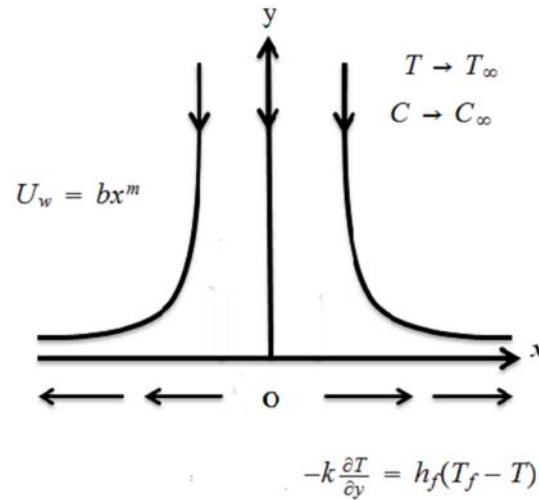


**Fig. 3.1:** A sketch of the computational domain.

### 3.2 Governing Problem

Here heat and mass transfer analysis for the steady two-dimensional laminar boundary layer flow of Carreau nanofluid in the presence of infinite shear rate viscosity over a non-linear stretching sheet are carried out. The coordinate system is selected in such a way that  $x$ -axis is measured along the stretching sheet while  $y$ -axis is normal to it and the fluid occupies the space  $y > 0$ . The sheet velocity is assumed to be  $U_w(x) = bx^m$ , where  $b$  and  $m$  are positive constants. Heat and mass transfer properties are explored through the Brownian motion and thermophoresis effects. The temperature  $T_w$  and concentration  $C_w$  at the surface of sheet are considered to be higher than the ambient temperature  $T_\infty$  ( $T_w > T_\infty$ ) and ambient concentration  $C_\infty$  ( $C_w > C_\infty$ ), respectively. The surface temperature is governed by the convective heating process which is described by the heat transfer coefficient  $h_f$  and  $T_f$  temperature of hot fluid below the surface.

The governing boundary layer equations for present flow are given by

$$\frac{\partial u}{\partial x} + \frac{\partial v}{\partial y} = 0, \quad (3.1)$$

$$\begin{aligned} u \frac{\partial u}{\partial x} + v \frac{\partial u}{\partial y} = \nu \left( \frac{\partial^2 u}{\partial y^2} \right) \left[ \beta^* + (1 - \beta^*) \left\{ 1 + \Gamma^2 \left( \frac{\partial u}{\partial y} \right)^2 \right\}^{\frac{n-1}{2}} \right] \\ + \nu(n-1)(1-\beta^*)\Gamma^2 \left( \frac{\partial^2 u}{\partial y^2} \right) \left( \frac{\partial u}{\partial y} \right)^2 \left\{ 1 + \Gamma^2 \left( \frac{\partial u}{\partial y} \right)^2 \right\}^{\frac{n-3}{2}}, \end{aligned} \quad (3.2)$$

$$u \frac{\partial T}{\partial x} + v \frac{\partial T}{\partial y} = \alpha_1 \frac{\partial^2 T}{\partial y^2} + \tau \left[ D_B \frac{\partial C}{\partial y} \frac{\partial T}{\partial y} + \frac{D_T}{T_\infty} \left( \frac{\partial T}{\partial y} \right)^2 \right], \quad (3.3)$$

$$u \frac{\partial C}{\partial x} + v \frac{\partial C}{\partial y} = D_B \frac{\partial^2 C}{\partial y^2} + \frac{D_T}{T_\infty} \frac{\partial^2 T}{\partial y^2}, \quad (3.4)$$

with associated boundary conditions

$$u = U_w = bx^m, \quad v = 0, \quad -k \frac{\partial T}{\partial y} = h_f(T_f - T), \quad C = C_w \quad \text{at} \quad y = 0, \quad (3.5)$$

$$u \rightarrow 0, \quad T \rightarrow T_\infty, \quad C \rightarrow C_\infty \quad \text{as} \quad y \rightarrow \infty. \quad (3.6)$$

Here  $\nu$  the kinematic viscosity of the base fluid,  $\tau = \frac{(\rho c_p)}{(\rho c_f)}$  is the ratio of nanoparticles heat capacity and the base fluid heat capacity,  $D_B$  the Brownian diffusion coefficient,  $D_T$  the thermophoretic diffusion coefficient and  $T_\infty$  the ambient fluid temperature

The following dimensionless quantities are used to transform the governing partial differential equations into a scheme of ordinary differential equations

$$\eta = y \sqrt{\frac{b(m+1)}{2\nu}} x^{\frac{m-1}{2}}, \quad \Psi(x, y) = \sqrt{\frac{2\nu b}{m+1}} x^{\frac{m+1}{2}} f(\eta), \quad (3.7)$$

$$\theta(\eta) = \frac{T - T_\infty}{T_w - T_\infty}, \quad \phi = \frac{C - C_\infty}{C_w - C_\infty}. \quad (3.8)$$

Consequently, the momentum, energy, and concentration equations and the relevant bound-

ary conditions reduce to the following

$$\left[ \beta^* + (1 - \beta^*) \left\{ 1 + We^2 (f'')^2 \right\}^{\frac{n-3}{2}} \left\{ 1 + nWe^2 (f'')^2 \right\} \right] f''' + f f'' - \left( \frac{2m}{m+1} \right) (f')^2 = 0, \quad (3.9)$$

$$\theta'' + \text{Pr} f \theta' + \text{Pr} \left[ Nb \theta' \phi' + Nt (\theta')^2 \right] = 0, \quad (3.10)$$

$$\phi'' + \text{Pr} Le f \phi' + \left( \frac{Nt}{Nb} \right) \theta'' = 0, \quad (3.11)$$

with

$$f(0) = 0, \quad f'(0) = 1, \quad \theta'(0) = -\gamma [1 - \theta(0)], \quad \phi(0) = 1, \quad (3.12)$$

$$f'(\infty) \rightarrow 0, \quad \theta(\infty) \rightarrow 0, \quad \phi(\infty) \rightarrow 0. \quad (3.13)$$

In the above equations,  $Le$  the Lewis number,  $Nt$  the thermophoresis parameter,  $Nb$  the Brownian motion parameter and  $\gamma$  the Biot number. These quantities are defined as follows:

$$\begin{aligned} Le &= \frac{\nu}{D_B}, \quad Nb = \frac{(\rho c_p) D_B (C_w - C_\infty)}{\nu (\rho c_f)}, \\ Nt &= \frac{(\rho c_p) D_T (T_f - T_\infty)}{\nu (\rho c_f) T_\infty}, \quad \gamma = \frac{-h (2\nu/b (m+1))^{1/2}}{k}. \end{aligned} \quad (3.14)$$

### 3.2.1 Physical Parameters of Engineering Significance

The skin friction coefficient  $C_{fx}$ , the Nusselt number  $Nu_x$  and the Sherwood number  $Sh_x$  are the parameters of engineering interest defining the surface drag force, temperature and concentration flux at the surface, respectively. These parameters are defined as:

$$C_{fx} = \frac{\tau_w}{\rho U_w^2(x)}, \quad Nu_x = \frac{x q_w}{k (T_w - T_\infty)}, \quad Sh_x = \frac{x q_m}{D_B (C_w - C_\infty)}, \quad (3.15)$$

where  $\tau_w$ ,  $q_w$  and  $q_m$  are given by



$$\tau_w = \mu_0 \left( \frac{\partial u}{\partial y} \right) \left[ \beta^* + (1-\beta^*) \left\{ 1 + \Gamma^2 \left( \frac{\partial u}{\partial y} \right)^2 \right\}^{\frac{n-1}{2}} \right] \Big|_{y=0}, \quad (3.16)$$

$$q_w = -k \frac{\partial T}{\partial y} \Big|_{y=0}, \quad q_m = -D_B \frac{\partial C}{\partial y} \Big|_{y=0}. \quad (3.17)$$

Upon using Eq. (3.16) & (3.17) in (3.15), the skin friction coefficient, Nusselt number and the Sherwood number become

$$Re^{1/2} C_{fx} = \sqrt{\frac{m+1}{2}} f''(0) \left[ \beta^* + (1-\beta^*) \left\{ 1 + We^2 (f''(0))^2 \right\}^{\frac{n-1}{2}} \right], \quad (3.18)$$

$$Re^{-1/2} Nu_x = -\sqrt{\frac{m+1}{2}} \theta'(0), \quad Re^{-1/2} Sh_x = -\sqrt{\frac{m+1}{2}} \phi'(0). \quad (3.19)$$

where  $Re = \frac{U_w x}{\nu}$  is the local Reynolds number.

### 3.3 Solution Methodology

The nonlinear differential equations (3.9 – 3.11) with boundary conditions (3.12) – (3.13) have been solved numerically using Runge-Kutta Fehlberg order method along with shooting technique. So firstly Eqs. (3.9), (3.10) and (3.11) are converted into set of first order equations. For this purpose, we rewrite the above set of equations as given below:

$$f''' = \frac{\left( \frac{2m}{m+1} \right) (f')^2 - f f''}{\left[ \beta^* + (1-\beta^*) \{1 + nWe^2 (f'')^2\} \{1 + We^2 (f'')^2\}^{\frac{n-3}{2}} \right]}, \quad (3.20)$$

$$\theta'' = -Pr \left[ Nb \theta' \phi' + Nt (\theta')^2 \right] - Pr f \theta', \quad (3.21)$$

$$\phi'' = -Pr Le f \phi' - \left( \frac{Nt}{Nb} \right) \theta''. \quad (3.22)$$

The new variables defined below are utilized to reduce the above higher order equations into system of first order differential equations:

$$\begin{aligned}
f &= y_1, f' = y_2, f'' = y_3, f''' = y'_3, \theta = y_4, \\
\theta' &= y_5, \theta'' = y'_5, \phi = y_6, \phi' = y_7, \phi'' = y'_7.
\end{aligned} \tag{3.23}$$

After inserting Eq. (3.23) into Eqs. (3.20–3.22), a new system of ordinary differential equations is obtained as:

$$y'_1 = y_2, y'_2 = y_3, y'_3 = \frac{\left[\left(\frac{2m}{m+1}\right)y_2^2 - y_1y_3\right]}{\beta^* + (1-\beta^*) [1 + nWe^2y_3^2] [1 + We^2y_3^2]^{\frac{n-3}{2}}}, \tag{3.24}$$

$$y'_4 = y_5, \quad y'_5 = -\text{Pr} y_1y_5 - \text{Pr} Nb y_5y_7 - \text{Pr} Nt (y_5)^2, \tag{3.25}$$

$$y'_6 = y_7, \quad y'_7 = -\text{Pr} Le y_1y_7 - \left(\frac{Nt}{Nb}\right) y'_5, \tag{3.26}$$

together with the boundary conditions

$$\begin{pmatrix} y_1 \\ y_2 \\ y_3 \\ y_4 \\ y_5 \\ y_6 \\ y_7 \end{pmatrix} = \begin{pmatrix} 0 \\ 1 \\ u_1 \\ u_2 \\ -\gamma(1-u_2) \\ 1 \\ u_3 \end{pmatrix}. \tag{3.27}$$

For the purpose of numerical computations of the above system of equations using Runge-Kutta method, the numerical computations require seven initial conditions but only four initial conditions are known. However, the values of  $f'(\infty)$ ,  $\theta(\infty)$  and  $\phi(\infty)$  are known and these end values are used to guess three unknown initial conditions with the Newton Raphson iteration. Here  $u_1, u_2, u_3$  are the initial guesses for the values of  $f''(0)$ ,  $\theta(0)$  and  $\phi'(0)$ . Thus, in the present study the value of  $\eta = \eta_{\max}$  is taken to be 10 and step-size is taken to be  $\Delta\eta = 0.01$  with relative error tolerance  $10^{-5}$ .

### 3.4 Results and Discussion

The prime goal of this section is to comprehend the physical aspects of mathematical and numerical model. The simulated results of non-dimensional temperature and concentration fields are presented graphically for varying values of physical parameters. For illustration, numerical results are shown in **Tables 3.1** and **3.2** and **Figs. 3.2 – 3.9**.

Taking into account the obtained numerical results, **Figs. 3.2(a – d)** delineate the influence of Weissenberg number  $We$  on the temperature  $\theta(\eta)$  and concentration  $\phi(\eta)$  profiles for both shear thinning and shear thickening fluids. From these **Figs.**, it is observed that for larger values of the Weissenberg number, the temperature and nanoparticle concentration enhance in shear thinning ( $n < 1$ ) fluid but quite the opposite behavior is prominent in shear thickening ( $n > 1$ ) fluid. Same pattern has been exposed for thermal and concentration boundary layer thicknesses.

The effects of thermophoresis parameter  $Nt$  on the temperature and nanoparticles concentration profiles for both shear thinning and shear thickening fluids are presented through **Figs. 3.3(a – d)**. A similar behavior appears for both the temperature and nanoparticles concentration fields and we observed that the magnitude of the temperature distribution as well as the nanoparticles volume fraction is increased for increasing values of thermophoresis parameter. This is due to the thermophoresis force produced by the temperature gradient moves the fluid fastly away from the sheet. In this manner it pushes the particles from hot surface towards the ambient fluid and thus moves larger extent of the fluid. This leads to limited rise in fluid temperature and concentration occur. **Figs. 3.4(a, b)** present the effects of the Brownian motion parameter  $Nb$  on the temperature and nanoparticles concentration profiles. By varying the values of  $Nb$ , examining both the shear thinning and shear thickening fluids, we noticed that the temperature and thermal boundary layer thickness are increased while nanoparticle concentration and concentration boundary layer thickness are decreased. By definition, augmentary the Brownian motion parameter, the intensity of this chaotic motion enhances the kinetic energy of the nanoparticles and as a result nanofluid temperature grows.

Behavior of the Lewis number  $Le$  on the temperature and concentration profiles is presented through **Figs. 3.5(a, b)**. It is observed that the Lewis number significantly affects the temperature and nanoparticles concentration distributions for both shear thinning and shear

thickening fluids. This is due to the fact that the augmented values of Lewis number parallel to stronger viscous diffusion as compared to mass diffusion. This leads to a improvement in molecular motions and their interactions due to this temperature of the fluid grows. On the other hand, a relatively opposite behavior is noticed for the concentration profiles. Physically, the mass transfer rate enhances as the Lewis number increases. For a base fluid of certain momentum diffusivity, a higher Lewis number possesses low Brownian diffusion coefficient and this result in a reduced penetration depth for the nanoparticle concentration boundary layer thickness.

In order to illustrate the influence of the viscosity ratio parameter  $\beta^*$  on the temperature and concentration distributions we have plotted **Figs. 3.6(a, b)** and **3.7(a, b)** examining both shear thinning and shear thickening fluids. From these Figs., we observe a minor dependence of temperature and concentration distributions on  $\beta^*$ . However, it is interesting to note that graph of temperature and concentration disclose quite the opposite trends with uplifting  $\beta^*$  for the shear thinning and shear thickening fluids. Moreover the same trend is depicted for temperature and concentration distributions. Additionally, these **Figs.** portray that the boundary layer thickness becomes thin in shear thinning fluid as we increase the viscosity ratio parameter and quite the opposite is true for shear thickening fluid.

The effects of Biot number  $\gamma$  on the temperature and nanoparticles concentration distribution are illustrated in **Figs. 3.8(a, b)** and **3.9(a, b)**. These **Figs.** put in evidence that the effect of enhancing Biot number is to increase significantly both temperature and related boundary layer thickness. This is because of the fact that enhancing Biot number results in a reduction in the thermal resistance of the surface and as a result of convective heat transfer to the fluid rises. Qualitatively, similar results have been found for increasing effects of Biot number on the nanoparticles concentration distribution.

**Table 3.1** is created to demonstrate the influence of Prandtl number  $Pr$ , the thermophoresis parameter  $Nt$ , the Brownian motion parameter  $Nb$ , viscosity ratio parameter  $\beta^*$ , Biot number  $\gamma$  and Lewis number  $Le$  on the Nusselt number  $Re^{-1/2} Nu_x$  for shear thinning and shear thickening fluids. On the evident of **table 3.1**, the local Nusselt number is a decreasing function of the thermophoresis parameter, Brownian motion parameter and Lewis number in shear thinning and shear thickening fluids. Moreover the effect of viscosity ratio parameter  $\beta^*$  on the

Nusselt number are quite the opposite for shear thinning ( $n < 1$ ) and shear thickening ( $n > 1$ ) fluids. By uplifting  $\beta^*$  the Nusselt number is increased for shear thinning fluid and decreased for shear thickening fluid. **Table 3.2** provides numerical results of the reduced Sherwood number  $Re^{-1/2}Shx$  for selected values of viscosity ratio parameter, thermophoresis parameter, Brownian motion parameter, Prandtl number, Biot number and Lewis number when  $m = 2.5$  and  $We = 2.0$  are fixed. From this table, it can be seen that the Sherwood number enhances by uplifting the Prandtl number, Lewis number and Brownian motion parameter in both cases. It is also noted that rise in thermophoresis parameter depreciates the mass transfer rate in shear thinning and shear thickening fluids. It is further observed that for increasing Biot number and Nusselt number, Sherwood number is decreased for both shear thinning ( $n < 1$ ) and shear thickening ( $n > 1$ ) cases. Additionally the effect of viscosity ratio parameter  $\beta^*$  on the Sherwood number are quite the opposite for shear thinning and shear thickening fluids. By increasing the  $\beta^*$ , the Sherwood number is increased for shear thickening and decreased for shear thing fluids. To validate the accuracy of the outcomes, the comparison of the results of present study with the existing reported works in the literature has been accomplished and tabulated in **Table 3.3**. The comparisons indicate excellent agreement with former pros.

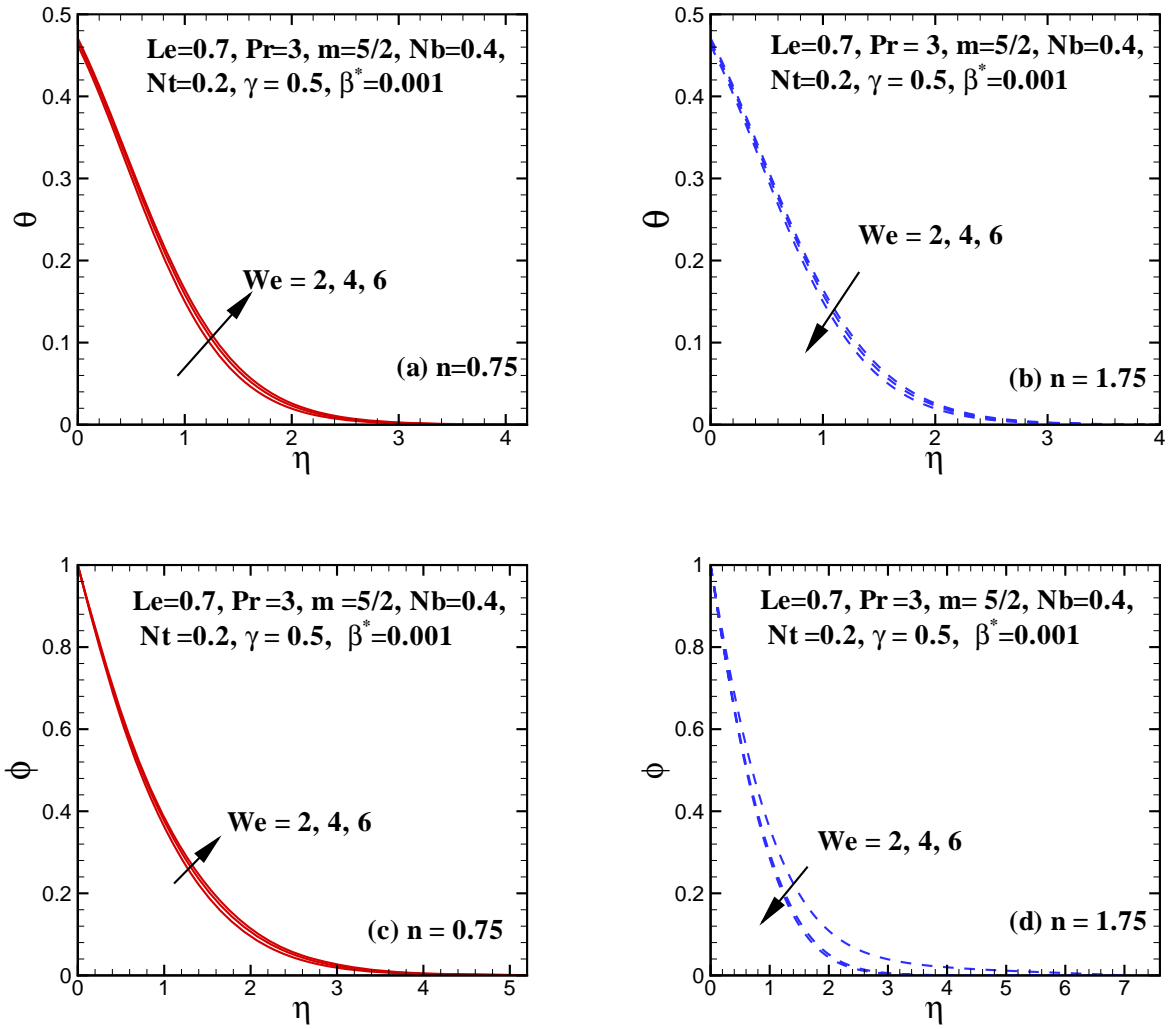


**Fig. 3.2:** Effect of Weissenberg number on temperature  $\theta(\eta)$  and concentration  $\phi(\eta)$  profiles.

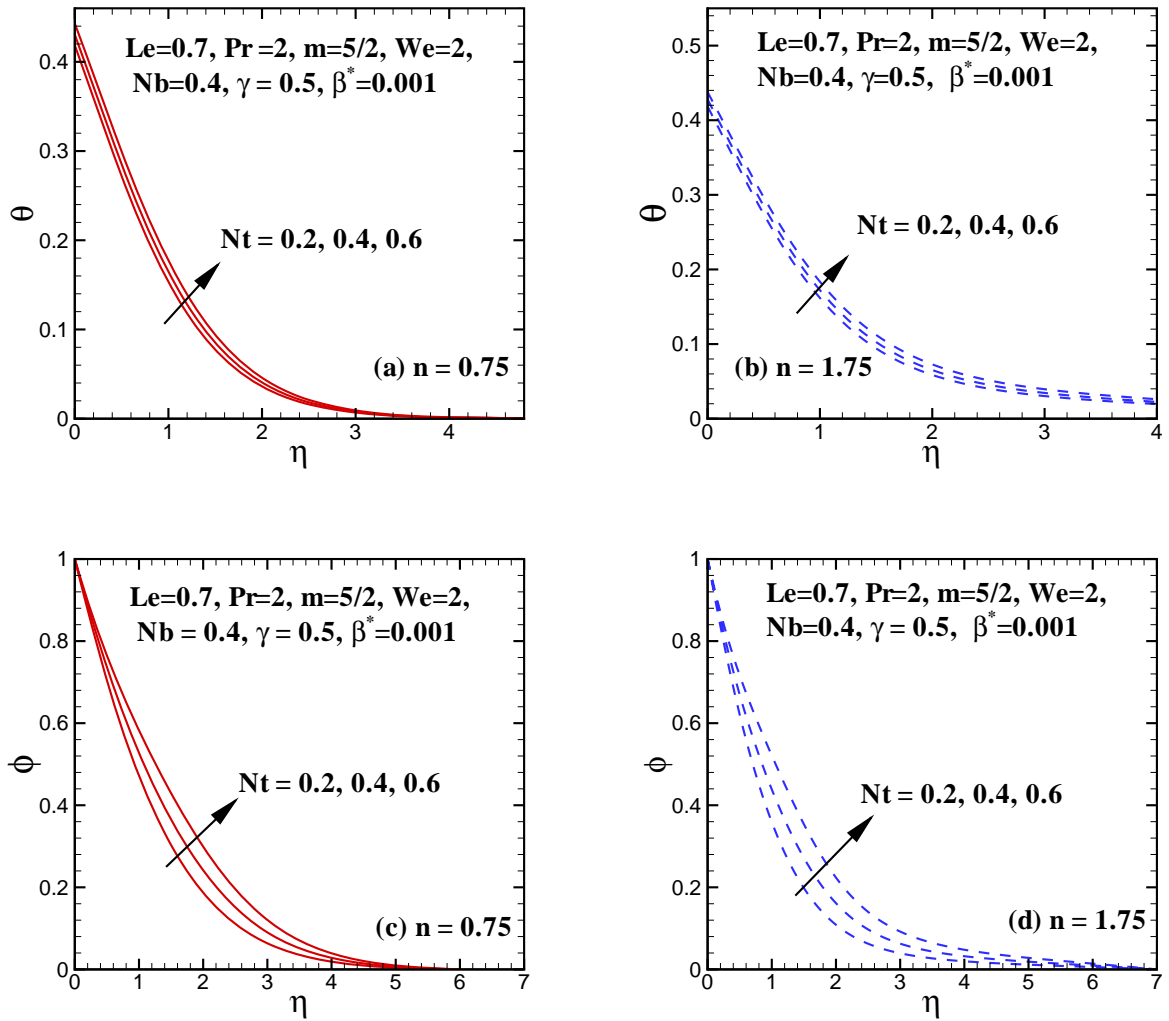


**Fig. 3.3:** Effect of Thermophoresis parameter  $Nt$  on temperature  $\theta(\eta)$  and concentration  $\phi(\eta)$  profiles.

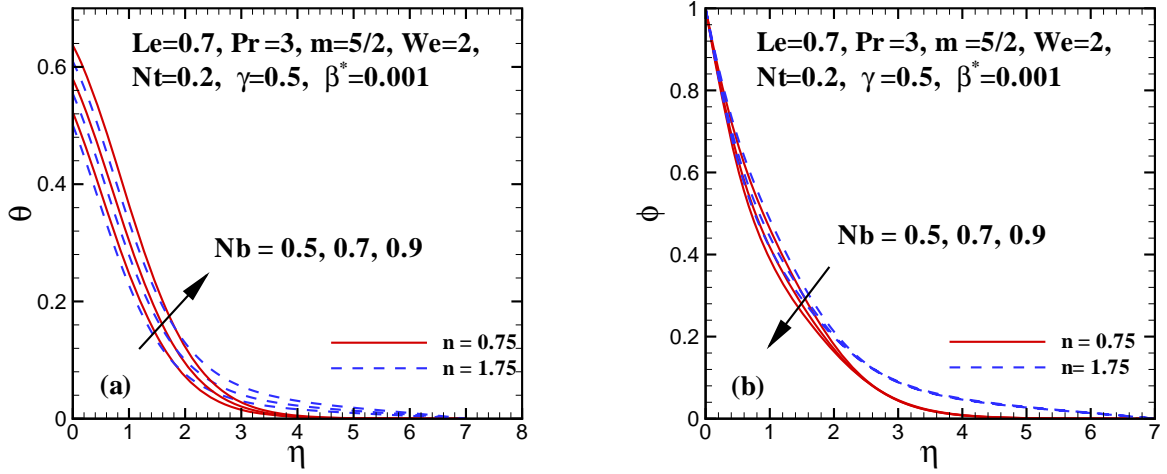


**Fig. 3.4:** Effect of Brownian motion parameter on temperature  $\theta(\eta)$  and concentration  $\phi(\eta)$  profiles.

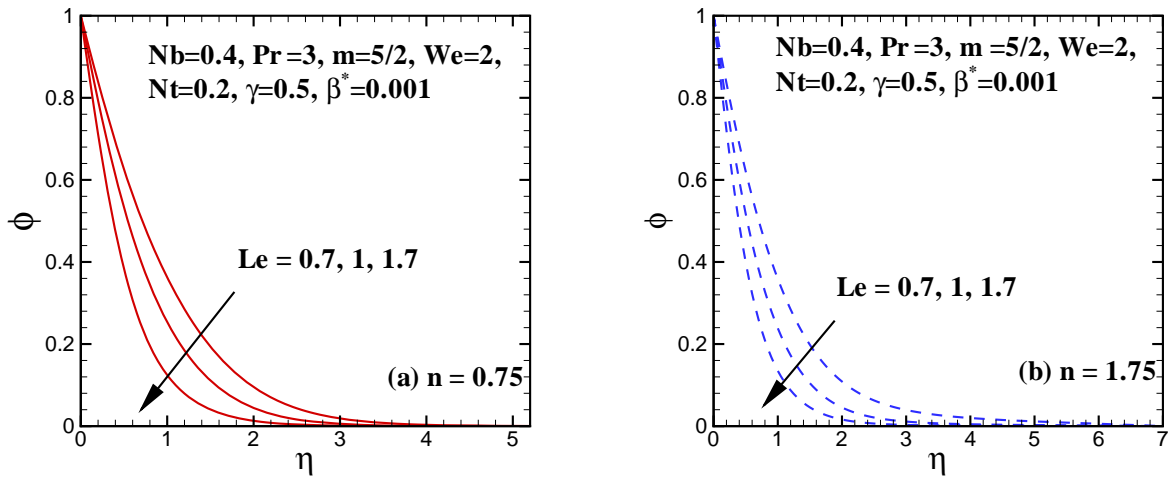


**Fig. 3.5:** Effect of Lewis number on concentration  $\phi(\eta)$  profile.



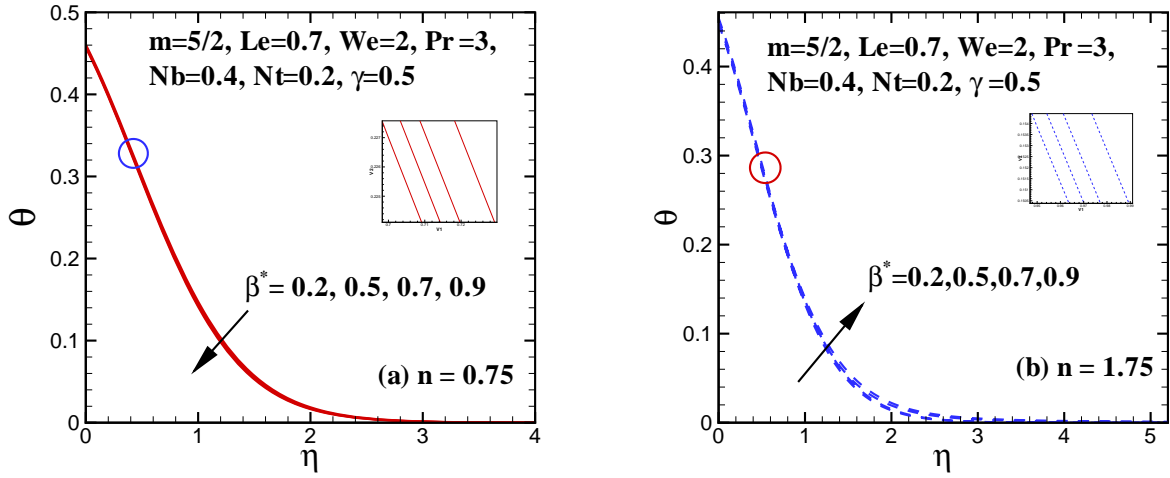


Fig. 3.6: Effect of  $\beta^*$  on temperature  $\theta(\eta)$  profile .

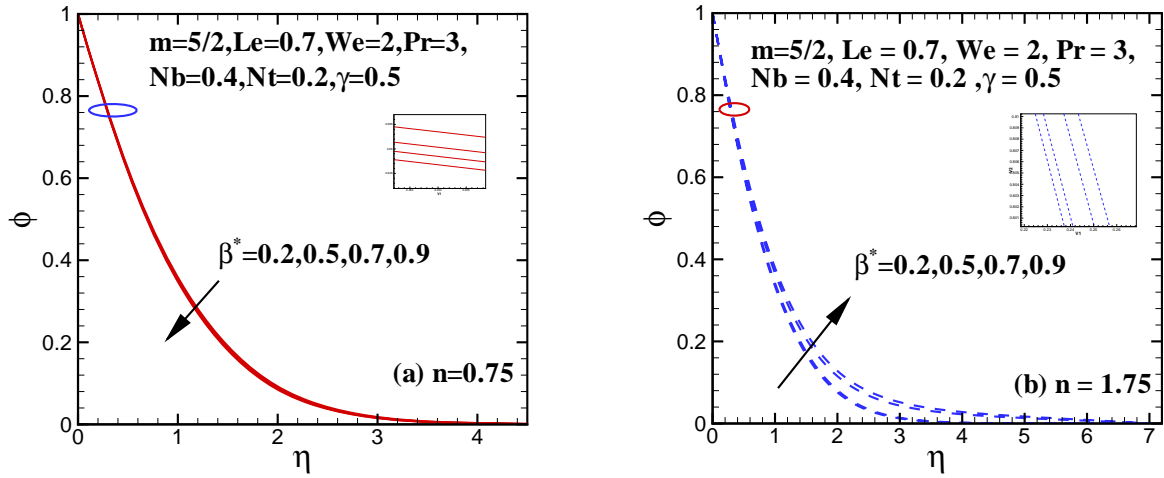


Fig. 3.7: Effect of  $\beta^*$  on concentration profile  $\phi(\eta)$ .

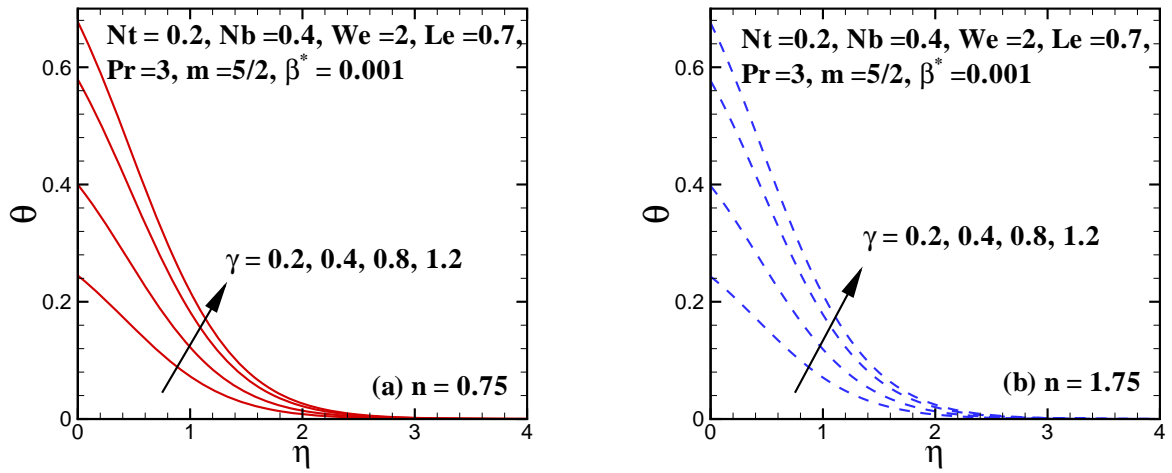


Fig. 3.8: Effect of Biot number  $\gamma$  on temperature  $\theta(\eta)$  profile .

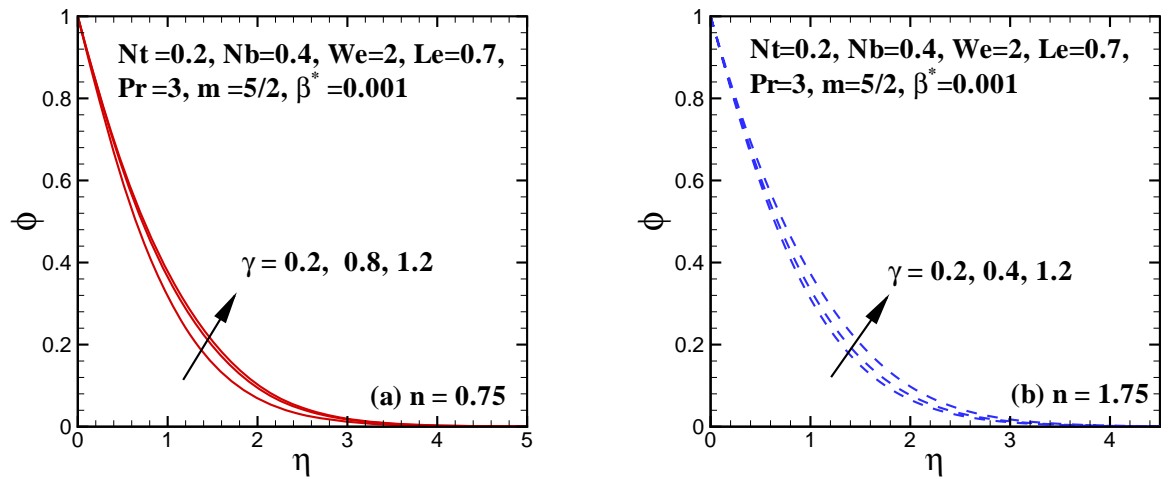


Fig. 3.9: Effect of Biot number  $\gamma$  on concentration  $\phi(\eta)$  profile.

**Table 3.1** : Numerical values of the local Nusselt number  $Re^{-1/2}Nu_x$  for different  $n, Nt, Nb, Le, \gamma, Pr, \beta^*$  when  $m = 2.5$  and  $We = 2$ .

$\beta^*$	$Nt$	$Nb$	$Le$	$\gamma$	$Pr$	$Re^{-1/2}Nu_x$	
						$n = 0.7$	$n = 1.7$
0.0	0.2	0.4	0.7	0.5	3.0	0.355630	0.365701
	0.2					0.356590	0.364943
	0.5					0.357821	0.363465
	0.7					0.358532	0.362453
	0.9					0.359177	0.360662
0.1	0.2	0.4	0.7	0.5	2.0	0.355635	0.365697
		0.4				0.340856	0.353319
		0.6				0.324911	0.340433
0.1	0.2	0.5	0.7	0.5	3.0	0.327875	0.338728
		0.7				0.269675	0.281788
		0.9				0.211655	0.224270
			0.7	0.5	3.0	0.355635	0.365697
			1.0			0.338606	0.346846
			1.4			0.323415	0.331075
				0.2		0.198773	0.201527
				0.4		0.314801	0.322421
				0.8		0.439855	0.456354
				1.2		0.504607	0.527490
					2.0	0.352722	0.361211
					3.0	0.355635	0.365697
					4.0	0.342344	0.351365

**Table 3.2** : Numerical values of the local Sherwood number  $Re^{-1/2}Sh_x$  for different  $n, Nt, Nb, Le, \gamma, Pr, \beta^*$  when  $m = 2.5$  and  $We = 2$ .

$\beta^*$	$Nt$	$Nb$	$Le$	$\gamma$	$Pr$	$Re^{-1/2}Sh_x$	
						$n = 0.7$	$n = 1.7$
0.0	0.2	0.4	0.7	0.5	3.0	1.099024	1.117449
	0.2					1.107000	1.102998
	0.5					1.117527	1.075874
	0.7					1.123788	1.159907
	0.9					1.129561	1.142954
0.1	0.2	0.4	0.7	0.5	2.0	1.099066	1.117383
		0.4				1.027651	1.019262
		0.6				0.972770	0.929015
0.1	0.2	0.5	0.7	0.5	3.0	1.129594	1.149216
		0.7				1.164477	1.185032
		0.9				1.182824	1.203461
			0.7	0.5	3.0	1.099066	1.117383
			1.0			1.416732	1.470551
			1.4			1.770195	1.844287
				0.2		1.136428	1.165137
				0.4		1.108624	1.129932
				0.8		1.079755	1.091175
				1.2		1.065296	1.070680
					2.0	0.806678	0.766691
					3.0	1.099066	1.117383
					4.0	1.357110	1.409126

**Table 3.3:** Comparison of the results of the local rate of heat transfer at the surface  $Re^{-1/2}Nu_x$  for diverse values of Pr. when  $Nt = 0.1$ ,  $Le = 1.0$ ,  $m = 2$ ,

$\beta^* = 0$ ,  $We = 3$ ,  $Nb = 0.5$  are fixed.

Pr	Nt	Le	Ref.[77]		Present study	
			$n = 0.7$	$n = 1.7$	$n = 0.7$	$n = 1.7$
1	0.1	1.0	0.61401	0.73544	0.614011	0.735441
3	0.1	1.0	1.24403	1.41979	1.244032	1.419790
5	0.1	1.0	1.66360	1.86146	1.663601	1.861463

## Chapter 4

# Radiative Heat Transfer in Stagnation Point Flow of MHD Carreau Fluid over a Stretched Surface

The current chapter presents a study of MHD stagnation point flow of Carreau fluid in the presence of infinite shear rate viscosity. Moreover, heat transfer analysis in the existence of non-linear radiation with convective boundary condition is performed. Effects of Joule heating is observed and mathematical analysis is presented subject to viscous dissipation. The suitable transformations are employed to alter the leading partial differential equations to a set of ordinary differential equations. The subsequent non-straight common ordinary differential equations are solved numerically by an effective numerical approach specifically Runge-Kutta Fehlberg method alongside shooting technique. The numerical results for Carreau fluid velocity and temperature fields are presented graphically.

## 4.1 Description of the Problem

We examine the steady boundary layer flow of an incompressible Carreau viscosity liquid model in the region of stagnation point over a stretching surface. The flow is initiated by a linear stretching surface. The coordinate system is designated in such a way that  $x$ -axis is measured alongside the stretching sheet while  $y$ -axis is normal to it and fluid occupies the space  $y > 0$ . The magnetic field  $B_0$  is uniform and applied in  $y$  direction and the induced magnetic field is neglected under low magnetic Reynolds number assumption. The sheet velocity is assumed to be  $U_w(x) = cx$  with  $c > 0$  is stretching rate. The velocity of exterior flow is  $U_\infty = ax$  ( $a > 0$ ), where  $a$  is constant. Moreover, heat transfer analysis is completed along the nonlinear thermal radiation with convective boundary condition at the surface. The viscous dissipation and Joule heating effects are also incorporated.

Under the above assumptions and the usual boundary-layer approximations, the governing boundary layer equations for present flow are given by

$$\frac{\partial u}{\partial x} + \frac{\partial v}{\partial y} = 0, \quad (4.1)$$

$$\begin{aligned} u \frac{\partial u}{\partial x} + v \frac{\partial u}{\partial y} = U_\infty \frac{dU_\infty}{dx} + \nu \left( \frac{\partial^2 u}{\partial y^2} \right) & \left[ \beta^* + (1-\beta^*) \left\{ 1 + \Gamma^2 \left( \frac{\partial u}{\partial y} \right)^2 \right\}^{\frac{n-1}{2}} \right] \\ + \nu(n-1)(1-\beta^*)\Gamma^2 \left( \frac{\partial^2 u}{\partial y^2} \right) \left( \frac{\partial u}{\partial y} \right)^2 & \left\{ 1 + \Gamma^2 \left( \frac{\partial u}{\partial y} \right)^2 \right\}^{\frac{n-3}{2}} \\ + \frac{\sigma B_0^2}{\rho} (U_\infty - u), & \end{aligned} \quad (4.2)$$

$$\begin{aligned} u \frac{\partial T}{\partial x} + v \frac{\partial T}{\partial y} = \alpha_1 \frac{\partial^2 T}{\partial y^2} - \frac{1}{\rho c_p} \frac{\partial q_r}{\partial y} + \frac{\sigma B_0^2}{\rho c_p} u^2 \\ + \frac{\nu}{c_p} \left( \frac{\partial u}{\partial y} \right)^2 \left[ \beta^* + (1-\beta^*) \left\{ 1 + \Gamma^2 \left( \frac{\partial u}{\partial y} \right)^2 \right\}^{\frac{n-1}{2}} \right]. \end{aligned} \quad (4.3)$$

Radiative heat flux used in Eq. (4.3), whose expression via Roseland approximation (cf. Roseland [78]) is given by

$$q_r = - \left( \frac{4\sigma^*}{3k^*} \frac{\partial T^4}{\partial y} \right), \quad (4.4)$$

For a planer boundary layer flow over a heated surface, Eq. (4.5) can be written as (cf. Shahzad *et al.* [79])

$$q_r = -\frac{16\sigma^*}{3k^*} \left( T^3 \frac{\partial T}{\partial y} \right). \quad (4.5)$$

Using Eq. (4.5) the energy Eq.(4.3) can be composed as

$$\begin{aligned} u \frac{\partial T}{\partial x} + v \frac{\partial T}{\partial y} &= \frac{\partial}{\partial y} \left[ \left( \alpha_1 + \frac{16\sigma^* T^3}{3k^* \rho c_p} \right) \frac{\partial T}{\partial y} \right] + \frac{\sigma B_0^2}{\rho c_p} u^2 \\ &+ \frac{\nu}{c_p} \left( \frac{\partial u}{\partial y} \right)^2 \left[ \beta^* + (1-\beta^*) \left\{ 1 + \Gamma^2 \left( \frac{\partial u}{\partial y} \right)^2 \right\}^{\frac{n-1}{2}} \right]. \end{aligned} \quad (4.6)$$

The boundary conditions of the present problem are

$$u = U_w = cx, \quad v = 0, \quad -k \frac{\partial T}{\partial y} = h_f(T_f - T) \quad \text{at} \quad y = 0, \quad (4.7)$$

$$u = U_\infty \rightarrow ax, \quad T \rightarrow T_\infty \quad \text{as} \quad y \rightarrow \infty. \quad (4.8)$$

The following dimensionless quantities are utilized to change the governing partial differential equations into a scheme of ordinary differential equations

$$\begin{aligned} \eta = y \sqrt{\frac{c}{\nu}}, \quad \Psi(x, y) = x \sqrt{c\nu} f(\eta), \quad \theta(\eta) = \frac{T - T_\infty}{T_f - T_\infty}, \\ u = cx f'(\eta), \quad v = -\sqrt{c\nu} f(\eta), \end{aligned} \quad (4.9)$$

where  $T = T_\infty + [1 + (\theta_w - 1)\theta]$  with  $\theta_w = \frac{T_f}{T_\infty}$ .

Consequently, momentum and energy equations with the relevant boundary conditions are reduced to the accompanying ordinary differential equations



$$\left[ \beta^* + (1 - \beta^*) \left\{ 1 + We^2 (f'')^2 \right\}^{\frac{n-3}{2}} \left\{ 1 + nWe^2 (f'')^2 \right\} \right] f''' + ff'' - (f')^2 + \alpha^{*2} + M^2 (\alpha^* - f') = 0, \quad (4.10)$$

$$\theta'' + Pr f \theta' + \frac{4}{3N_R} \frac{d}{d\eta} \left[ \{1 + (\theta_w - 1)\theta\}^3 \theta' \right] + Pr Ec (f'')^2 \left[ \beta^* + (1 - \beta^*) \left\{ 1 + We^2 (f'')^2 \right\}^{\frac{n-1}{2}} \right] + M^2 Pr Ec (f')^2 = 0, \quad (4.11)$$

with

$$f(0) = 0, \quad f'(0) = 1, \quad \theta'(0) = -\gamma [1 - \theta(0)], \quad (4.12)$$

$$f'(\infty) \rightarrow \alpha^*, \quad \theta(\infty) \rightarrow 0, \quad (4.13)$$

where  $M = \sqrt{\frac{\sigma B_0^2}{\rho c}}$  is the magnetic parameter,  $\alpha^* = a/c$  the velocity ratio parameter,  $N_R = \frac{kk^*}{4\sigma^* T_\infty^3}$  the radiation parameter,  $Ec = \frac{(cx)^2}{c_p(T_f - T_\infty)}$  the Eckert number and  $\gamma = \frac{h}{k} \sqrt{\frac{\nu}{c}}$  the local Biot number.

#### 4.1.1 Physical Parameters of Engineering Significance

The skin friction coefficient and the Nusselt number are the parameters of engineering interest which characterize the surface drag and wall heat transfer. These parameters are defined as

$$C_{fx} = \frac{\tau_w}{\rho U_w^2(x)}, \quad Nu_x = \frac{xq_w}{k(T_f - T_\infty)}, \quad (4.14)$$

where  $\tau_w$  and  $q_w$  are given by

$$\tau_w = \mu_0 \left( \frac{\partial u}{\partial y} \right) \left[ \beta^* + (1 - \beta^*) \left\{ 1 + \Gamma^2 \left( \frac{\partial u}{\partial y} \right)^2 \right\}^{\frac{n-1}{2}} \right], \quad q_w = -k \left( \frac{\partial T}{\partial y} \right)_{y \rightarrow 0} + (q_r)_w \quad (4.15)$$

Upon using Eq. (4.15), the local skin friction coefficient and local Nusselt number become

$$\begin{aligned} \text{Re}_x^{1/2} C_{fx} &= f''(0) \left[ \beta^* + (1 - \beta^*) \left\{ 1 + W e^2 (f''(0))^2 \right\}^{\frac{n-1}{2}} \right], \\ \text{Re}_x^{-1/2} Nu_x &= -\theta'(0) \left\{ 1 + \frac{4}{3N_R} [1 + (\theta_w - 1)\theta(0)]^3 \right\}. \end{aligned} \quad (4.16)$$

## 4.2 Solution Methodology

The governing flow equations (Eqs. (4.10) and (4.11)) are highly nonlinear and partially coupled set of ordinary differential equations. In order to find solution of these equations along side boundary conditions (4.12)–(4.13), the shooting technique along with fourth-fifth order Runge–Kutta integration scheme is utilized. Since Runge–Kutta Fehlberg method solves only initial value problem. So firstly Eqs. (4.10) and (4.11) are converted into set of first order equations. For this purpose, we rewrite the above set of equations as given below:

$$f''' = \frac{(f')^2 - \alpha^{*2} - f f'' - M^2 (\alpha^* - f')}{\left[ \beta^* + (1 - \beta^*) \{1 + n W e^2 (f'')^2\} \{1 + W e^2 (f'')^2\}^{\frac{n-3}{2}} \right]}, \quad (4.17)$$

$$\begin{aligned} \theta'' &= -\text{Pr} f \theta' - \frac{4}{3N_R} \frac{d}{d\eta} \left[ \{1 + (\theta_w - 1)\theta\}^3 \theta' \right] - M^2 \text{Pr} Ec (f')^2 \\ &\quad - \text{Pr} Ec (f'')^2 \left[ \beta^* + (1 - \beta^*) \left\{ 1 + W e^2 (f'')^2 \right\}^{\frac{n-1}{2}} \right]. \end{aligned} \quad (4.18)$$

The new variables defined below are utilized to reduce above higher order equations into system of first order differential equations:

$$\begin{aligned} f &= y_1, \quad f' = y_2, \quad f'' = y_3, \quad f''' = y_3', \\ \theta &= y_4, \quad \theta' = y_5, \quad \theta'' = y_5'. \end{aligned} \quad (4.19)$$

After inserting Eq. (4.19) into Eqs. (4.17) and (4.18), a new system of first-order ordinary

differential equations is obtained as:

$$y_1' = y_2, \quad y_2' = y_3, \quad y_3' = \frac{[y_2^2 - y_1 y_3 - \alpha^{*2} - M^2 (\alpha^* - y_2)]}{\beta^* + (1 - \beta^*) [1 + n W e^2 y_3^2] [1 + W e^2 y_3^2]^{\frac{n-3}{2}}}, \quad (4.20)$$

$$y_4' = y_5, \quad (4.21)$$

$$y_5' = \frac{-3 \text{Pr} N_R y_1 y_5 - 12 (\theta_w - 1) [1 + (\theta_w - 1) y_4]^2 y_5^2}{3 N_R + 4 [1 + (\theta_w - 1) y_4]^3} - \frac{3 N_R \text{Pr} Ec (y_3)^2 [\beta^* + (1 - \beta^*) \{1 + W e^2 (y_3)^2\}^{\frac{n-1}{2}}]}{3 N_R + 4 [1 + (\theta_w - 1) y_4]^3} + \frac{M^2 \text{Pr} Ec (y_2)^2}{3 N_R + 4 [1 + (\theta_w - 1) y_4]^3} \quad (4.22)$$

together with the boundary conditions

$$\begin{pmatrix} y_1 \\ y_2 \\ y_3 \\ y_4 \\ y_5 \end{pmatrix} = \begin{pmatrix} 0 \\ 1 \\ u_1 \\ u_2 \\ -\gamma (1 - u_2) \end{pmatrix}. \quad (4.23)$$

where  $u_1$  and  $u_2$  are the initial guesses for  $f''(0)$  and  $\theta'(0)$ .

The RK-Fehlberg method is an iterative algorithm which tries to find appropriate initial conditions for related initial value problem. For our problem, computations are based on the following steps:

1. Firstly chose the limit of  $\eta_\infty$  and the best suited limit for  $\eta_\infty$  is between 5 to 10.
2. Then select suitable initial guesses for  $y_3(0)$  and  $y_4(0)$ . Initially  $y_3(0) = -1$  and  $y_4(0) = 0.5$  are selected.
3. Then set of ODEs are solved with the help of fourth-fifth order Runge–Kutta integration scheme.
4. Finally, boundary residuals (absolute variations in given and calculated values of  $y_2(\infty)$  and  $y_4(\infty)$ ) is calculated. The solution will converge if entire values of boundary residuals are

less than tolerance error, which is considered  $10^{-5}$ .

5. If values of boundary residuals are larger than tolerance error, then values of  $y_3(0)$  and  $y_4(0)$  will be modified by Newton's method.

### 4.3 Results and Discussion

In order to examine results of the present study a numerical computation is performed for MHD stagnation point flow of Carreau fluid with infinite shear rate viscosity and nonlinear radiation over a convectively heated surface. The partially coupled set of Eqs. (4.10) – (4.11) with boundary conditions (4.12) and (4.13) are tackled numerically using Runge-Kutta fourth-fifth order method along with shooting technique. Moreover, representative outcomes about the skin friction and Nusselt number are recorded through tables. The influence of non-dimensional parameters like  $\alpha^*$ ,  $M$ ,  $\beta^*$ ,  $n$ ,  $\gamma$ ,  $Pr$ ,  $Ec$ ,  $\theta_w$  and  $N_R$  on dimensionless fluid velocity and temperature distributions are determined and presented through graphs. Additionally the accuracy of our numerical results is verified with earlier published results by Mahapatra and Gupta [80], Nazar *et al.* [81] and Ishak *et al.* [82] for particular cases through **table 4.1**. A good agreement is reported between these results.

**Fig. 4.1** represents a considerable variation in the velocity  $f'(\eta)$  and the corresponding boundary layer thickness at points where free stream velocity is different from sheet velocity. It is noted that the velocity increases and the boundary layer thickness decreases with an increase in  $\alpha^*$  for both shear thinning and thickening cases. Additionally an increasing value of  $\alpha^*$  depicts a significantly decrement in temperature  $\theta(\eta)$ . **Fig. 4.2** is plotted to inspect the impact of magnetic parameter  $M$  on temperature  $\theta(\eta)$  and velocity  $f'(\eta)$  profiles, for both shear thickening ( $n > 1$ ) and shear thinning ( $n < 1$ ) fluids. It is observed from these **Figs.** that increasing the magnetic parameter results in diminishing the velocity field and enhancement in temperature field. Physically  $M$  shows the ratio of electromagnetic force to the viscous force and strong values of  $M$  represents an increase in the Lorentz force. This is drag-like force that creates more resistance to transport phenomenon and fluid velocity as well as boundary layer thickness diminish. **Fig. 4.3** describes the impact of viscosity ratio parameter  $\beta^*$  on velocity  $f'(\eta)$  and temperature  $\theta(\eta)$  profiles for both hydromagnetic and hydrodynamic cases. It is

adequate to note that plots of velocity and temperature uncover inverse pattern with increasing  $\beta^*$ . It is noted that velocity profile depicts a considerable decrease with the higher values of  $\beta^*$  and opposite trend was observed for temperature profile. From **Fig. 4.4**, it is seen that increasing values of  $n$  (power law index) expand the fluid velocity for  $\alpha^* < 1$  and opposite trend is observed for  $\alpha^* > 1$ . Moreover by increasing the values of power law index  $n$  from 0.8 to 1.6 temperature profile decreases, when stretching velocity is greater than the free stream velocity. In addition when  $\alpha^* < 1$  temperature profile decreases.

**Fig. 4.5** is designed to observe the effects of the Biot number  $\gamma$  and Prandtl number  $Pr$  on the temperature profile  $\theta(\eta)$  for both the hydrodynamic and hydro magnetic flows. From these **Figs.**, it is observed that stronger values of the Biot number result in higher convection at the stretching sheet which increases the temperature of the fluid. It is also observed that in hydrodynamic flow thermal boundary layer is thicker as compared to hydromagnetic flows. Additionally increasing values of  $Pr$  decreases the temperature profile. Since the low Prandtl number depicts fluids with high thermal conductivity and this creates thicker thermal boundary layer structures than that for the large Prandtl number. **Fig. 4.6** is a plot of the variation in the temperature distribution for various values of the temperature ratio parameter  $\theta_w$  and the radiation parameter  $N_R$  for both hydrodynamic and hydromagnetic flows. These results reveal that temperature distribution decreases by increasing the values of radiation parameter. The thermal boundary layer thickness contracts for the greater radiation parameter. And the results are totally opposite for the temperature ratio parameter  $\theta_w$ . The temperature ratio parameter relates to higher wall temperature as compared to ambient fluid and as a result temperature of the fluid increases. Additionally thermal boundary layer thickness rises for higher values of the temperature ratio parameter. **Fig. 4.7** describes the effects of Eckert number  $Ec$  on temperature profile  $\theta(\eta)$ . It is noted that the increasing values of Eckert number flourishes the temperature profile.

**Table 4.2** shows the joint effects of the magnetic parameter  $M$  and the velocity ratio parameter  $\beta^*$  on the wall shear stress  $Re^{1/2}C_{fx}$ . Both parameters increase the magnitude of the wall shear stress  $Re^{1/2}C_{fx}$  for both shear thinning and thickening fluids. The skin friction is reduced for the higher values of the Weissenberg number  $We$  in the shear thinning fluid and is increased in the shear thickening fluid. Moreover, it is seen that the Nusselt number  $Re^{-1/2}Nu_x$

is decreased with  $M$  as the strong magnetic field reduce the extent of heat transfer rate. **Table 4.3** describes the effect of radiation parameter  $N_R$  on the Nusselt number  $Re^{-1/2}Nu_x$ . The amount of heat transfer rate decreases with the increasing values of  $N_R$ . In addition the Nusselt number increases with strong values of Prandtl number. It is because of the fact that the Prandtl number controls the relative thickness of the thermal boundary layer.

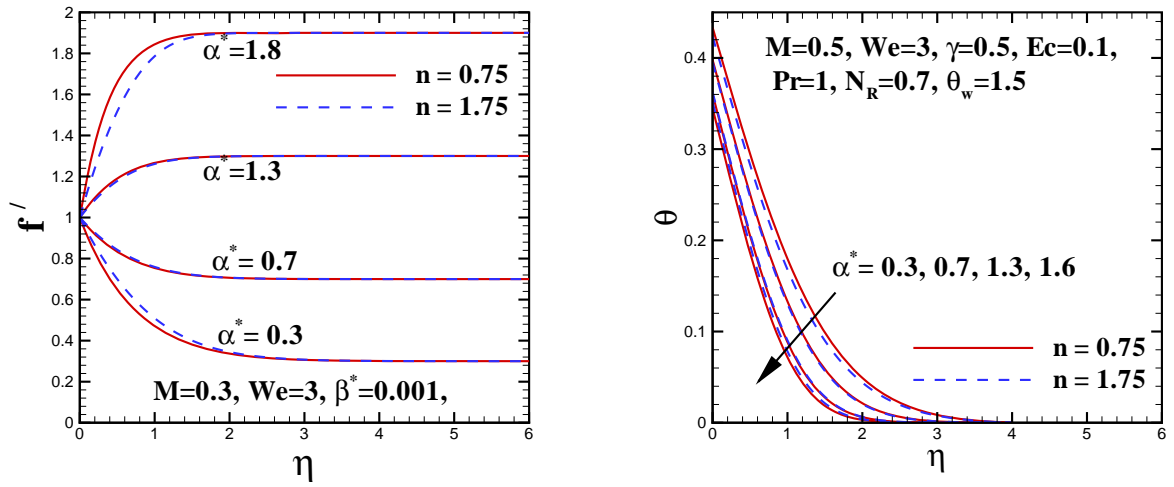


**Fig. 4.1:** Effects of the velocity ratio parameter  $\alpha^*$  on the velocity and temperature distributions.

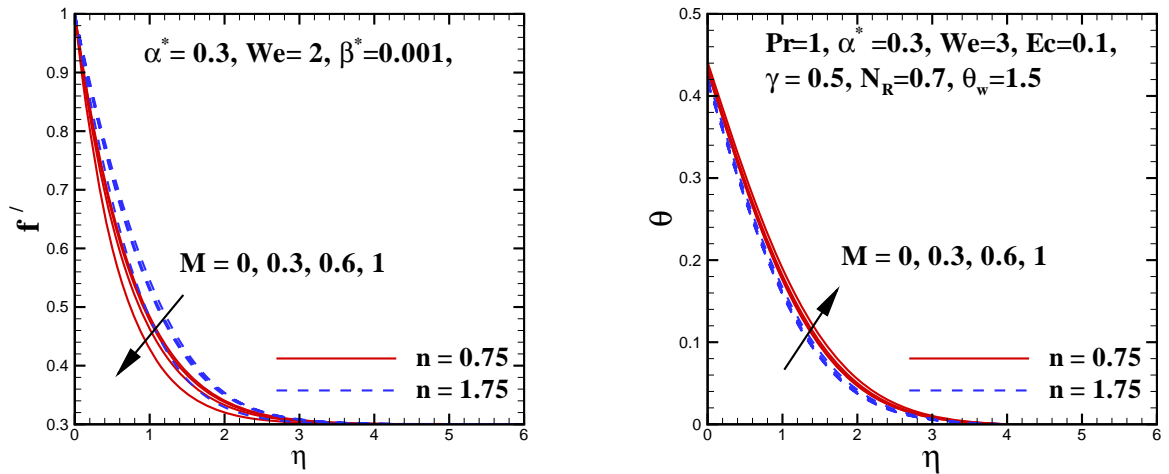


**Fig. 4.2:** Effects of the Magnetic parameter  $M$  on the velocity and temperature distributions.

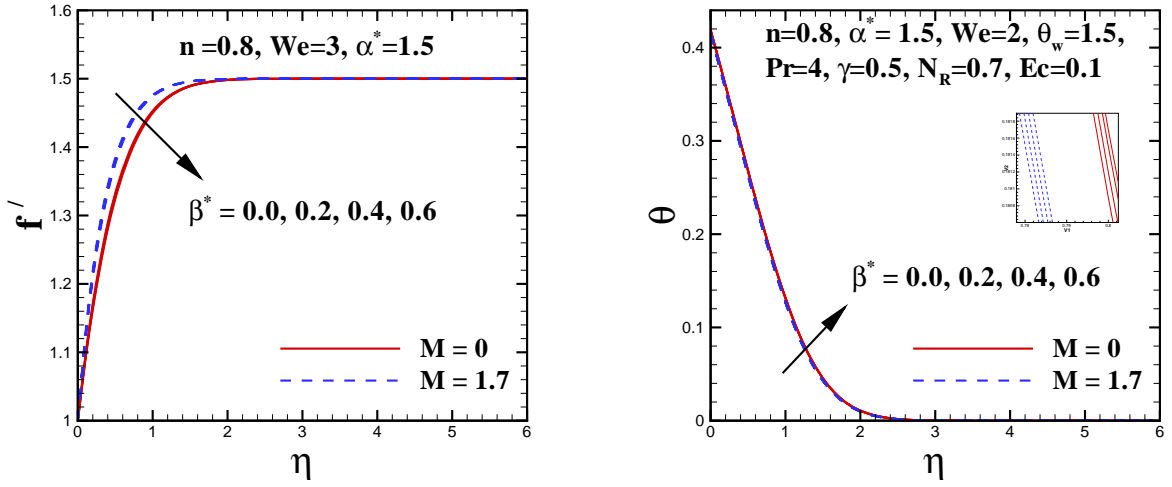


**Fig. 4.3:** Effects of the viscosity ratio parameter  $\beta^*$  on the velocity and temperature distributions.

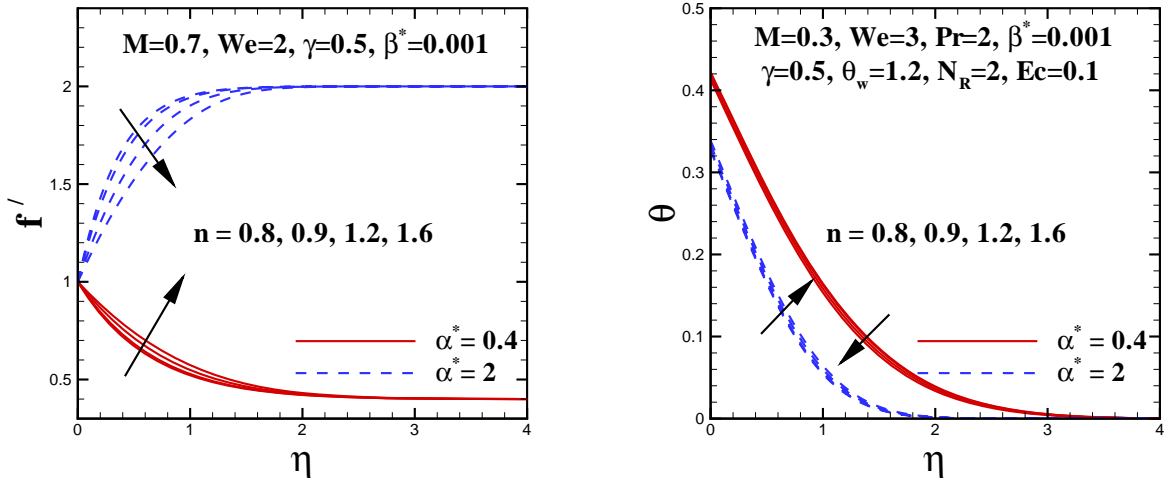


**Fig. 4.4:** Effects of the power law index  $n$  on the velocity and temperature distributions.

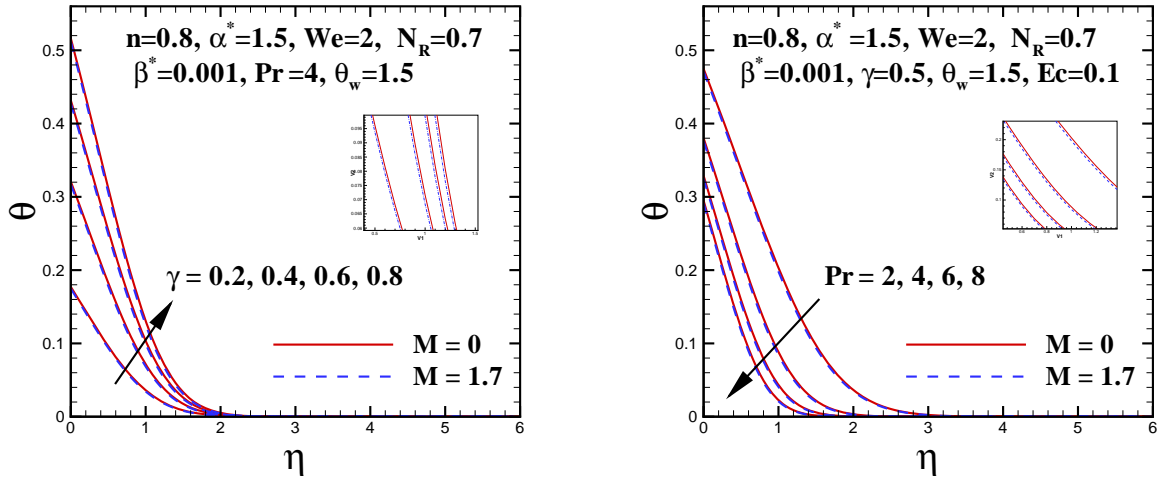


**Fig. 4.5:** Effects of the Biot number  $\gamma$  and Prandtl number  $Pr$  on the temperature distribution.

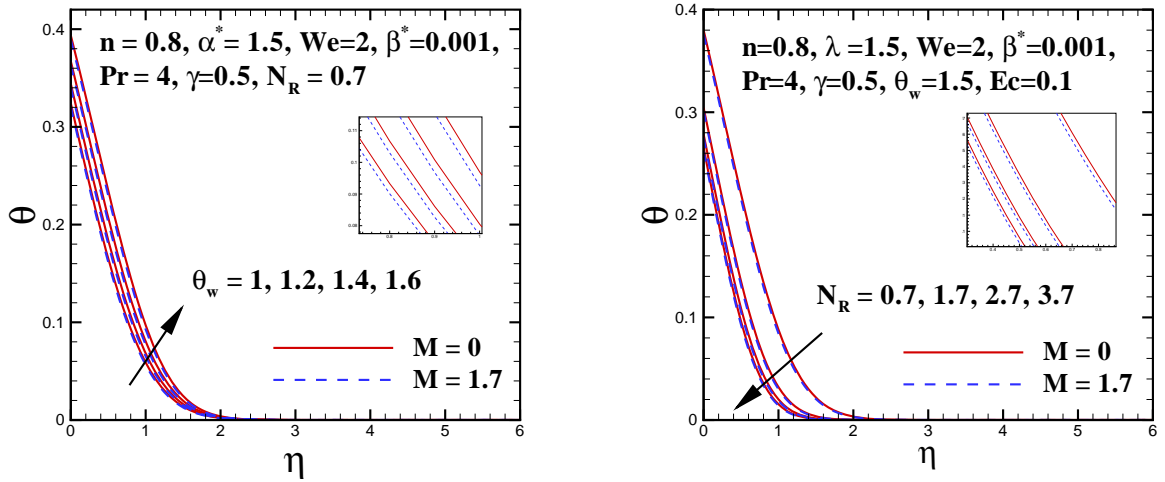


**Fig. 4.6:** Effects of the temperature ratio parameter  $\theta_w$  and radiation parameter  $N_R$  on temperature distribution.



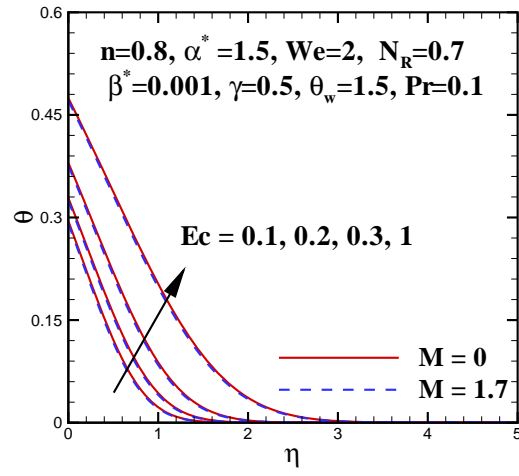


**Fig. 4.7:** Effects of the Eckert number  $Ec$  on temperature distribution.

**Table 4.1** : Contrast values of  $-f''(0)$  for  $\alpha^*$  when  $\beta^* = We = M = 0$  and  $n = 1$ .

$\alpha^*$	Mahapatra and Gupta [80]	Nazar <i>et al.</i> [81]	Ishak <i>et al.</i> [82]	Present results
0.01	—	—	0.9980	0.998028
0.10	0.9694	0.9694	0.9694	0.969650
0.20	0.9181	0.9181	0.9181	0.918165
0.50	0.6673	0.6673	0.6673	0.667686

**Table 4.2** : Surface drag force  $Re^{1/2}C_{fx}$  and heat transfer rate  $Re^{-1/2}Nu_x$  for different values of  $\beta^*$ ,  $M$ ,  $\alpha^*$  and  $We$  when  $Pr = 1.5$ ,  $\gamma = 0.3$ ,  $\theta_w = 1.5$ ,  $Ec = 0.1$  and  $N_R = 1$ .

$M$	$We$	$\alpha^*$	$\beta^*$	$Re^{1/2}C_{fx}$		$Re^{-1/2}Nu_x$	
				$n = 0.75$	$n = 1.75$	$n = 0.75$	$n = 1.75$
0	3	0.3	0.001	-0.784896	-1.053800	0.500565	0.502467
			0.3	-0.806517	-1.090060	0.500368	0.502376
			0.6	-0.867699	-1.194930	0.499803	0.502112
			0.8	-0.926226	-1.298290	0.499255	0.501852
0.3	2			-0.831271	-1.012570	0.500599	0.501957
			3	-0.806517	-1.090060	0.500368	0.502376
			3.5	-0.795918	-1.125350	0.500266	0.502540
			4	-0.786367	-1.158540	0.500172	0.502682
0.3	3	0.3		-0.806517	-1.090060	0.500368	0.502370
			0.7	-0.427685	-0.490977	0.504149	0.504164
			1.3	0.505230	0.598867	0.501464	0.501690
			1.7	1.197720	1.827620	0.497663	0.499169
0.3	3	0.3	0.0	-0.806437	-1.090210	0.500367	0.502377
			0.2	-0.821804	-1.059190	0.500513	0.502218
			0.4	-0.836166	-1.024390	0.500645	0.502024
			0.6	-0.849679	-1.007155	0.500765	0.366731

**Table 4.3 :** Heat transfer rate  $Re^{-1/2}Nu_x$  for different values of  $\beta^*$ ,  $Pr$ ,  $\theta_w$ ,  $N_R$  and  $\gamma$  when  $M = 0.3$ ,  $\alpha^* = 0.3$ ,  $Ec = 0.1$  and  $We = 3$ .

$Pr$	$\theta_w$	$N_R$	$\gamma$	$\beta^*$	$Re^{-1/2}Nu_x$	
					$n = 0.75$	$n = 1.75$
2	1.5	0.7	0.2	0.001	0.273236	0.272824
4					0.266097	0.264471
6					0.258931	0.257190
8					0.253453	0.251803
2	1				0.181550	0.182882
	1.2				0.207981	0.208794
	1.4				0.247517	0.247571
	1.6				0.303518	0.302598
	1.5	1.7			0.435903	0.429010
		2.7			0.576677	0.564581
		3.7			0.711888	0.694991
		0.7	0.4		0.503225	0.511048
			0.6		0.645731	0.663615
			0.8		0.734863	0.760775
			0.2	0.0	0.273236	0.272824
				0.2	0.273218	0.272874
				0.4	0.273201	0.272930
				0.6	0.273184	0.224812
				0.8	0.273168	0.236665

## Chapter 5

# On Multiple Solutions of Carreau Fluid Flow over an Inclined Shrinking Sheet

This chapter presents the multiple solutions of a non-Newtonian Carreau fluid flow over a nonlinear inclined shrinking surface in presence of infinite shear rate viscosity. The governing boundary layer equations are derived for the Carreau fluid with infinite shear rate viscosity. The suitable transformations are employed to alter the leading partial differential equations to a set of ordinary differential equations. The consequential non-linear ODEs are solved numerically by an active numerical approach namely Runge-Kutta Fehlberg fourth-fifth order method accompanied by shooting technique. Multiple solutions are presented graphically and results are shown for various physical parameters. It is important to state that the velocity and momentum boundary layer thickness reduce with increasing viscosity ratio parameter in shear thickening fluid while opposite trend is observed for shear thinning fluid. Another important observation is that the wall shear stress is significantly decreased by the viscosity ratio parameter  $\beta^*$  for the first solution and opposite trend is observed for the second solution.

## 5.1 Mathematical Formulation

Here, we have discussed a two dimensional laminar steady boundary layer flow of an incompressible Carreau fluid flow over an inclined shrinking sheet which is inclined with an acute angle  $\alpha$ . The  $x$ -axis is along the sheet in the direction of motion and  $y$ -axis is normal to it. The sheet has uniform temperature  $T_w$  with  $T_\infty$  ( $T_w > T_\infty$ ) as the ambient fluid temperature and it is moving with a non-linear velocity  $U_w = bx^m$ . The parameters  $b$  and  $m$  ( $> 0$ ) are positive real numbers relating to the shrinking rate.

With Carreau fluid model and usual boundary layer approximations, the governing equations of mass, momentum and energy can be written as

$$\frac{\partial u}{\partial x} + \frac{\partial v}{\partial y} = 0, \quad (5.1)$$

$$\begin{aligned} u \frac{\partial u}{\partial x} + v \frac{\partial u}{\partial y} = & \nu \left( \frac{\partial^2 u}{\partial y^2} \right) \left[ \beta^* + (1 - \beta^*) \left\{ 1 + \Gamma^2 \left( \frac{\partial u}{\partial y} \right)^2 \right\}^{\frac{n-1}{2}} \right] \\ & + \nu(n-1)(1 - \beta^*) \Gamma^2 \left( \frac{\partial^2 u}{\partial y^2} \right) \left( \frac{\partial u}{\partial y} \right)^2 \left\{ 1 + \Gamma^2 \left( \frac{\partial u}{\partial y} \right)^2 \right\}^{\frac{n-3}{2}} \\ & + g\beta_T(T - T_\infty) \cos(\alpha), \end{aligned} \quad (5.2)$$

$$u \frac{\partial T}{\partial x} + v \frac{\partial T}{\partial y} = \alpha_1 \frac{\partial^2 T}{\partial y^2}. \quad (5.3)$$

The relevant momentum and thermal boundary conditions for the present problem are

$$u = -U_w = bx^m, \quad v = -v_w(x) \quad T = T_w \quad \text{at} \quad y = 0, \quad (5.4)$$

$$u \rightarrow 0, \quad T \rightarrow T_\infty \quad \text{as} \quad y \rightarrow \infty. \quad (5.5)$$

Now using the dimensionless variables (cf. Chapter 3, Eq. (3.7 – 3.8)) into Eqs. (5.1) to (5.3) and boundary conditions (5.4) and (5.5), one can get the following set of ordinary

differential equations

$$\left[ \beta^* + (1 - \beta^*) \left\{ 1 + We^2 (f'')^2 \right\}^{\frac{n-3}{2}} \left\{ 1 + nWe^2 (f'')^2 \right\} \right] f''' + ff'' - \left( \frac{2m}{m+1} \right) (f')^2 + Gr\theta \cos(\alpha) = 0, \quad (5.6)$$

$$\theta'' + Pr f\theta' = 0, \quad (5.7)$$

the corresponding boundary conditions

$$f(0) = s, \quad f'(0) = -1, \quad \theta(0) = 1, \quad (5.8)$$

$$f'(\infty) \rightarrow 0, \quad \theta(\infty) \rightarrow 0. \quad (5.9)$$

Further,  $Gr = \left( \frac{2}{m+1} \right) \frac{1}{b^2 x^{2m-1}} g\beta_T (T_w - T_\infty)$  is the local Grashof number and  $s = \frac{-v_w}{\sqrt{\frac{bv(m+1)}{2} x^{\frac{m-1}{2}}}} > 0$  the suction parameter.

### 5.1.1 Engineering Parameters of Interest

The parameters of engineering interest in the flow and heat transfer of Carreau fluid are the skin friction  $C_{fx}$  and the Nusselt number  $Nu_x$ . These parameters characterize as surface drag and wall heat transfer which can be defined

$$C_{fx} = \frac{\tau_w}{\rho U_w^2(x)}, \quad Nu_x = -\frac{x}{(T_w - T_\infty)} \left( \frac{\partial T}{\partial y} \right), \quad (5.10)$$

where  $\tau_w$  is given by

$$\tau_w = \mu_0 \left( \frac{\partial u}{\partial y} \right) \left[ \beta^* + (1 - \beta^*) \left\{ 1 + \Gamma^2 \left( \frac{\partial u}{\partial y} \right)^2 \right\}^{\frac{n-1}{2}} \right]. \quad (5.11)$$

Using the variables (5.11), we obtain

$$\begin{aligned}
\text{Re}_x^{1/2} C_{fx} &= \sqrt{\frac{m+1}{2}} f''(0) \left[ \beta^* + (1-\beta^*) \left\{ 1 + We^2 \left( f''(0) \right)^2 \right\}^{\frac{n-1}{2}} \right], \\
\text{Re}_x^{-1/2} Nu_x &= -\sqrt{\frac{m+1}{2}} \theta'(0).
\end{aligned} \tag{5.12}$$

## 5.2 Numerical Method and Validation

The nonlinear differential equations (5.6) and (5.7) with boundary conditions (5.8) and (5.9) have been solved numerically using Runge-Kutta Fehlberg fourth-fifth order method along with shooting technique. Thus, Eqs. (5.6) and (5.7) have been converted into first-order equations as follows:

$$y_1' = y_2, \tag{5.13}$$

$$y_2' = y_3, \tag{5.14}$$

$$y_3' = \frac{\left[ \left( \frac{2m}{m+1} \right) y_2^2 - y_1 y_3 - Gr \theta \cos(\alpha) \right]}{\beta^* + (1-\beta^*) \left[ 1 + nWe^2 y_3^2 \right] \left[ 1 + We^2 y_3^2 \right]^{\frac{n-3}{2}}}, \tag{5.15}$$

$$y_4' = y_5, \tag{5.16}$$

$$y_5' = -Pr y_1 y_5, \tag{5.17}$$

where  $y_1 = f$ ,  $y_2 = f'$ ,  $y_3 = f''$ ,  $y_4 = \theta$ ,  $y_5 = \theta'$  and boundary conditions (5.8) and (5.9) become

$$y_1(0) = s, \quad y_2(0) = -1, \quad y_2(\infty) = 0, \quad y_4(0) = 1, \quad y_4(\infty) = 0. \tag{5.18}$$

In view of the above boundary conditions, out of five only three initial conditions are known and we begin solution procedure by two initial guesses of  $f''(0)$  and  $\theta'(0)$  with the Newton-Raphson iteration to assure the iteration convergence required to satisfy asymptotically boundary conditions at infinity. Thus, in the present study the value of  $\eta = \eta_{\max}$  is taken to be 10 and step-size is taken to be  $\Delta\eta = 0.01$  with relative error tolerance  $10^{-5}$ . It is critical to take note that the dual solutions are attained by setting two different initial guesses for the



values of  $f''(0)$ , where both profiles (upper and lower solutions) satisfy the far field boundary conditions (5.9 and 5.10) asymptotically but with different shape.

### 5.3 Results and Discussion

In the present segment we will examine the behavior of skin friction coefficient, Nusselt number, velocity and temperature profiles for different values of developing parameter such as Weissenberg number  $We$ , power law index  $n$ , viscosity ratio parameter  $\beta^*$ , inclination angle  $\alpha$ , suction parameter  $s$  and Grashof number  $Gr$ .

Here, we assigned physically realistic numerical values to the controlling parameters with a particular true objective to get a knowledge about the momentum and thermal fields. For this we fixed  $We = 1.5$ ,  $n = 1.2$ ,  $\alpha = 30$ ,  $m = 2$ ,  $\beta^* = 0.1$ ,  $Gr = 1.5$ ,  $Pr = 1$  and  $s = 3$  as the default values. Scheme of skin friction coefficient and Nusselt number in contrast to distinctive estimations of physical parameter is displayed in **Figs. 5.1 – 5.5**. In actual, when we study the infinite shear rate viscosity in the case of shrinking sheet then eventually two solutions may appeared. **Fig. 5.1** shows the variation of skin friction coefficient verses  $s$  for power law index  $n$ . It is observed through this **Fig.** that dual solutions exist for  $s_c > s$ , where the critical values of  $s$  are  $s_c = 1.82181, 1.9810, 1.9066$ . Here, we can see that both the branches describe a decreasing behavior for increasing values of power law index  $n$ . Also we can see that increasing values of power law index  $n$  flourish the critical values. Through **Fig. 5.1** it is also noted that the solution does not exist for  $s_c < s$ .

**Fig. 5.2** discloses the effect of viscosity ratio parameter  $\beta^*$  on the skin friction coefficient in shrinking case. For both the situations, the critical values of  $s$  corresponding to several values of viscosity ratio parameter  $\beta^*$  are listed in this **Fig.** For the dual solution, it is seen through graphs that the skin friction decreases with the increase of viscosity ratio parameter. As a consequence of computations performed in this study, it is depicted from this **Fig.** that dual solutions exist for  $s_c = (1.9700, 1.9490, 1.9231)$  and where  $s_c > 1$  are the critical value of  $s$ , a point for which upper and lower solutions get together. We can also see that beyond  $s_c = (1.9700, 1.9490, 1.9231) < s$ , no solution exists because the boundary layer separates from the surface at a critical value ( $s_c$ ) beyond which the boundary layer approximation is not valid.

It is also observed that critical values decreases for increasing values of  $\beta^*$ .

**Fig. 5.3** depicts the behavior of  $\beta^*$  on Nusselt number. For the first solution, it is seen through graphs that the Nusselt number increases with the increase of viscosity ratio parameter. On the other hand, for second solution it can be observed that increasing viscosity ratio parameter decreases the Nusselt number. Dual solutions exist for  $s_c = (1.9700, 1.9490, 1.9231) > s$ . For  $s_c < s$  dual solutions does not exist. It can also seen that for increasing values of viscosity ratio parameter critical values decreases.

From **Fig. 5.4** we noticed that the increasing value of Weissenberg number  $We$  increases the skin friction coefficient for both the first and second solutions. Physically Weissenberg number is the ratio of the relaxation time of the fluid and the specific process time. It grows the thickness of fluid and that is why velocity of the fluid depreciates. Critical values of  $s$  in **Fig. 5.4** are  $s_c = 1.9139, 1.9229, 1.9329$ . Here solutions exist for  $s_c > s$ . While the opposite behavior was observed in **Fig. 5.5**. Increasing values of Weissenberg number reduce the Nusselt number in both first and second solutions. Dual solutions exist for  $s_c (= 1.9139, 1.9229, 1.9329) > s$ . It can also observed that for increasing values of Weissenberg number  $We$  critical value also increases.

**Figs. 5.6 – 5.9** are the velocity and temperature profiles for emerging parameters. Through **Fig. 5.6**, it portrays that when we increase  $We$ , temperature profile for both first and second solution presents the same increasing behavior. Physically  $We$  is the ratio of elastic forces and viscous forces, it enhances the thickness of fluid so temperature increases.

In **Fig. 5.7** dual velocity profiles are shown for suction parameter  $s = 2, 3$  and  $4$ . Consequently, we observed that in case of higher suction, there happens more separation between these two solutions. These plots designate that boost in the fluid velocity is marked with increasing values of the suction parameter  $s$  in case of first solution, whereas the fluid velocity decreases by enriching suction parameter for the second solution. Furthermore, a cautious perception of **Fig. 5.7** states that the thickness of boundary layer can be boosted with the growth of suction parameter  $s$ . Actually, the suction lessens the drag force to avoid the separation of boundary layer.

For completeness we have also included plots of the velocity field for varying values of the viscosity ratio parameter  $\beta^*$  examining both the first and second solutions. From **Fig. 5.8**,

we see the little dependence of the velocity field on  $\beta^*$ . Increasing  $\beta^*$  gives the reduction in velocity profile because  $\beta^*$  is a viscosity ratio parameter. It is sufficient to note that plots of velocity reveal quite the opposite trend with uplifting  $\beta^*$  when compared with those of the local Weissenberg number  $We$ .

**Fig. 5.9** shows in detail the characteristics of momentum layer for varying value of the Grashof number  $Gr$ . It is observed that uplifting values of  $Gr$  result in an increase in velocity and corresponding boundary layer thickness for first solution and for second solution a dual trend is noticed. Thickness of boundary layer increases near the wall and decreases beyond the wall. The Grashof number ( $Gr$ ) is a dimensionless number which approximates the ratio of the buoyancy to viscous force acting on a fluid. It frequently rises the fluid in both solutions.

The influence of inclination angle  $\alpha$  on velocity and temperature profile is presented in **Fig. 5.10**. In order to investigate the impact of the inclination angle  $\alpha$  on the boundary layer flow, we fix the value of emerging parameters and varying the value of  $\alpha$ , examining both the first and second solution. From **Figs. 5.10(a)** and **5.10(b)**, we noticed that increasing the values of the inclination angle  $\alpha$  decreases the velocity profiles while the opposite trend is observed for temperature profile. Physically increase in inclination angle decrease the buoyancy forces so velocity profile decreases.

**Table 5.1** is drawn for the different values of the suction parameter  $s$  to analyze the skin friction coefficient and local Nusselt number. It is observed from this table that the magnitude of both the skin friction and Nusselt number increases with the increase of suction parameter. Moreover, **Table 5.2** results are in good agreement with earlier works in particular cases and admirable agreement has been noted.

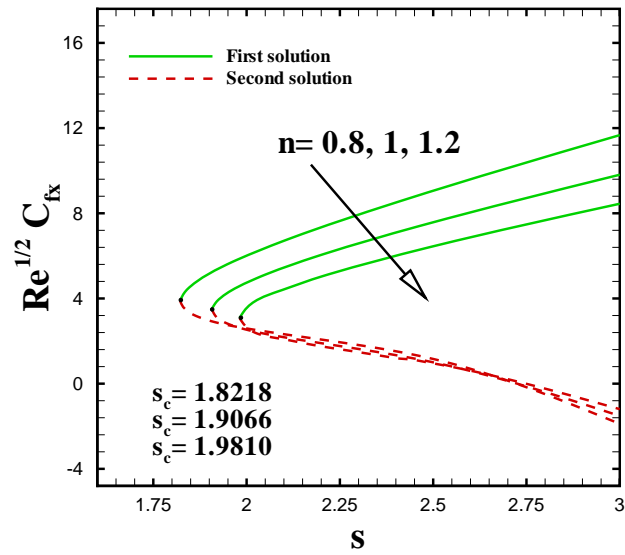


**Fig. 5.1 :** Effect of the power law index  $n$  on the wall shear stress  $Re^{1/2}C_{fx}$ .

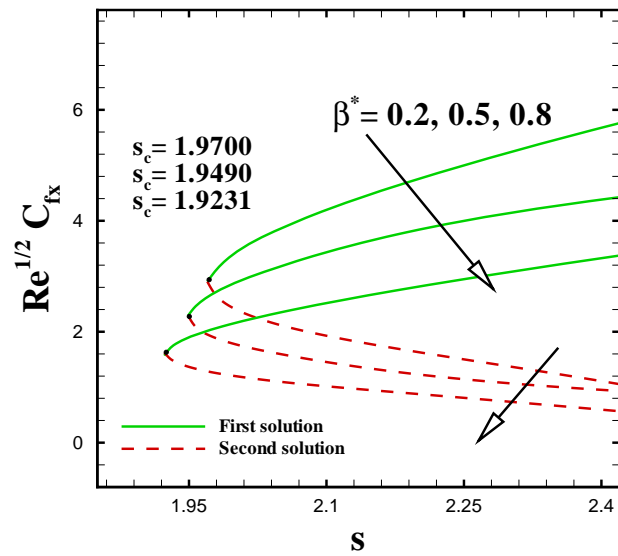


**Fig. 5.2 :** Effect of the viscosity ratio parameter  $\beta^*$  on the wall shear stress  $Re^{1/2}C_{fx}$ .

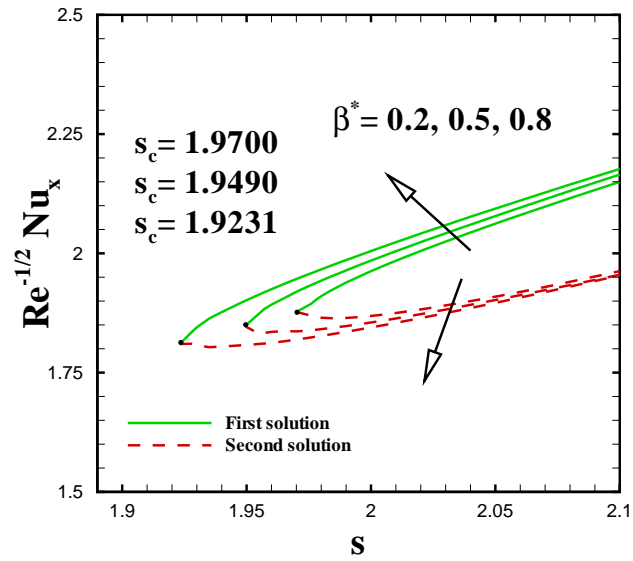


**Fig. 5.3** : Effect of the viscosity ratio parameter  $\beta^*$  the rate of heat transfer  $Re^{-1/2} Nu_x$ .

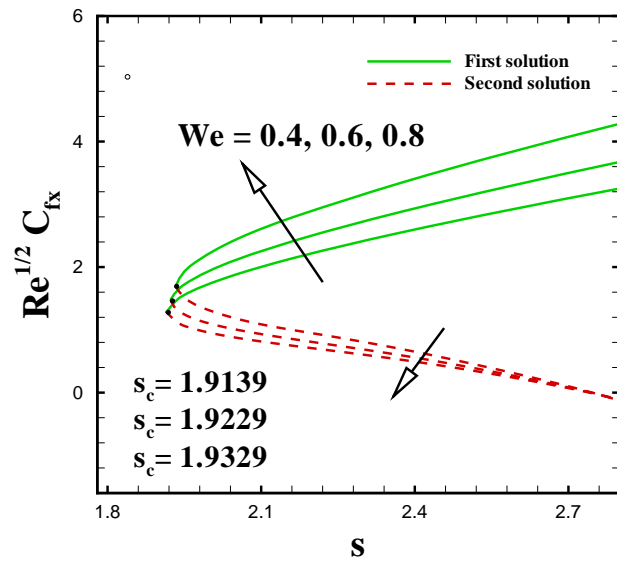


**Fig. 5.4** : Effect of the Weissenberg number  $We$  on the wall shear stress  $Re^{1/2} C_{fx}$ .

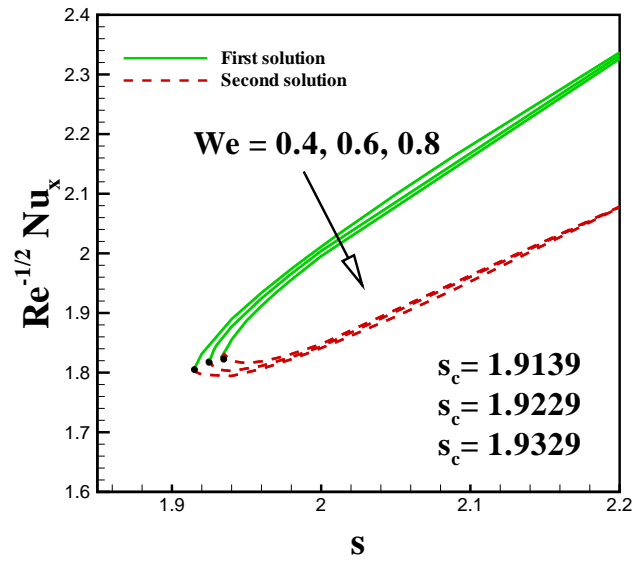


Fig. 5.5 : Effect of the Weissenberg  $We$  on the rate of heat transfer  $Re^{-1/2}Nu_x$ .

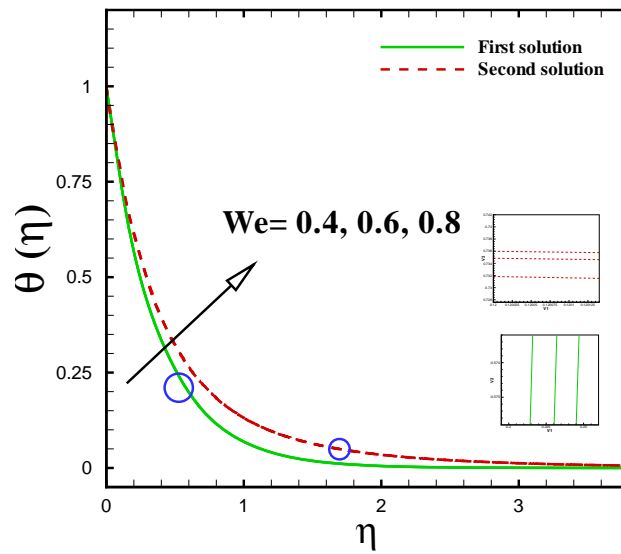


Fig. 5.6 : Effect of the Weissenberg  $We$  on the temperature profile  $\theta(\eta)$ .

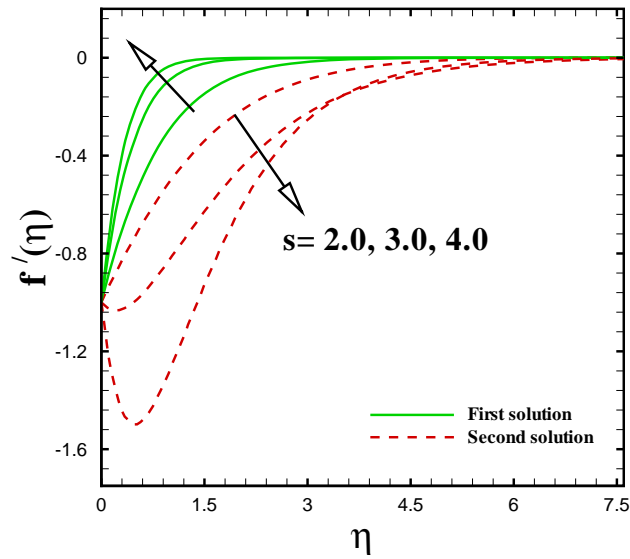


Fig. 5.7 : Effect of the suction parameter  $s$  on the velocity profile  $f'(\eta)$ .

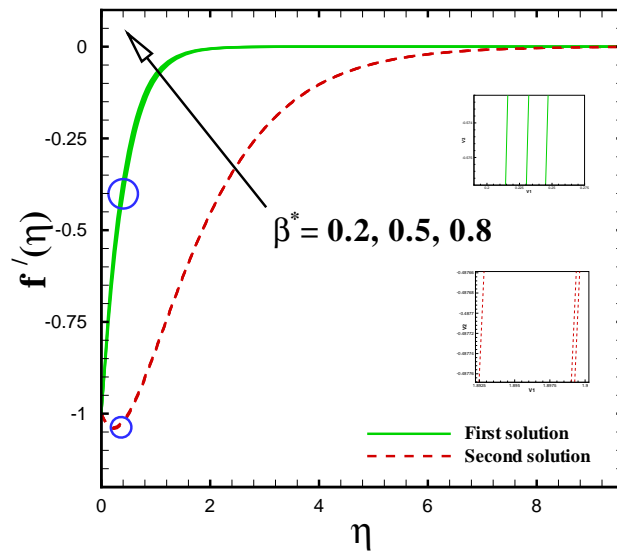


Fig. 5.8 : Effect of viscosity ratio parameter  $\beta^*$  on the velocity profile  $f'(\eta)$ .

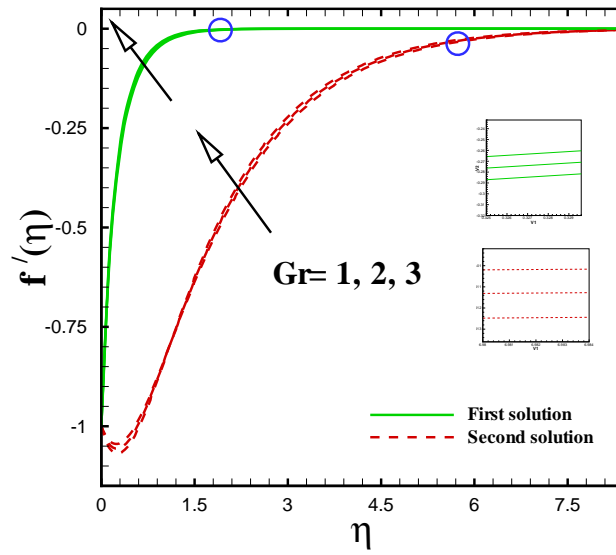


Fig. 5.9 : Effect of Grashof number  $Gr$  on the velocity profile  $f'(\eta)$ .

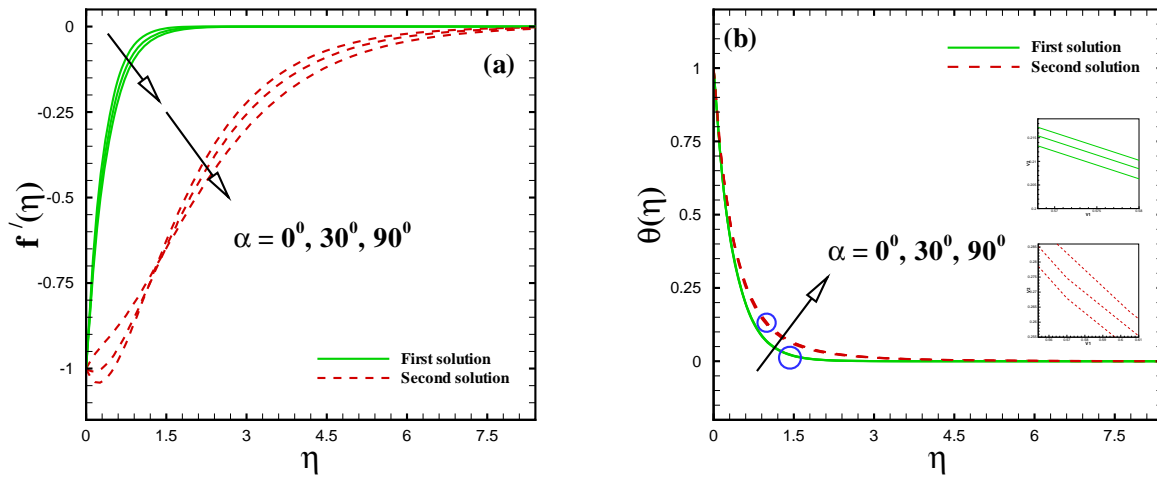


Fig. 5.10 : Effect of inclination angle  $\alpha$  on the velocity  $f'(\eta)$  and temperature  $\theta(\eta)$  profiles



**Table 5.1** : Analysis for skin friction and rate of heat transfer with  $We = 0$ ,  $m = 1$ ,  $Gr = 0$  and  $\alpha = 0$ .

$s$	$f''(0)$	$\theta'(0)$
2	0.9882	-1.5790
3	2.6180	-2.8137
4	3.7321	-3.8676

**Table 5.2** : Comparison of the results for the reduced Nusselt number  $-\theta'(0)$  when  $We = 0$ ,  $\alpha = 0$ ,  $m = 1$ ,  $n = 0$ ,  $\beta^* = 0$ ,  $Gr = 0$ , and  $s = 0$ .

Pr	Ref. [83]	Ref. [84]	Ref. [85]	Ref. [86]	Present study	
					First solution	Second solution
0.7	0.4539	0.4539	0.4539	0.454374	0.454501	0.377110
2.0	0.9113	0.9114	0.9114	0.911155	0.911411	0.881301
7.0	1.8954	1.8954	1.8954	1.822020	1.895400	1.880900

## Chapter 6

# Dual Solutions of Carreau Nanofluid Flow over an Inclined Shrinking Sheet

This chapter deals with the dual solutions of Carreau viscosity model over a shrinking sheet with infinite shear rate viscosity. The effects due to heat transfer mechanism along with the nano-particles are also considered with the thermophoresis and Brownian motion. The study is explored under the response of non-linear thermal radiation and heat generation/absorption. Moreover, convective boundary conditions are also taken into account. The governing equations are transformed into nonlinear ODEs by using suitable transformations. These developing leading non-linear equations have been solved numerically by means of Runge-Kutta Fehlberg method. The graphs of the velocity, temperature and concentration profiles are presented. Dual solutions are detected and exist for the shrinking sheet. Additionally, the critical values have been achieved by utilizing the plots of reduce skin friction and Nusselt number. The analysis reveals that the multiple solutions occurs for the certain choice of essential physical parameters; for example, suction parameter  $s$ , Grashof number  $Gr_1$ ,  $Gr_2$ , inclination angle  $\alpha$ , Lewis number  $Le$ , Brownian motion  $Nb$  and thermophoresis parameter  $Nt$ .

## 6.1 Geometry of the Physical Model

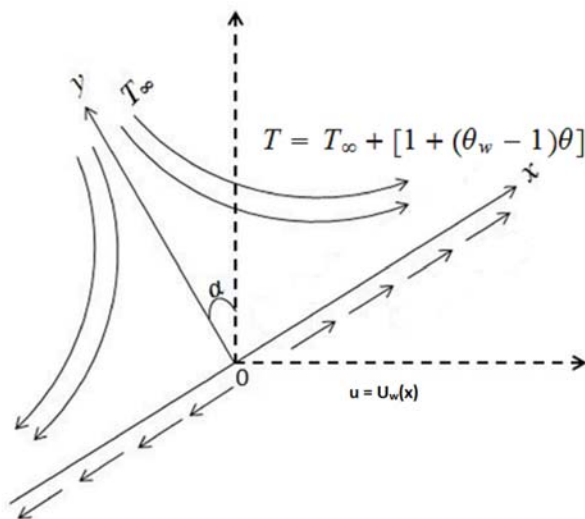


**Fig. 6.1** : Physical configuration of the system.

## 6.2 Mathematical Formulation

Consider a steady two-dimensional flow of an incompressible Carreau nanofluid over a inclined shrinking sheet which is inclined an acute angle  $\alpha$ . A cartesian coordinate system is employed in such a way that the  $x$ -axis is a coordinate measured along the shrinking sheet and the  $y$ -axis is occupied to be normal to the sheet. We assume that the shrinking sheet has a variable velocity  $U_w(x)$ . Furthermore, effects of heat and mass transfer are measured while the conditions at the surface are of convective type (see **Fig. 6.1**). Also behavior of thermal radiation and heat generation/absorption are taken into account. Moreover, flow analysis consists of Brownian motion and thermophoresis effects. Under the usual boundary layer and Rosseland approximations, the present flow problem is governed by the following equations:

$$\frac{\partial u}{\partial x} + \frac{\partial v}{\partial y} = 0, \quad (6.1)$$

$$\begin{aligned}
u \frac{\partial u}{\partial x} + v \frac{\partial u}{\partial y} &= \nu \left( \frac{\partial^2 u}{\partial y^2} \right) \left[ \beta^* + (1 - \beta^*) \left\{ 1 + \Gamma^2 \left( \frac{\partial u}{\partial y} \right)^2 \right\}^{\frac{n-1}{2}} \right] \\
&+ \nu(n-1)(1-\beta^*)\Gamma^2 \left( \frac{\partial^2 u}{\partial y^2} \right) \left( \frac{\partial u}{\partial y} \right)^2 \left\{ 1 + \Gamma^2 \left( \frac{\partial u}{\partial y} \right)^2 \right\}^{\frac{n-3}{2}} \\
&+ g\beta_T(T - T_\infty) \cos(\alpha) + g\beta_C(C - C_\infty) \cos(\alpha), \tag{6.2}
\end{aligned}$$

$$u \frac{\partial T}{\partial x} + v \frac{\partial T}{\partial y} = \alpha_1 \frac{\partial^2 T}{\partial y^2} - \frac{1}{\rho c_p} \frac{\partial q_r}{\partial y} + \frac{Q_0}{\rho c_p} (T - T_\infty) + \tau \left[ D_B \frac{\partial C}{\partial y} \frac{\partial T}{\partial y} + \frac{D_T}{T_\infty} \left( \frac{\partial T}{\partial y} \right)^2 \right], \tag{6.3}$$

$$u \frac{\partial C}{\partial x} + v \frac{\partial C}{\partial y} = D_B \frac{\partial^2 C}{\partial y^2} + \frac{D_T}{T_\infty} \frac{\partial^2 T}{\partial y^2}. \tag{6.4}$$

The boundary conditions related to the given problem are:

$$u = -U_w(x), \quad v = v_w, \quad -k \frac{\partial T}{\partial y} = h_f(T_f - T), \quad -D_B \frac{\partial C}{\partial y} = h_s(C_f - C) \quad \text{at } y = 0, \tag{6.5}$$

$$u \rightarrow 0, \quad T \rightarrow T_\infty, \quad C \rightarrow C_\infty \quad \text{as } y \rightarrow \infty. \tag{6.6}$$

By considering the dimensionless variables (Eq. (3.7 – 3.8) cf. Chapter 3), the momentum, energy and concentration equations are transformed as

$$\begin{aligned}
&\left[ \beta^* + (1 - \beta^*) \left\{ 1 + W e^2 (f'')^2 \right\}^{\frac{n-3}{2}} \left\{ 1 + n W e^2 (f'')^2 \right\} \right] f'''' + f f'' \\
&- \left( \frac{2m}{m+1} \right) (f')^2 + Gr_1 \theta \cos(\alpha) + Gr_2 \theta \cos(\alpha) = 0, \tag{6.7}
\end{aligned}$$

$$\theta'' + \frac{4}{3N_R} \frac{d}{d\eta} \left[ \{1 + (\theta_f - 1)\theta\}^3 \theta' \right] + \text{Pr} [f\theta' + Nb\phi'\theta' + Nt\theta'^2 + \delta\theta] = 0, \tag{6.8}$$

$$\phi'' + \text{Pr} \text{Le} f \phi' + \frac{Nt}{Nb} \theta'' = 0. \quad (6.9)$$

Here ( $\theta_f > 1$ ) is temperature ratio parameter,  $\delta = \frac{Q_0}{(\rho c)_p a}$  the internal heat parameter (where the heat source ( $\delta > 0$ ) or sink ( $\delta < 0$ )),  $Gr_1 = \left(\frac{2}{m+1}\right) \frac{1}{b^2 x^{2m-1}} g \beta_T (T_f - T_\infty)$  and  $Gr_2 = \left(\frac{2}{m+1}\right) \frac{1}{b^2 x^{2m-1}} g \beta_C (C_f - C_\infty)$  are the local Grashof numbers.

And the related boundary conditions (6.5) and (6.6) after using variables (Eq. (3.7 – 3.8) cf. Chapter 3) become

$$f(0) = s, \quad f'(0) = -1, \quad \theta'(0) = -\gamma [1 - \theta(0)], \quad \phi'(0) = -\gamma_1 [1 - \phi(0)], \quad (6.10)$$

$$f'(\infty) \rightarrow 0, \quad \theta(\infty) \rightarrow 0, \quad \phi(\infty) \rightarrow 0. \quad (6.11)$$

In above equation  $\gamma_1 = \frac{h}{D_B} \sqrt{\frac{v}{b}}$  is the mass Biot number.

### 6.2.1 Engineering Parameters of Interest

Here skin friction coefficient  $C_{fx}$ , Nusselt number  $Nu_x$  and Sherwood number  $Sh_x$  are

$$C_{fx} = \frac{\tau_w}{\rho U_w^2(x)}, \quad Nu_x = \frac{xq_w}{(T_f - T_\infty)}, \quad Sh_x = \frac{xq_m}{D_B(C_f - C_\infty)}, \quad (6.12)$$

where  $\tau_w$ ,  $q_w$  and  $q_m$  are given by

$$\begin{aligned} \tau_w &= \mu_0 \left( \frac{\partial u}{\partial y} \right) \left[ \beta^* + (1 - \beta^*) \left\{ 1 + \Gamma^2 \left( \frac{\partial u}{\partial y} \right)^2 \right\}^{\frac{n-1}{2}} \right], \\ q_w &= -k \left( \frac{\partial T}{\partial y} \right)_{y \rightarrow 0} + (q_r)_w, \quad q_m = -D_B \frac{\partial C}{\partial y}. \end{aligned} \quad (6.13)$$

Using the variables (6.13), we obtain

$$\text{Re}_x^{1/2} C_{fx} = \sqrt{\frac{m+1}{2}} f''(0) \left[ \beta^* + (1-\beta^*) \left\{ 1 + We^2 \left( f''(0) \right)^2 \right\}^{\frac{n-1}{2}} \right], \quad (6.14)$$

$$\text{Re}_x^{-1/2} Nu_x = -\theta'(0) \left\{ 1 + \frac{4}{3N_R} [1 + (\theta_w - 1)\theta(0)]^3 \right\}, \quad (6.15)$$

$$\text{Re}_x^{-1/2} Sh_x = -\sqrt{\frac{m+1}{2}} \phi'(0). \quad (6.16)$$

## 6.3 Numerical Results and Discussion

This segment shows the information of the validations and some physical outcomes. The detail of the effects of  $Gr_1$  and  $Gr_2$  on the flow, heat and mass transfer characteristics of Carreau nanofluid toward a shrinking sheet has been showed in this section . This empowers us to complete the numerical calculations for the velocity, temperature and concentration fields with the boundary layer for different values of the important parameters. For numerical investigation, we selected the values to relevant parameters as  $We = 1.5$ ,  $\alpha = 30^\circ$ ,  $m = 2$ ,  $n = 1.2$ ,  $\beta^* = 0.5$ ,  $Gr_1 = 1.5$ ,  $Gr_2 = 1.5$ ,  $Pr = 1$ ,  $N_R = 1$ ,  $Nt = 1$ ,  $Nb = 0.1$ ,  $\theta_w = 1.2$ ,  $Le = 1$ ,  $\gamma = 0.5$ ,  $\gamma_1 = 0.1$ ,  $\delta = 0.2$  and  $s = 3$ . We fixed these values in the whole study. It is observed that the governing system of differential equations hold multiple solutions. Therefore, it is very important to find out the critical range (knowingly critical values) corresponding to the leading parameters for the existence of multiple solutions.

### 6.3.1 Flow Characteristics

The given section describes the impact of different physical parameters on the flow characteristics. Important quantities like skin friction coefficient  $Re^{1/2}C_{fx}$  and the velocity profile  $f'(\eta)$  are presented for the different physical parameters like Grashof numbers  $Gr_1$  and  $Gr_2$ , inclination angle  $\alpha$ , viscosity ratio parameter  $\beta^*$ , Lewis number  $Le$ , nonlinear radiation parameter  $N_R$  and suction/injection parameter  $s$ . Our study reveals that there is a region  $s > 1$  for which unique solution exist and dual nature solution exists for the  $s > s_c$ . It is also mentioned that for  $s < s_c$  the given ordinary differential equations have no solution. Here  $s_c$  is the critical value of  $s$  also depending on other physical parameters.

**Figs. 6.2(a – b)** represent the paths of the local skin friction coefficient  $Re^{1/2}C_{fx}$  for the different values of the Grashof numbers  $Gr_1$  and  $Gr_2$ , while the other parameters are fixed. These figures show that multiple solution exists for different values of  $s_c > s$ . In **Fig. 6.2 (a)** as Grashof number goes from lower to higher values the local skin friction coefficient increases at the surface for first solution and opposite trend is observed for the lower branch solution. The critical values of the fixed parameters are  $s_c = 1.1222, 0.9830, 0.8520$  as Grashof number goes from 1.5, 2.5, 3.5. Similarly, in **Fig. 6.2 (b)** growing values of  $Gr_2$  shows a monotonically increase in the skin friction coefficient for the first solution and decrease for the second solution. The critical values of the fixed parameters are  $s_c = 1.1762, 1.0706, 0.9832$  as  $Gr_2$  increases from 1 – 3.

The non-dimensional velocity profiles  $f'(\eta)$  for different values of inclination angle  $\alpha$  and viscosity ratio parameter  $\beta^*$  are presented in **Figs. 6.3(a – b)**. In **Fig. 6.3 (a)** the dual velocity profile exist for different values of the inclination angle  $\alpha$  for  $s = 3$ . Dual profile shows increasing values of  $\alpha$  decreases the velocity profile for both first and second solution. It is noticed from **Fig. 6.3 (b)** that an increment in viscosity ratio parameter monotonically increases both the first and second solution.

**Figs. 6.4(a – b)** is the plot for different values of the  $Gr_1$  and  $Gr_2$ . In both the figures dual nature velocity profile exists. An increase in  $Gr_1$  and  $Gr_2$  increases the first solution and quite opposite trend is observed for the second solution. Moreover, momentum boundary layer thickness reduces in first solution and increases in the second solution.

Numerical results are presented through **Figs. 6.5(a – b)** for the velocity profile for different values of important parameters like Lewis number  $Le$  and suction parameter  $s$ . Here we have noticed dual nature velocity profiles in both the figures. It is observed from **Fig. 6.5 (a)** that for various values of Lewis number gives monotonically decrease in the first solution and this solution is physically feasible and stable while the second solution is definitely not. It is perceived from **Fig. 6.5 (b)** that as the suction parameter  $s$  is increased the non-dimensional velocity profile for the first solution while velocity profiles are depressed with higher values of  $s$  for second solution.

### 6.3.2 Thermal characteristics

In given section we presents the heat transfer characteristics for the Carreau nanofluid flow over a shrinking sheet. **Figs. 6.6 – 6.9** are drawn to see the impact of various physical parameters like inclination angle  $\alpha$ , viscosity ratio parameter  $\beta^*$ , nonlinear radiation parameter  $N_R$ , thermophoresis parameter  $Nt$ , suction parameter  $s$ , Prandtl number  $Pr$ , Grashof number  $Gr_1$  and  $Gr_2$  on the Nusselt number and temperature profile  $\theta(\eta)$ . With the help of these plots we depict the dual nature solution for the heat transfer mechanism for various values of the pertinent parameters as expressed above.

The trajectories of the Nusselt number  $Re^{-1/2}Nu_x$  for various Grashof numbers  $Gr_1$  and  $Gr_2$  are presented in **Figs. 6.6(a – b)** for the shrinking parameter  $s$ . These plots clearly indicate that dual nature of solutions exist for the specific Grashof numbers  $Gr_1 = 1.5, 2.5, 3.5$  and  $Gr_2 = 1, 2, 3$

As we observed that critical values of  $s_c$  are same as we have for in case of skin friction coefficient. The values of  $s_c$  corresponding to various values of  $Gr_1$  are 1.1222, 0.9830, 0.8520 in **Fig. 6.6 (a)** and critical values of  $Gr_2 = 1.1762, 1.0740, 0.9832$  in **Fig. 6.6 (b)**. It is stated that increasing values of Grashof number  $Gr_1$  increases the first and second solution and no similarity solution exist for  $s < s_c$ . It is clarified from **Fig. 6.6 (b)** that increasing values of  $Gr_2$  increases the first solution while in second solution Nusselt number  $Re^{-1/2}Nu_x$  depicts a decreasing behavior with stronger  $Gr_2$  at the boundary.

The influence of inclination angle  $\alpha$  and thermal Biot number  $\gamma$  is presented through **Fig. 6.7(a – b)** for fixed values of physical parameters. First solution increases by growing values of inclination angle  $\alpha$ . However when we consider the branches of second solution the temperature profile  $\theta(\eta)$  decreases with a rise in inclination angle  $\alpha$  within the thermal boundary layer. It is clear from **Fig. 6.7 (b)** that increasing values of thermal Biot number  $\gamma$  increases both the first and second solution of the temperature profile  $\theta(\eta)$ .

In **Fig. 6.8 (a)** the dual nature behavior is observed on the temperature profile  $\theta(\eta)$  for nonlinear radiation parameter  $N_R$ . It is observed that growing values of  $N_R$  reduces the temperature profile  $\theta(\eta)$  and also the thermal boundary layer thickness becomes thinner for both the first and second solution. Graphical representation of **Fig. 6.8 (b)** shows the enhance in temperature profile within the boundary layer for increasing values of thermophoresis parameter



$Nt$  for both first and second solution.

The suction is very important phenomena to retain the steady flow adjacent the sheet by delaying the separation. The effects of suction parameter are essential in investigative as well as practical point of view. **Fig. 6.9 (a)** demonstrates the temperature profile  $\theta(\eta)$  for different values of suction parameter  $s$ . From this figure it is observed that temperature profile decreases by increasing values of  $s$  from 2 – 4 for both the first and second solution. Similarly in **Fig. 6.9 (b)** increasing values of  $Pr$  decreases the temperature profile for both the first and second solution.

### 6.3.3 Concentration characteristics

Here we will discuss the different outcomes of the pertinent parameters on the concentration profile  $\phi(\eta)$ . In case of shrinking sheet dual solution exist for the concentration profile  $\phi(\eta)$  with fixed parameters. The nanoparticles concentration at the wall is represented by **Figs. 6.10(a – b)** to see the impact of  $Gr_1$  and  $Gr_2$  against the suction parameter  $s$ . For the Sherwood number critical values of  $s$  are same as we have for skin friction coefficient and Nusselt number. In **Fig. 6.10 (a)** increasing values of  $Gr_1$  uplifting the first solution as well as second solution. It is clear from **Fig. 6.10 (b)** that up growing values of  $Gr_2$  gives increasing behavior for the first solution and shows opposite trend for the second solution.

**Figs. 6.11(a – b)** are the plots of the concentration profile  $\phi(\eta)$  against the nonlinear radiation  $N_R$  and thermophoresis parameter  $Nt$ . Increasing values of  $N_R$  makes the reduction in concentration profile  $\phi(\eta)$  for both the first and second solution. While, increasing values of  $Nt$  shows the increase in concentration profile  $\phi(\eta)$  for upper and lower branch solution. To see the impact of Prandtl number  $Pr$  and suction parameter  $s$  on the concentration profile  $\phi(\eta)$  we have made the **Figs. 6.12(a – b)**. In **Fig. 6.12 (a)** increasing values of  $Pr$  gives reduction in concentration profile  $\phi(\eta)$  for both the upper and lower branch solution. Similarly, in **Fig. 6.12 (b)** increasing values of suction parameter  $s$  gives decrement in concentration profile  $\phi(\eta)$ .

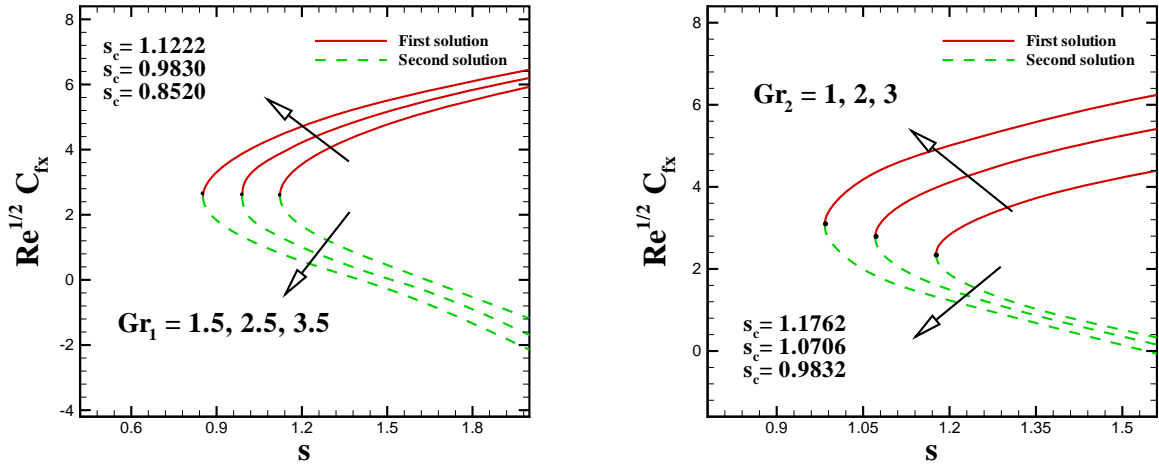


Fig. 6.2 : Effect of the Grashof number  $Gr_1$  and  $Gr_2$  on the wall shear stress  $Re^{1/2}C_{fx}$ .

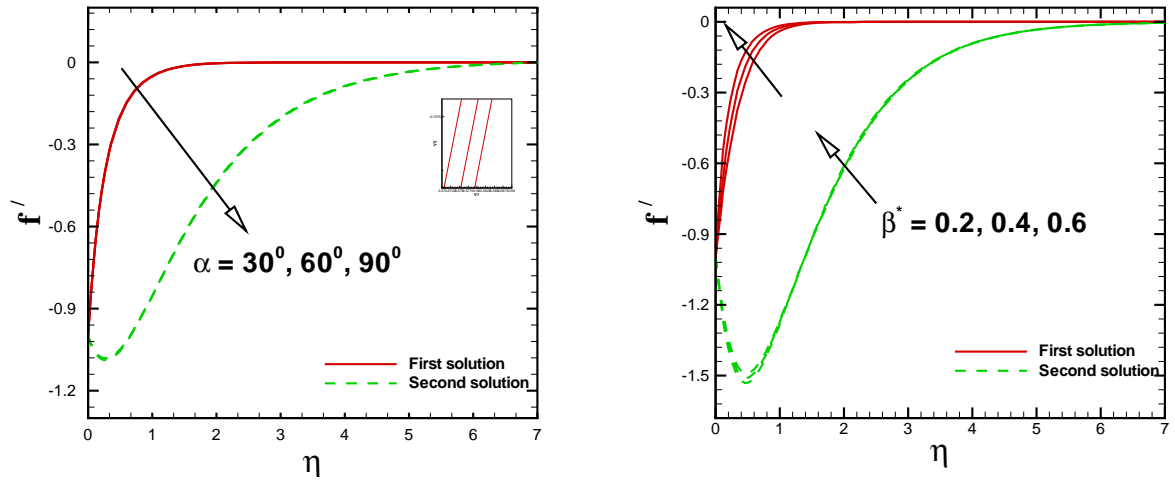
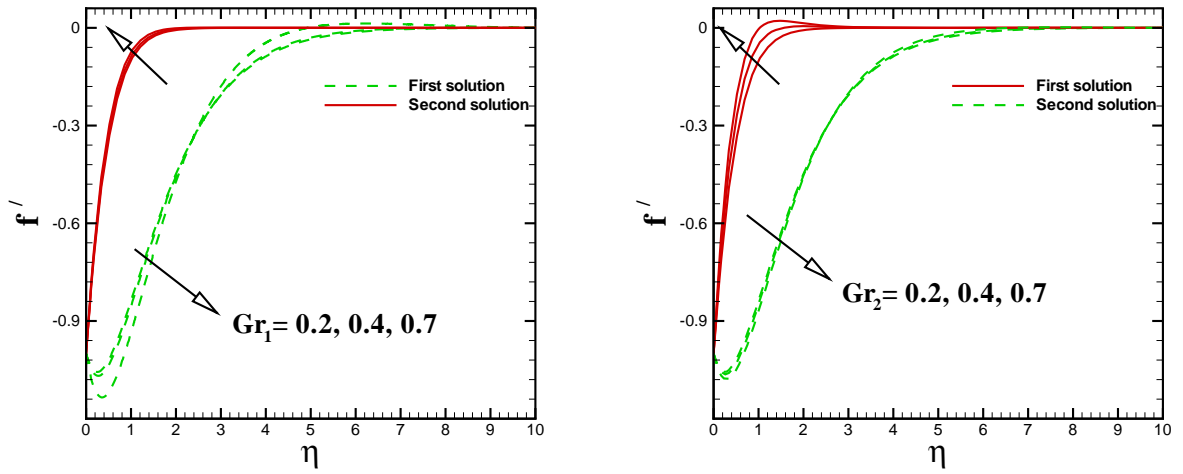
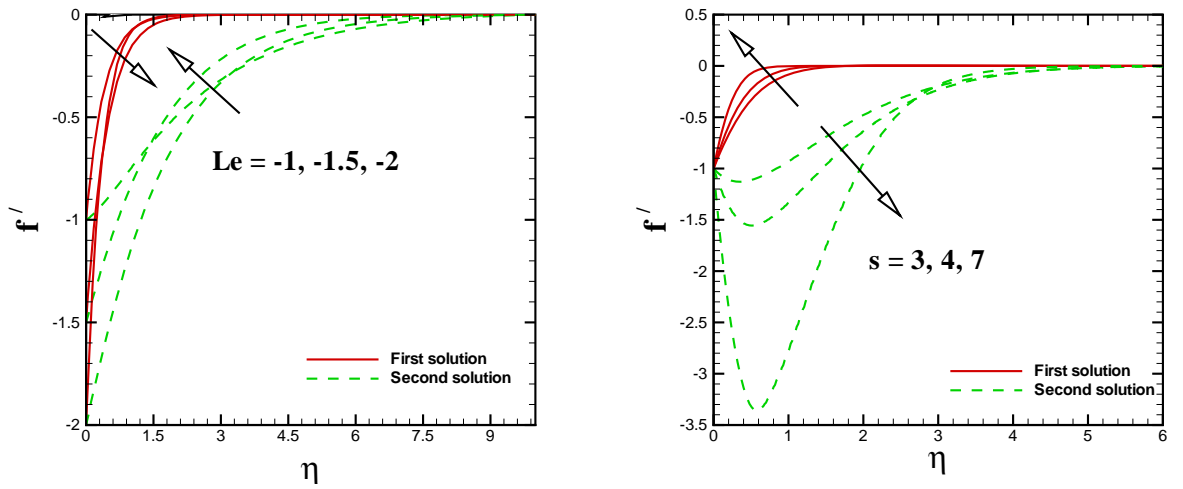


Fig. 6.3 : Effect of the inclination angle  $\alpha$  and viscosity ratio parameter  $\beta^*$  on velocity profile  $f'(\eta)$ .



**Fig. 6.4 :** Effect of the Grashof number  $Gr_1$  and  $Gr_2$  the on velocity profile  $f'(\eta)$ .



**Fig. 6.5 :** Effect of the Lewis number  $Le$  and suction parameter  $s$  on velocity profile  $f'(\eta)$ .

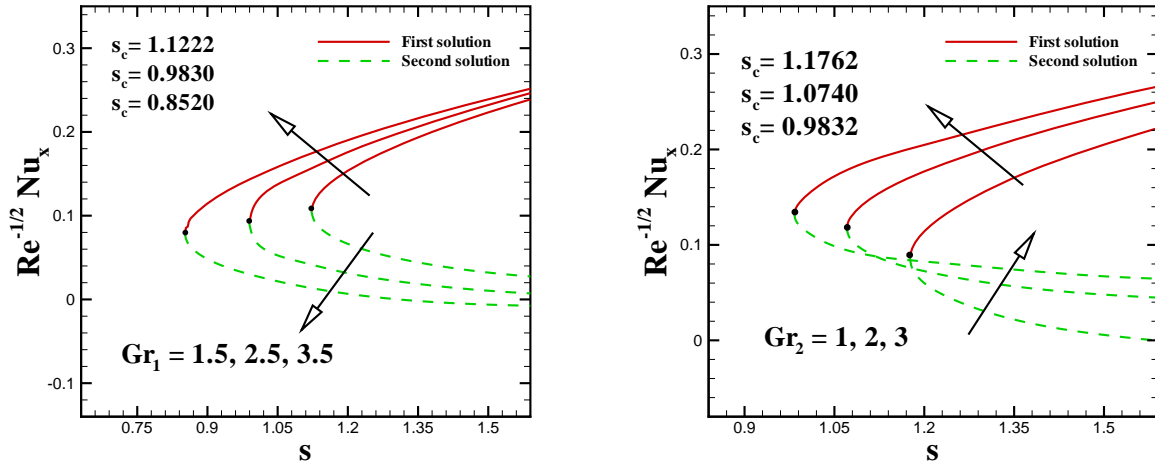


Fig. 6.6 : Effect of the Grashof number  $Gr_1$  and  $Gr_2$  on the Nusselt number  $Re^{-1/2}Nu_x$ .

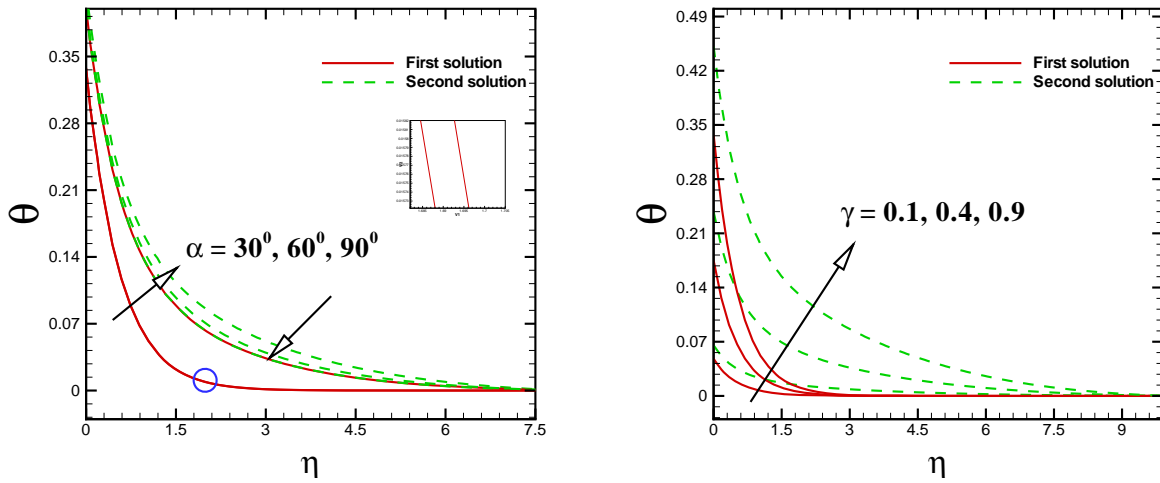
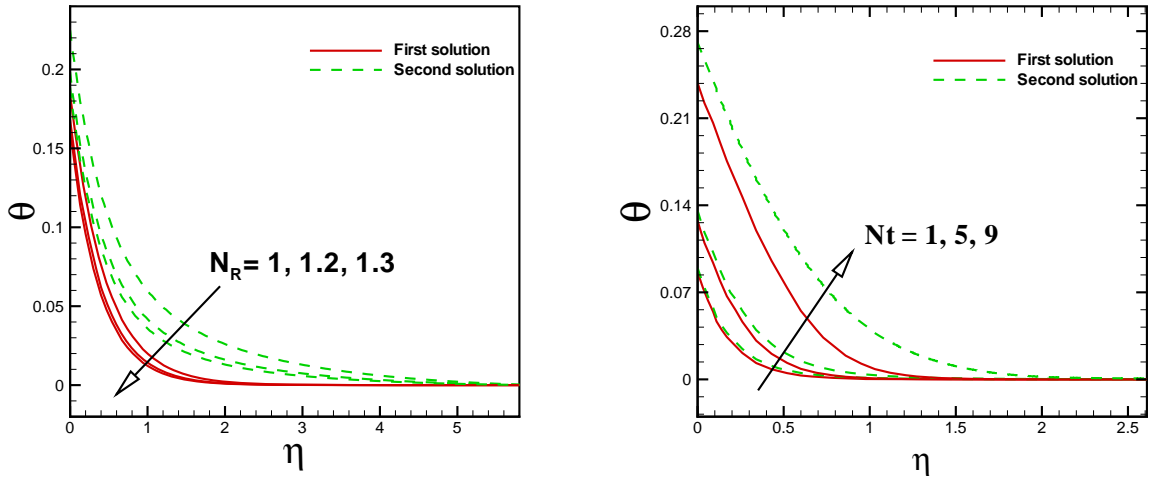
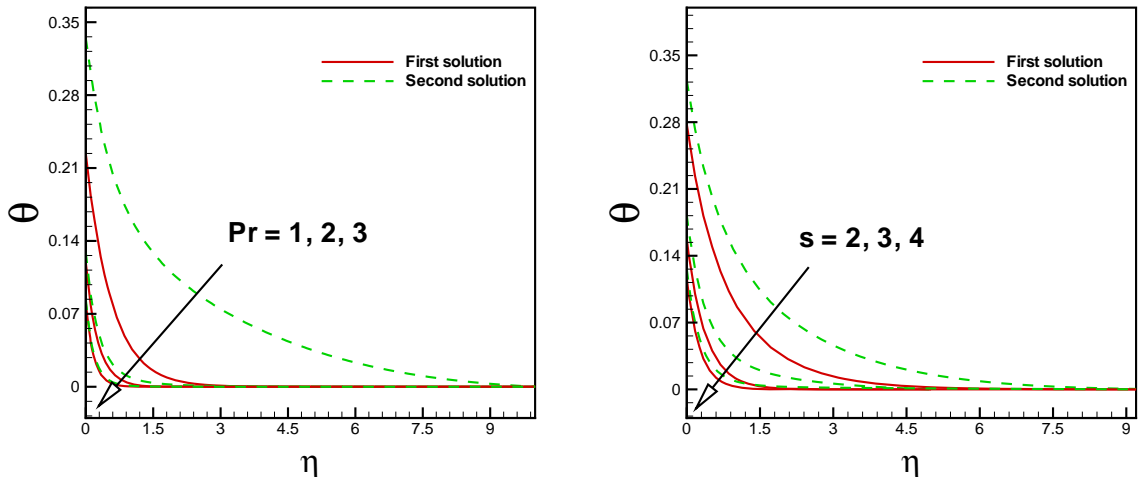


Fig. 6.7 :Effect of the inclination angle  $\alpha$  and thermal Biot number  $\gamma$  on the temperature profile  $\theta(\eta)$ .



**Fig. 6.8 :** Effect of nonlinear radiation parameter  $N_R$  and thermophoresis parameter  $Nt$  on temperature profile  $\theta(\eta)$ .



(6.17)

**Fig. 6.9 :** Effect of Prandtl number  $Pr$  and suction parameter  $s$  on temperature profile  $\theta(\eta)$ .

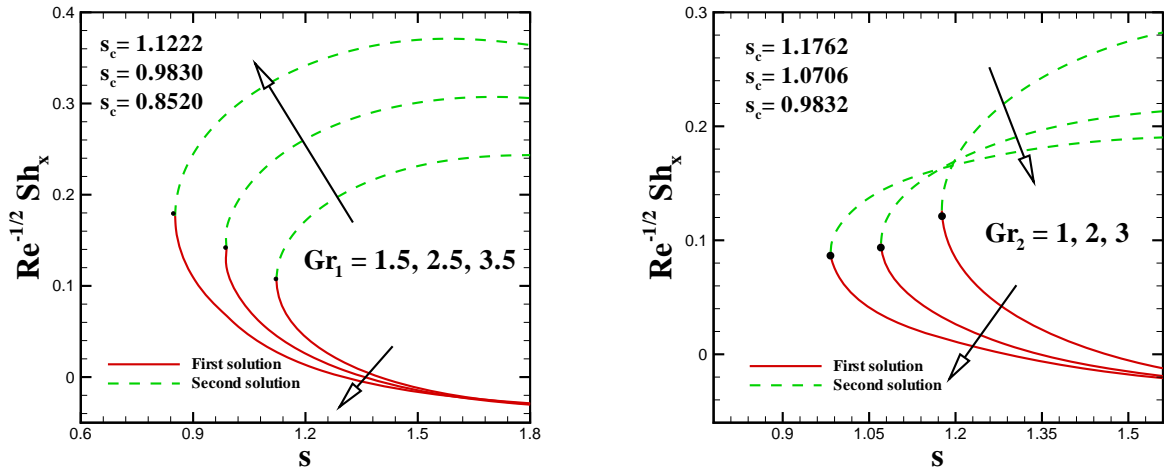


Fig. 6.10 : Effect of the Grashof number  $Gr_1$  and  $Gr_2$  on the Sherwood number  $Re^{-1/2}Sh_x$ .

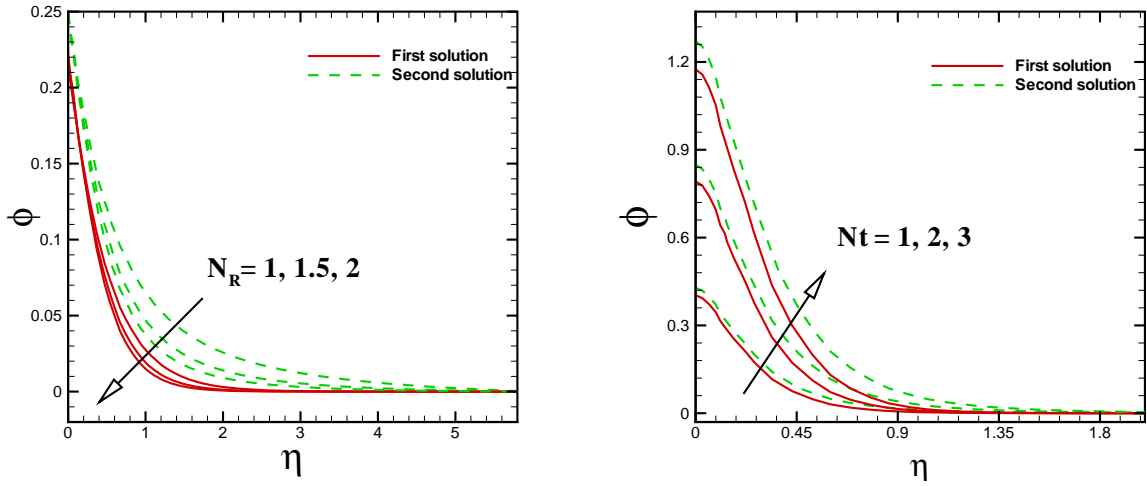
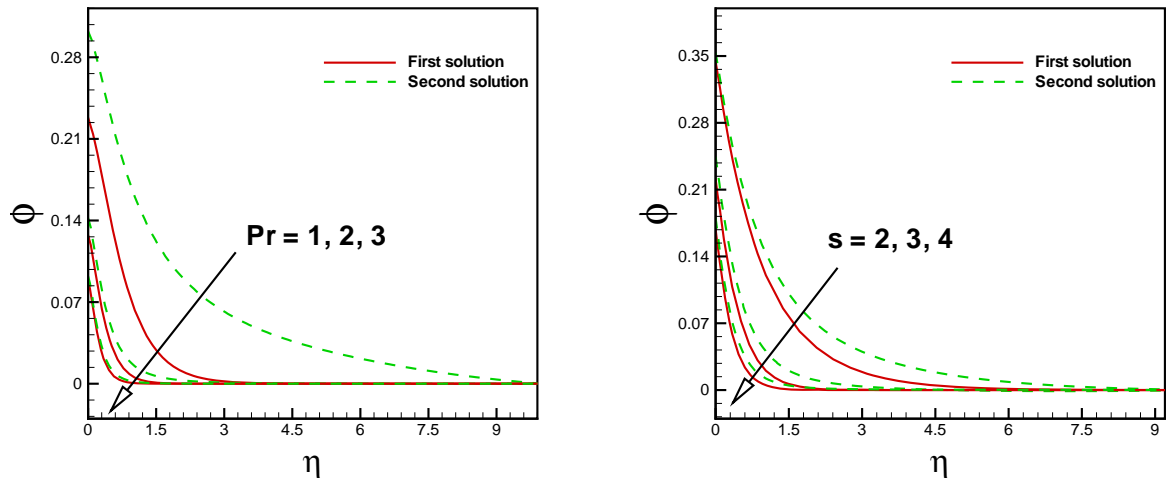


Fig. 6.11 : Effect of nonlinear radiation parameter  $N_R$  and thermophoresis parameter  $Nt$  on concentration profile  $\phi(\eta)$ .



**Fig. 6.12 :** Effect of Prandtl number  $Pr$  and suction parameter  $s$  on concentration profile  $\phi(\eta)$ .

## Chapter 7

# Multiple Solutions with Cattaneo–Christov Double-Diffusion Model of Carreau Fluid Flow

This chapter considered a numerical computation for multiple solutions near by the stagnation point flow of Carreau viscosity model past a shrinking sheet with infinite shear rate viscosity. Energy and concentration equations are developed with the help of theory of Cattaneo-Christov double diffusion. Such diffusions are established as a part of expressing the solutal and thermal relaxation times framework. The emerging leading non-linear equations have been solved numerically by means of Runge-Kutta Fhelberg method. The obtained numerical results have been displayed graphically and some exciting features like multiple solutions are established. The critical values are computed for the suction and shrinking parameters. Moreover, the critical values have been attained by using the plots of reduced skin friction. This study discloses that the multiple solutions occur for the different essential physical parameters for example suction parameter  $s$ , stretching/shrinking parameter  $\lambda$ , magnetic parameter  $M$ , Prandtl number  $Pr$ , velocity slip parameter  $\delta_1$ , viscosity ratio parameter  $\beta^*$ , Schmidt number  $Sc$ , non-dimensional thermal relaxation time  $\delta_e$  and non-dimensional solutal relaxation time  $\delta_c$ .



## 7.1 Geometry of the Physical Model

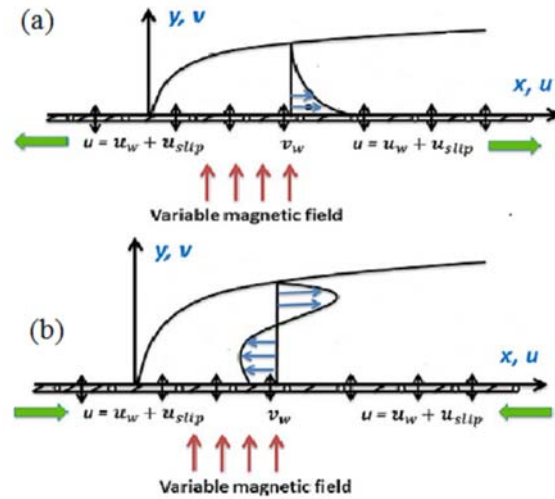


Fig. 7.1 : Physical model of the problem (a) stretching sheet and (b) shrinking sheet

## 7.2 Problem Formulation

### 7.2.1 Flow Equation

Let us consider a stagnation point flow of Carreau fluid past a shrinking sheet. The stretching velocity of the sheet is nonlinear as  $U_w(x) = bx$  (stretching sheet) and  $U_w(x) = -bx$  (shrinking sheet) where  $b$  is constant. Moreover,  $v_w(x) = v(x)$  and  $U_\infty(x) = cx$  are the mass flux velocity and free stream velocity, respectively in which  $c$  is a constant. We take the steady two-dimensional flow of Carreau fluid model with following assumptions:

- (1) Velocity slip
- (2) Incompressible fluid
- (3) MHD
- (4) Cattaneo-Christov double diffusion model for heat and mass flux

The continuity and momentum equations after boundary layer approximations can be expressed as:

$$\frac{\partial u}{\partial x} + \frac{\partial v}{\partial y} = 0, \quad (7.1)$$

$$\begin{aligned} u \frac{\partial u}{\partial x} + v \frac{\partial u}{\partial y} &= U_\infty \frac{dU_\infty}{dx} + \nu \left( \frac{\partial^2 u}{\partial y^2} \right) \left[ \beta^* + (1 - \beta^*) \left\{ 1 + \Gamma^2 \left( \frac{\partial u}{\partial y} \right)^2 \right\}^{\frac{n-1}{2}} \right] \\ &+ \nu(n-1)(1-\beta^*)\Gamma^2 \left( \frac{\partial^2 u}{\partial y^2} \right) \left( \frac{\partial u}{\partial y} \right)^2 \left\{ 1 + \Gamma^2 \left( \frac{\partial u}{\partial y} \right)^2 \right\}^{\frac{n-3}{2}} \\ &+ \frac{\sigma B_0^2}{\rho} (U_\infty - u), \end{aligned} \quad (7.2)$$

subject to appropriate boundary conditions

$$u = U_w(x) + u_{slip}, \quad v = v_w(x) \quad \text{at} \quad y = 0, \quad (7.3)$$

$$u \rightarrow U_\infty(x), \quad \text{as} \quad y \rightarrow \infty. \quad (7.4)$$

We assume the partial slip at the wall as  $u_{slip} = L \frac{\partial u}{\partial y} \left[ 1 + \Gamma^2 \left( \frac{\partial u}{\partial y} \right)^2 \right]^{\frac{n-1}{2}}$ , where  $L$  is the velocity slip factor.

The dimensionless quantities (Eq. (4.9) cf. Chapter 4) are utilized to change the governing partial differential equations into a scheme of ordinary differential equations thus Eq. (7.2) becomes

$$\begin{aligned} &\left[ \beta^* + (1 - \beta^*) \left\{ 1 + We^2 (f'')^2 \right\}^{\frac{n-3}{2}} \left\{ 1 + nWe^2 (f'')^2 \right\} \right] f''' + f f'' \\ &- (f')^2 + 1 + M^2(1 - f') = 0, \end{aligned} \quad (7.5)$$

with the related boundary conditions

$$f(0) = s, \quad f'(0) = \lambda + \delta_1 f''(0) (1 + We^2 (f''(0)^2))^{\frac{n-1}{2}}, \quad f'(\infty) \rightarrow 1, \quad (7.6)$$

where  $s = \frac{-v_w}{\sqrt{c\nu}}$  the mass transfer parameter and  $\delta_1 = L \sqrt{\frac{c}{\nu}}$  the velocity slip parameter.

## 7.2.2 Energy and Concentration Equations

The relevant energy and concentration equations are

$$\rho c_p \left( u \frac{\partial T}{\partial x} + v \frac{\partial T}{\partial y} \right) = -\nabla \cdot \mathbf{q}, \quad (7.7)$$

$$u \frac{\partial C}{\partial x} + v \frac{\partial C}{\partial y} = -\nabla \cdot \mathbf{J}. \quad (7.8)$$

The Cattaneo-Christov heat and mass flux fulfill the following relations

$$\mathbf{q} + \lambda_e \left[ \frac{\partial \mathbf{q}}{\partial t} + \mathbf{V} \cdot \nabla \mathbf{q} - \mathbf{q} \cdot \nabla \mathbf{V} + (\nabla \cdot \mathbf{V}) \mathbf{q} \right] = -k \nabla T, \quad (7.9)$$

$$\mathbf{J} + \lambda_c \left[ \frac{\partial \mathbf{J}}{\partial t} + \mathbf{V} \cdot \nabla \mathbf{J} - \mathbf{J} \cdot \nabla \mathbf{V} + (\nabla \cdot \mathbf{V}) \mathbf{J} \right] = -D \nabla C. \quad (7.10)$$

Here for  $\lambda_c = 0$  and  $\lambda_e = 0$  the above equations regain laws due to Fourier and Fick. For an incompressible and steady fluid the above reduce to

$$\mathbf{q} + \lambda_e [\mathbf{V} \cdot \nabla \mathbf{q} - \mathbf{q} \cdot \nabla \mathbf{V}] = -k \nabla T, \quad (7.11)$$

$$\mathbf{J} + \lambda_c [\mathbf{V} \cdot \nabla \mathbf{J} - \mathbf{J} \cdot \nabla \mathbf{V}] = -D \nabla C. \quad (7.12)$$

Thus Eqs. (7.7), (7.8), (7.11) and (7.12) are transformed as

$$\begin{aligned} u \frac{\partial T}{\partial x} + v \frac{\partial T}{\partial y} + \lambda_e [u^2 \frac{\partial^2 T}{\partial x^2} + v^2 \frac{\partial^2 T}{\partial y^2} + (u \frac{\partial u}{\partial x} + v \frac{\partial u}{\partial y}) \frac{\partial T}{\partial x} \\ + 2uv \frac{\partial^2 T}{\partial x \partial y} + (u \frac{\partial v}{\partial x} + v \frac{\partial v}{\partial y}) \frac{\partial T}{\partial y}] = \alpha_1 \frac{\partial^2 T}{\partial y^2}, \end{aligned} \quad (7.13)$$

$$\begin{aligned} u \frac{\partial C}{\partial x} + v \frac{\partial C}{\partial y} + \lambda_c [u^2 \frac{\partial^2 C}{\partial x^2} + v^2 \frac{\partial^2 C}{\partial y^2} + (u \frac{\partial u}{\partial x} + v \frac{\partial u}{\partial y}) \frac{\partial C}{\partial x} \\ + 2uv \frac{\partial^2 C}{\partial x \partial y} + (u \frac{\partial v}{\partial x} + v \frac{\partial v}{\partial y}) \frac{\partial C}{\partial y}] = D \frac{\partial^2 C}{\partial y^2}. \end{aligned} \quad (7.14)$$

The relevant boundary conditions are

$$T = T_w, \quad C = C_w \quad \text{at } y = 0, \quad (7.15)$$

$$T \rightarrow T_\infty, \quad C \rightarrow C_\infty \quad \text{as } y \rightarrow \infty. \quad (7.16)$$

Defining the following variables

$$\theta(\eta) = \frac{T - T_\infty}{T_f - T_\infty}, \quad \phi(\eta) = \frac{C - C_\infty}{C_f - C_\infty}, \quad (7.17)$$

we finally reached at

$$\theta'' + \text{Pr} f \theta' - \text{Pr} \delta_e (f f' \theta' + f^2 \theta'') = 0, \quad (7.18)$$

$$\phi'' + Sc f \phi' - Sc \delta_c (f f' \phi' + f^2 \phi'') = 0, \quad (7.19)$$

$$\theta(0) = 1, \quad \phi(0) = 1 \quad \text{as } \eta \rightarrow 0, \quad (7.20)$$

$$\theta(\infty) \rightarrow 0, \quad \phi(\infty) \rightarrow 0 \quad \text{as } \eta \rightarrow \infty, \quad (7.21)$$

where  $\delta_e = \lambda_e c$  is the non-dimensional thermal relaxation time,  $\delta_c = \lambda_c c$  the non-dimensional solutal relaxation time and  $Sc = \frac{\nu}{D}$  the Schmidt number.

### 7.2.3 Engineering Parameters of Interest

The skin friction coefficient  $C_{fx}$  is defined as

$$C_{fx} = \frac{\tau_w}{\rho U_w^2(x)}, \quad (7.22)$$

where  $\tau_w$  is the surface shear stress and is given by

$$\tau_w = \mu_0 \left( \frac{\partial u}{\partial y} \right) \left[ \beta^* + (1 - \beta^*) \left\{ 1 + \Gamma^2 \left( \frac{\partial u}{\partial y} \right)^2 \right\}^{\frac{n-1}{2}} \right], \quad (7.23)$$

Using Eq. (7.23), we obtain

$$\text{Re}_x^{1/2} C_{fx} = f''(0) \left[ \beta^* + (1 - \beta^*) \left\{ 1 + We^2 \left( f''(0) \right)^2 \right\}^{\frac{n-1}{2}} \right], \quad (7.24)$$

### 7.3 Results Validation and Discussion

This section provides the validation and information of different physical outcomes. The impact of stagnation point, partial slip condition, MHD and viscosity ratio parameter on flow, heat and mass transfer properties of an electrically conducted Carreau fluid over a shrinking surface has been discussed. The results which are given by plots are utilized to achieve a parametric study of the non-dimensional parameters, specifically the magnetic parameter  $M$ , shrinking parameter  $\lambda$ , suction parameter  $s$ , Weissenberg number  $We$ , Prandtl number  $Pr$ , viscosity ratio parameter  $\beta^*$ , solutal relaxation time  $\delta_c$  and thermal relaxation time  $\delta_e$ . For numerical examination, we allotted the values to the controlling parameters as  $We = 0.5$ ,  $n = 1.2$ ,  $\beta^* = 0.9$ ,  $s = 3$ ,  $Pr = 1$ ,  $M = 0.3$ ,  $\delta_1 = 0.1$ ,  $Le = 1$ ,  $\delta_e = 0.2$ ,  $\delta_c = 0.2$  and  $s = 3$ . We fixed these values in the whole study except the plots and table wherein they are mentioned. Dual solutions are presented with the main aim of the critical values of the pertaining parameters. First (upper) and second (lower) solutions are represented by solid and dashed lines, respectively.

#### 7.3.1 Validation of Numerical Outcomes

To confirm the validity and consistency of numerical results, we conducted a numerical comparison between the obtained results and previously published data. These comparison can be found in **Tables 7.1** and **7.2** with Wang [87], Yacob and Ishak [88] and Golra Gireesha [89] for different values of shrinking parameters. In **Tables 7.1** and **7.2** results of skin friction are validated against the published work for different values of shrinking parameter  $\lambda$  with excellent agreement.

### 7.3.2 Flow Characteristics

The attained numerical results pertaining to these figures show that dual solutions exist for certain choice of shrinking parameter  $\lambda$  which further depends on viscosity ratio parameter  $\beta^*$  and magnetic parameter  $M$ . It is also observed that when value of  $\lambda$  is equal to a specific value say critical value then there is only one solution. Solution exists till the critical value and no solution can be found  $\lambda < \lambda_c^*$ . From **Fig. 7.2**, it is noticeable that skin friction decreases for an increase in viscosity ratio parameter  $\beta^*$ . It is depicted from this **Fig.** that dual solutions exist for  $\lambda_c^* = -2.0441, -2.0600, -2.0944$ . Moreover, we can also noticed that beyond the values of  $\lambda_c^* = -2.0441, -2.0600, -2.0944$  no solution exists because the boundary layer separates from the surface at the critical value ( $\lambda_c^*$ ) beyond which the boundary layer approximation is not valid. The critical values of  $\lambda$  decreases as viscosity ratio parameter  $\beta^*$  goes from 0.4 to 0.9. **Fig. 7.3** makes clear that the enhancement in magnetic parameter  $M$  gives a quick monotonic increase in the local skin friction. Physically, this is because of the fact that the execution of magnetic field creates enhancement in drag force.

The non-dimensional velocity profiles  $f'(\eta)$  for diverse values of magnetic parameter  $M$  and suction parameter  $s$  are explained in **Figs. 7.4** and **7.5**. It is inferred from **Fig. 7.4** that rise in magnetic parameter  $M$  increases the first solution but quite the opposite behavior is observed for the second branch solution. Moreover, thickness of momentum boundary layer declines in the case of upper solution whereas it boosts for the second solution. Physically, this is because of the Lorentz force. An increase in magnetic field rises the Lorentz force and hence, accelerate the first solution. The inverse is true for the second solution. According to **Fig. 7.5** dimensionless velocity field  $f'(\eta)$  decreases as suction parameter  $s$  increases. Moreover, it is depicted that velocity boundary layer thickness decreases for the first solution with enhancement in suction parameter  $s$ . But for the second solution, growing values of  $s$  decreases the velocity profile near the solid boundary and after the definite distance from the surface they go on increasing again.

### 7.3.3 Thermal Characteristics

In this segment our attention is to focused only on the thermal characteristics of Carreau fluid flow over a shrinking sheet. In order to validate the heat transfer characteristics the effect of few parameters such as magnetic parameter  $M$ , velocity slip parameter  $\delta_1$ , suction parameter  $s$

and Prandtl number  $Pr$  on temperature profile are presented from **Figs. 7.6 – 7.9**. From these **Figs.**, we once again illustrate that the dual nature solution can also be observed in the heat transfer analysis in the range of the same values of shrinking parameter  $\lambda$  and for fixed values of other parameters as expressed previously.

Suction is extremely fundamental marvels to hold the steady flow adjacent the sheet by delaying the separation. The impact of suction parameter is important in investigative and in addition handy perspective. **Fig. 7.6** shows the temperature profile  $\theta(\eta)$  for various estimations of suction parameter  $s$ . From this **Fig.** it is observed that temperature profile  $\theta(\eta)$  diminishes by expanding estimations of  $s$  from 1 to 2 for both the first and second solutions. We further observed that in case of suction  $s = 0.1$ , **Fig. 7.7** represents the dual nature of temperature profile  $\theta(\eta)$  for different values of magnetic parameter  $M$ . For assumed set of fixed values, this **Fig.** characterizes that the temperature distribution  $\theta(\eta)$  is reduced in case of the first solution. However, it should be prominent that an opposite trend of temperature profile  $\theta(\eta)$  is seen in the second solution.

Graphical perspective of **Fig. 7.8** affirms the diminishment in non-dimensional temperature profile  $\theta(\eta)$  inside the boundary layer for higher values of velocity slip parameter  $\delta_1$  for both first and second solutions. The thickness of boundary layer drops off as the magnitude of  $\delta_1$  expanded. However, for first solution of temperature profile has a smaller magnitude in comparison with the second one. **Fig. 7.9** represents the dual nature behavior of non-dimensional thermal relaxation time  $\delta_e$  on the temperature field  $\theta(\eta)$ . Increasing values of  $\delta_e$  reduce the temperature and thermal boundary layer thickness. Physically, it is because of the material particle wants more time for heat transfer to its adjacent particles due to thermal relaxation enrichment.

**Fig. 7.10** is a plot for the dual temperature profile  $\theta(\eta)$  for some definite values of the parameter ( $\lambda > -1$ ) with Prandtl number  $Pr$ . Agreeing to the pattern shown in **Fig. 7.10** one can detect that there is a reduction in the temperature profile  $\theta(\eta)$  as well as the boundary layer thickness. Physically, this is because of the Prandtl number  $Pr$ . Prandtl number has an opposite relation with thermal diffusivity. Increasing values of  $Pr$  correspond to a fragile thermal diffusivity and henceforth temperature reduces.

### 7.3.4 Concentration Characteristics

Our next goal is to present the multiple solutions for the concentration distribution  $\phi(\eta)$  for different values of Schmidt number  $Sc$ . Graphical view of **Fig. 7.11** portrayed the reduction in the first solution of non dimensional concentration profile  $\phi(\eta)$  within the boundary layer for growing values of Schmidt number  $Sc$  while for the second solution, it is noted that the function  $\phi(\eta)$  increases near the sheet and for larger values of  $Sc$  and it appears to be decreasing type after this small region for the rest of the boundary layer flow. Schmidt number  $Sc$  is the ratio of viscous to molecular diffusion rates. Thus higher Schmidt number  $Sc$  gives the low mass diffusivity. It specifies decay in the concentration profile  $\phi(\eta)$ .

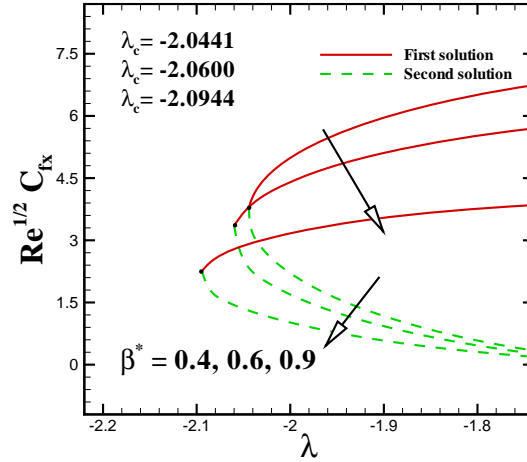


**Fig. 7.2 :** Effect of the viscosity ratio parameter  $\beta^*$  on wall shear stress  $Re^{1/2}C_{fx}$ .



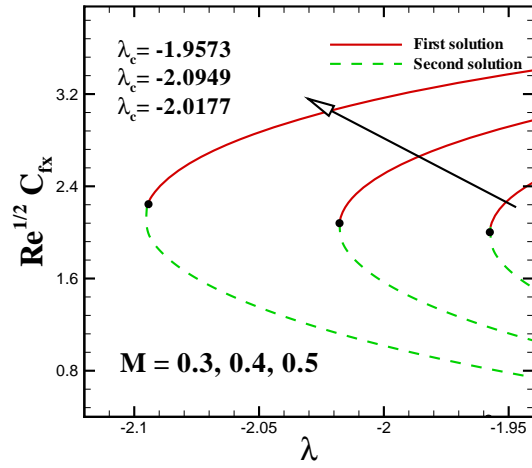


**Fig. 7.3** : Effect of the magnetic parameter  $M$  on the wall shear stress  $Re^{1/2}C_{fx}$ .

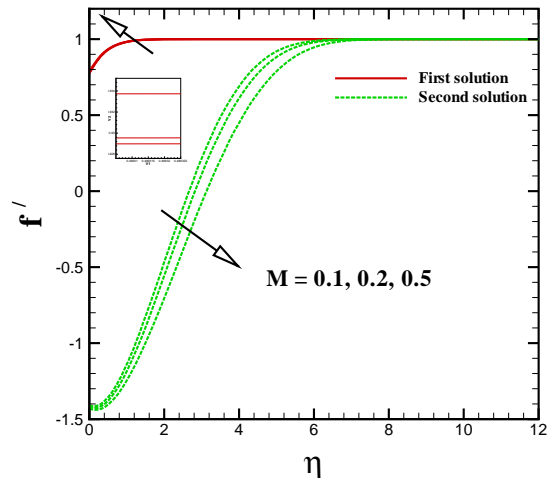


**Fig. 7.4** : Effect of the magnetic parameter  $M$  on velocity profile  $f'(\eta)$ .

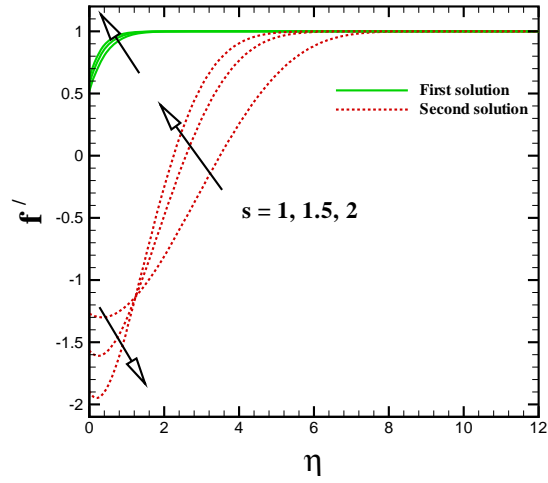


**Fig. 7.5 :** Effect of the suction parameter  $s$  on velocity profile  $f'(\eta)$ .

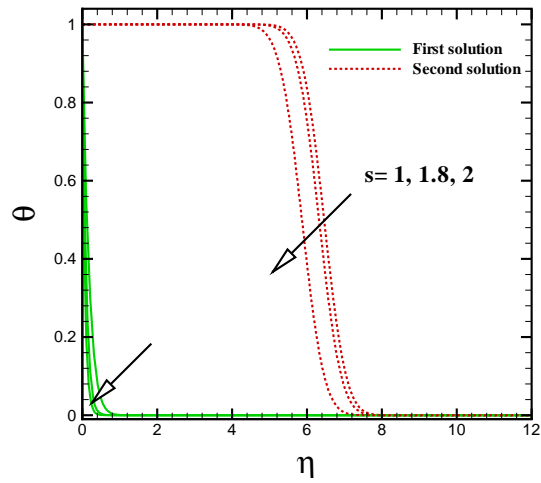


**Fig. 7.6 :** Effect of the suction parameter  $s$  on temperature profile  $\theta(\eta)$ .

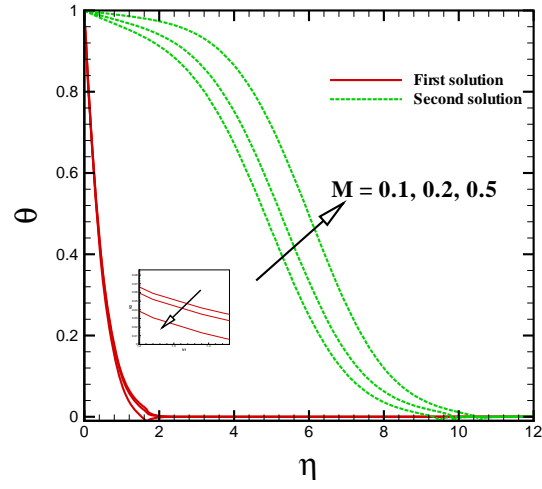


**Fig. 7.7** : Effect of the magnetic parameter  $M$  on temperature profile  $\theta(\eta)$ .

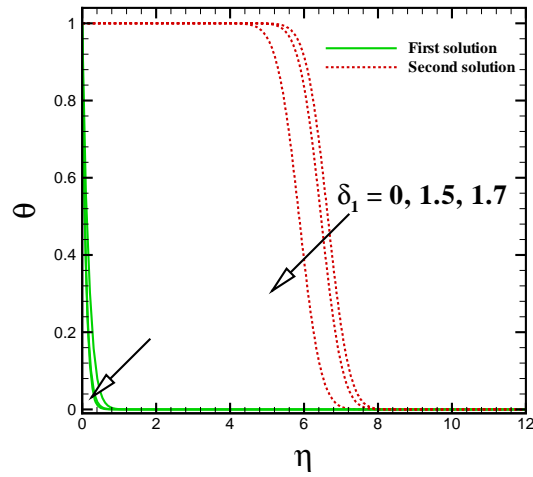


**Fig. 7.8** : Effect of the velocity slip parameter  $\delta_1$  on temperature profile  $\theta(\eta)$ .

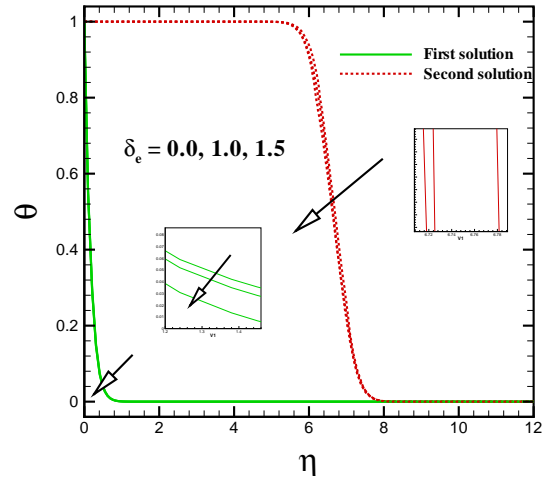


**Fig. 7.9** : Effect of thermal relaxation time  $\delta_e$  on temperature profile  $\theta(\eta)$ .

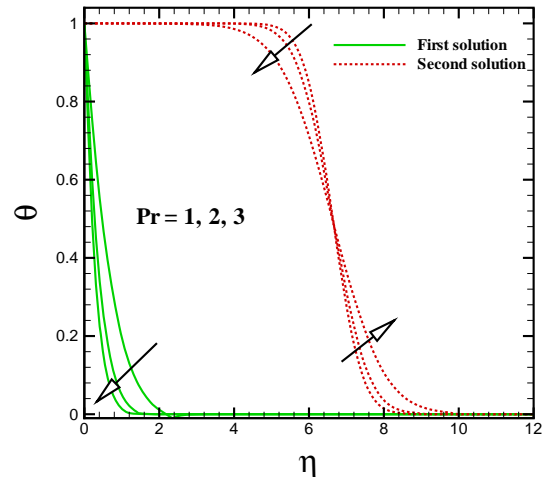


**Fig. 7.10** : Effect of Prandtl number  $Pr$  on temperature profile  $\theta(\eta)$ .

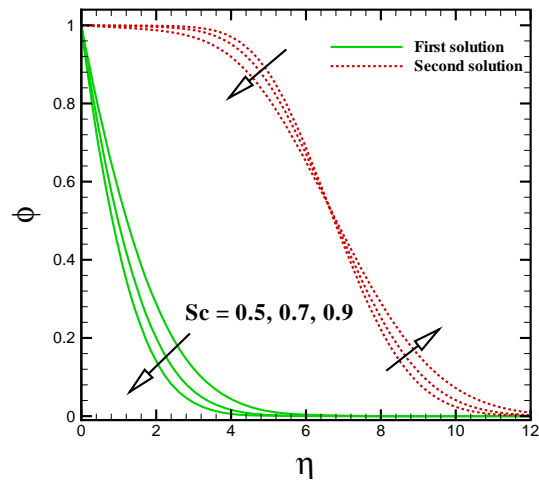


**Fig. 7.11** : Effect of Schmidt number  $Sc$  on concentration profile  $\phi(\eta)$ .

**Table 7.1 :** Values of skin friction coefficient  $f''(0)$  for different values of  $\lambda$ .

$\lambda$	Wang [87]	Yacob and Ishak [88]	Present study
5.0	-10.26475	–	-10.2647543
3.0	–	–	-4.276534
2.0	-1.88731	-1.887307	-1.887270
1.0	0	0	0
0.5	0.7133	0.713295	0.713276
0.0	1.232588	1.232588	1.232553

**Table 7.2 :** A comparison of the skin friction  $Re^{1/2}C_{fx}$  for  $\lambda$  when  $n = 1$ ,  $We = 0$ ,  $\beta^* = 0$ ,  $s = 0$ ,  $M = 0$ ,  $\delta_e = \delta_c = 0$ .

$\lambda$	Wang [87]		Golra and Gireesha [89]		Present study	
	First solution	Second solution	First solution	Second solution	First solution	Second solution
-0.25	1.40224	–	1.40225	–	1.402199	
-0.50	1.4957	–	1.49566	–	1.495626	
-0.75	1.48930	–	1.48928	–	1.489267	
-1.00	1.32882	0	1.32881	0	1.328804	
-1.15	1.08223	0.116702	1.08223	0.11670	1.082230	0.116702
-1.20	–	–	0.93247	0.23363	0.932467	0.233650
-1.2465	0.55430	–	–	–	0.584261	0.554297

## Chapter 8

# Heat Generation/Absorption and Thermal Radiation Impacts on Three Dimensional Flow of Carreau Fluid

The current chapter numerically investigates the three-dimensional flow and heat transport caused by a bidirectional stretching sheet. One phenomenal aspect of this review is to consider the impact of infinite shear rate viscosity. For this reason, Carreau rheological model is accounted as a working liquid for the flow mechanism. In addition, heat transport features of the flow fields have been inspected by utilizing the impacts of magnetic field, thermal radiation and heat generation/absorption. We have incorporated the appropriate dimensionless transformations to alter the basic conservation equations into a set of partially couples ODEs. The associated system of reduced ODEs together with physical boundary restrictions are numerically integrated via versatile and extensively validated, Runge-Kutta Fehlberg method. The problem is governed by active physical parameters such as, viscosity ratio parameter, magnetic parameter, Weissenberg number, nonlinear radiation parameter, heat generation/absorption parameter, Biot number, Prandtl number and temperature ratio parameter. We exhibit and explain the impacts of these active parameters on dimensionless fluid velocity, fluid tempera-

ture, skin friction and Nusselt number by means of tables and graphs. From this study, it is observed that fluid velocity is depressed by higher values of magnetic parameter; however, a reverse trend is noted for fluid temperature.

## 8.1 Geometry of the Physical Model

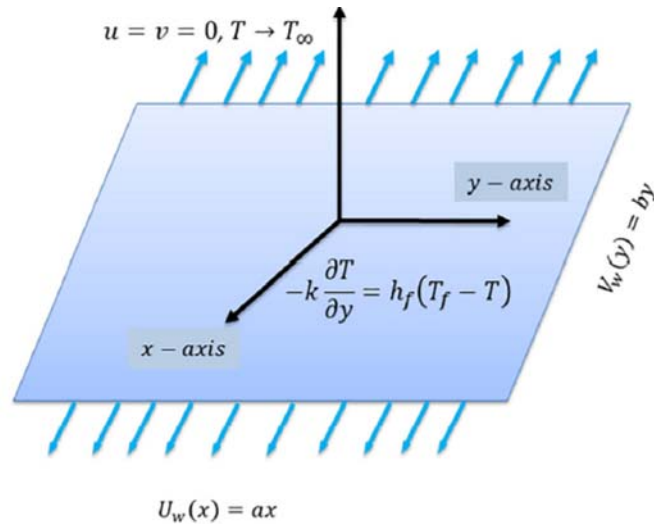


**Fig. 8.1** : The considered physical model and boundary conditions.

## 8.2 Mathematical Formulation

Steady three-dimensional flow of an electrically conducting Carreau fluid caused by a bidirectional stretching surface is considered and described through **Fig. 8.1**. The outcomes of thermal radiation and convective boundary conditions are also exhibited to model the problem. The rectangular coordinates system is selected wherein the flow in direction measures the distance along the surface and direction is normal to it. As the flow is taken to be laminar thus, a uniform magnetic field is applied parallel to the  $z$ -direction.

The mass, momentum and energy conservations can be described by the system of three-dimensional equations in the following form



$$\frac{\partial u}{\partial x} + \frac{\partial v}{\partial y} + \frac{\partial w}{\partial z} = 0, \quad (8.1)$$

$$\begin{aligned} u \frac{\partial u}{\partial x} + v \frac{\partial u}{\partial y} + w \frac{\partial u}{\partial z} = \nu \left( \frac{\partial^2 u}{\partial z^2} \right) \left[ \beta^* + (1 - \beta^*) \left\{ 1 + \Gamma^2 \left( \frac{\partial u}{\partial z} \right)^2 \right\}^{\frac{n-1}{2}} \right] \\ + \nu(n-1)(1-\beta^*)\Gamma^2 \left( \frac{\partial^2 u}{\partial z^2} \right) \left( \frac{\partial u}{\partial z} \right)^2 \left\{ 1 + \Gamma^2 \left( \frac{\partial u}{\partial z} \right)^2 \right\}^{\frac{n-3}{2}} \\ - \frac{\sigma B_0^2}{\rho} u, \end{aligned} \quad (8.2)$$

$$\begin{aligned} u \frac{\partial v}{\partial x} + v \frac{\partial v}{\partial y} + w \frac{\partial v}{\partial z} = \nu \left( \frac{\partial^2 v}{\partial z^2} \right) \left[ \beta^* + (1 - \beta^*) \left\{ 1 + \Gamma^2 \left( \frac{\partial v}{\partial z} \right)^2 \right\}^{\frac{n-1}{2}} \right] \\ + \nu(n-1)(1-\beta^*)\Gamma^2 \left( \frac{\partial^2 v}{\partial z^2} \right) \left( \frac{\partial v}{\partial z} \right)^2 \left\{ 1 + \Gamma^2 \left( \frac{\partial v}{\partial z} \right)^2 \right\}^{\frac{n-3}{2}} \\ - \frac{\sigma B_0^2}{\rho} v, \end{aligned} \quad (8.3)$$

$$u \frac{\partial T}{\partial x} + v \frac{\partial T}{\partial y} + w \frac{\partial T}{\partial z} = \alpha_1 \frac{\partial^2 T}{\partial z^2} - \frac{k}{\rho c_p} \frac{\partial q_r}{\partial z} + \frac{Q}{\rho c_p} (T - T_\infty). \quad (8.4)$$

Radiative heat flux used in Eq. (8.4) which is given by a Rosseland approximation [79] as:

$$q_r = - \left( \frac{4\sigma^*}{3k^*} \frac{\partial T^4}{\partial z} \right), \quad (8.5)$$

For a planer boundary layer flow over a heat surface, Eq. (8.5) can be written as

$$q_r = - \frac{16\sigma^*}{3k^*} \left( T^3 \frac{\partial T}{\partial z} \right), \quad (8.6)$$

in view of Eq. (8.6), energy Eq. (8.4) which can be composed as

$$u \frac{\partial T}{\partial x} + v \frac{\partial T}{\partial y} + w \frac{\partial T}{\partial z} = \frac{\partial}{\partial z} \left[ \left( \alpha_1 + \frac{16\sigma^* T^3}{3k^* \rho c_p} \right) \frac{\partial T}{\partial z} \right] + \frac{Q_0}{\rho c_p} (T - T_\infty). \quad (8.7)$$

The resulting boundary conditions of the present problem are

$$u = U_w(x) = ax, \quad v = V_w(y) = by, \quad w = 0, \quad -k \frac{\partial T}{\partial y} = h_f(T_f - T) \quad \text{at } z = 0, \quad (8.8)$$

$$u \rightarrow 0, \quad v \rightarrow 0, \quad T \rightarrow T_\infty \quad \text{as } z \rightarrow \infty. \quad (8.9)$$

The accompanying dimensionless quantities are used to change the governing PDEs into a scheme of ODEs

$$\begin{aligned} \eta &= z \sqrt{\frac{a}{\nu}}, \quad u = axf'(\eta), \quad v = ayg'(\eta), \\ w &= \sqrt{\frac{a}{\nu}} [f(\eta) + g(\eta)], \quad \theta(\eta) = \frac{T - T_\infty}{T_f - T_\infty}. \end{aligned} \quad (8.10)$$

The momentum and energy equations with the relevant boundary conditions are compacted in the following form

$$\begin{aligned} &\left[ \beta^* + (1 - \beta^*) \left\{ 1 + We_1^2 (f'')^2 \right\}^{\frac{n-3}{2}} \left\{ 1 + nWe_1^2 (f'')^2 \right\} \right] f''' \\ &\quad + (f + g)f'' - (f')^2 - M^2 f' = 0, \end{aligned} \quad (8.11)$$

$$\begin{aligned} &\left[ \beta^* + (1 - \beta^*) \left\{ 1 + We_2^2 (g'')^2 \right\}^{\frac{n-3}{2}} \left\{ 1 + nWe_2^2 (g'')^2 \right\} \right] g''' \\ &\quad + (f + g)g'' - (g')^2 - M^2 g' = 0, \end{aligned} \quad (8.12)$$

$$\theta'' + \text{Pr} (f + g) \theta' + \frac{4}{3N_R} \frac{d}{d\eta} \left[ \{1 + (\theta_w - 1) \theta\}^3 \theta' \right] + \delta \text{Pr} \theta = 0, \quad (8.13)$$

with

$$f(0) = 0, \quad g(0) = 0, \quad f'(0) = 1, \quad g'(0) = \lambda, \quad \theta'(0) = -\gamma [1 - \theta(0)], \quad (8.14)$$

$$f'(\infty) \rightarrow 0, \quad g'(\infty) \rightarrow 0, \quad \theta(\infty) \rightarrow 0, \quad (8.15)$$

with  $We_1 = \sqrt{\frac{a\Gamma^2 U_w^2}{\nu}}$ ,  $We_2 = \sqrt{\frac{a\Gamma^2 V_w^2}{\nu}}$  as the local Weissenberg numbers.

### 8.2.1 Parameters of Engineering Interest

The local skin friction coefficients  $Re^{1/2}C_{fx}$ ,  $Re^{1/2}C_{fy}$  and the local Nusselt number  $Re^{-1/2}Nu_x$  are expressed as

$$C_{fx} = \frac{\tau_{xz}}{\rho U_w^2(x)}, \quad C_{fy} = \frac{\tau_{yz}}{\rho U_w^2(x)}, \quad Nu_x = \frac{x \left[ -k \left( \frac{\partial T}{\partial z} \right)_w + (q_r)_w \right]_{z \rightarrow 0}}{k(T_f - T_\infty)}. \quad (8.16)$$

Upon making use of Eq. (8.16), the dimensionless form of local skin friction coefficient and local Nusselt number are

$$Re_x^{1/2} C_{fx} = f''(0) \left[ \beta^* + (1-\beta^*) \left\{ 1 + We_1^2 \left( f''(0) \right)^2 \right\}^{\frac{n-1}{2}} \right], \quad (8.17)$$

$$\left( \frac{U_w}{V_w} \right) Re_y^{1/2} C_{fy} = g''(0) \left[ \beta^* + (1-\beta^*) \left\{ 1 + We_2^2 \left( g''(0) \right)^2 \right\}^{\frac{n-1}{2}} \right], \quad (8.18)$$

$$Re^{-1/2} Nu_x = -\theta'(0) \left\{ 1 + \frac{4}{3N_R} [1 + (\theta_w - 1)\theta(0)]^3 \right\}, \quad (8.19)$$

where  $Re_x = \frac{xU_w}{\nu}$  and  $Re_y = \frac{yV_w}{\nu}$  are the local Reynolds numbers.

## 8.3 Validation of the Code

To establish the validation of the present numerical code, the comparison tables (**Table 8.1** and **8.2**) are constructed with available published results for various values of velocity ratio parameter  $\lambda$ . We have assumed the limiting case of Newtonian fluid by taking the values  $We_1 = We_2 = M = \beta^* = 0$  and  $n = 1$ . Therefore, the computed results of skin friction coefficients  $-f''(0)$  and  $-g''(0)$  are compared in **Tables 8.1** and **8.2** with those of Areil [90], Hayat *et al.* [91] and Khan *et al.* [92]. A remarkable correspondence is noted between present computations and previous works.

## 8.4 Analysis of the Results

In this section, we aim to discuss the influence of involved physical parameters on the fluid velocities and temperature distributions. This numerical study analyses the impacts of non-dimensional magnetic parameter, velocity ratio parameter, Weissenberg numbers, heat generation/absorption parameter, radiation parameter, temperature ratio parameter and Prandtl number on the flow field and heat transfer characteristics. Further, the computed results of non-dimensional skin frictions and Nusselt number are plotted graphically and explained physically.

First, we will discuss the impacts of viscosity ratio parameter  $\beta^*$  on both the velocity profiles  $f'(\eta)$  and  $g'(\eta)$  by keeping all other parameters fixed. **Fig. 8.2(a)** presents the variation of horizontal velocity profiles  $f'(\eta)$  for different values of  $\beta^*$  in case of shear thinning and shear thickening fluids. It is seen that the fluid velocity increases with higher values of viscosity ratio parameter for shear thinning ( $n < 1$ ) fluid and an inverse is observed in case of shear thickening ( $n > 1$ ) fluid. Moreover, it has been viewed that the associated boundary layer thickness is smaller in case of shear thinning fluid as compare to the shear thickening fluid. The velocity profiles along  $y$ -directions for varying values of viscosity ratio parameter  $\beta^*$  are plotted in **Fig. 8.2(b)**. It is apparent from these plots that a rise in viscosity ratio parameter leads to raise the fluid velocity as well as momentum boundary layer thickness for shear thickening fluid ( $n = 1.7$ ). However, the non-dimensional velocity profiles decrease in case of shear thinning fluid ( $n = 0.7$ ).

The influence of Weissenberg number  $We_1$  on dimensionless velocity components in  $x$  and  $y$  -directions are depicted graphically in **Figs. 8.3(a, b)**. It is interesting to note that these profiles show an opposite behavior for the cases of shear thinning and shear thickening fluids. In **Fig. 8.3(a)**, we found that growing values of Weissenberg number lower the velocity profiles  $f'(\eta)$  in case of ( $n = 0.7$ ) while it enhances the velocity in case of ( $n = 1.7$ ). From these sketches we notice that the thickness of momentum boundary layer reduces for shear thinning case and grows for shear thickening case with higher Weissenberg number. In all the cases, the far field boundary conditions are fulfilled asymptotically at  $\eta = 4$ . The computation results of velocity distributions  $f'(\eta)$  and  $g'(\eta)$  with varying values of magnetic parameter  $M$  for two different values of power-law index are illustrated in **Figs. 8.4(a, b)**. As expected, the fluid velocity

decreases in both the cases with an increase in magnetic parameter. This means that the applied magnetic field has retarding effect on the velocity distributions for both shear thinning and shear thickening cases. This is in conformity with the fact that the presence of magnetic parameter generates a force called Lorentz force which resist the fluid motion. Consequently, the momentum boundary layer thickness reduces for higher values of  $M$ . However, the fluid velocities as well as the associated boundary layer thicknesses in the case of shear thickening fluid are greater than those of shear thinning fluid.

In **Figs. 8.5(a, b)** the evolution of temperature distributions with variation in heat generation/absorption parameter  $\delta$  and Biot number  $\gamma$  are described. In these figures, the temperature curves are sketched for two different cases of power-law index  $n$  i.e., ( $n < 1$ ) and ( $n > 1$ ). From **Fig. 8.5(a)**, it can clearly be viewed that at any point inside the boundary layer, the temperature profiles  $\theta(\eta)$  increases whenever the heat generation/absorption parameter gets the larger values. It is apparent that fluid temperature is higher in case of shear thinning fluid. Also, we see that the thermal boundary layer thickness represents a significant growth with an increment in heat generation/absorption parameter. The impact of Biot number on dimensionless temperature profiles is illustrated in **Fig. 8.5(b)**. It is sighted that there is a strong impact of Biot number on temperature profiles in case of both shear thinning and thickening fluid. It is clearly shown that the simulated result of non-dimensional temperature demonstrates an accelerating conduct with rising values of Biot number  $\gamma$ . Physically, Biot number is associated with heat transfer at the surface and an increase in  $\gamma$  causes an enhancement in thermal boundary layer which produces a significant rise in temperature profiles.

Consequences of magnetic parameter  $M$  on temperature distribution are elucidated through **Fig. 8.6(a)**. It is demonstrated through this figure that for both the cases of shear thinning and shear thickening fluids, a reasonable rise in fluid temperature is noted for higher magnetic parameter. At all points with in the boundary layer, the fluid temperature takes higher values for shear thinning fluid. In addition, it may be noted that the corresponding thermal boundary layer thickness increases with growing  $M$ . The obtained curves of non-dimensional fluid temperature for various values of thermal radiation parameter  $N_R$  are exposed in **Fig. 8.6(b)**. It is depicted from this figure that temperature profiles increase with increase in radiation parameter for both the fluids. However, larger temperature is seen to occur for higher values of  $N_R$

in case of shear thinning fluid. Further, the thermal boundary layer thickness argument with larger values of  $N_R$ . **Fig. 8.7(a)** demonstrates the temperature distribution for a variation of temperature ratio parameter  $\theta_w$ . As expected, the temperature curves start with a greater value and show a significant drop in temperature values as they progress with in the boundary layer. We notice that  $\eta = 5$  is sufficient for all the curves to satisfy the far field boundary condition. In an examination of this figure, it is observed that the dimensionless temperature inside the boundary layer increase substantially with an increase in the temperature ratio parameter. Physically, this is due to fact that the temperature ratio parameter transmits to higher wall temperature as associated to ambient fluid and as a result temperature of the fluid rises. Moreover, thermal boundary layer thickness enhances for augmented values of  $\theta_w$ . The calculated results of non-dimensional temperature distributions for several values of Weissenberg number  $We_1$  are delineated through **Fig. 8.7(b)**. These results are computed for both shear thinning and shear thickening fluids by keeping the other parameter fixed. We found that for a fixed nonzero value of  $\eta$ , there is tendency of growing values of  $We_1$  cause for decreasing the fluid temperature for shear thickening fluid. However, an inverse behavior is noted in shear thinning fluid. That is, temperature profiles rise with the escalating values of Weissenberg number.

**Tables 8.3** and **8.4** illustrates how the skin friction coefficients  $Re_x^{1/2}C_{fx}$ ,  $\left(\frac{U_w}{V_w}\right) Re_y^{1/2}C_{fy}$  and Nusselt number  $Re^{-1/2}Nu_x$  varies with different values of magnetic parameter  $M$ , Weissenberg numbers  $We_1$  and  $We_2$ , velocity ratio parameter  $\lambda$  and viscosity ratio parameter  $\beta^*$ . It is found that the magnitude of skin friction in  $x$ -direction  $\left(|Re_x^{1/2}C_{fx}|\right)$  is significantly raise by  $M$  and  $\lambda$  for both shear thinning and shear thickening fluids. In addition, it may be prominent from the table that  $Re_x^{1/2}C_{fx}$  (absolute value) augments with the increase of  $We_1$  and  $We_2$  for shear thickening fluid and a quite opposite is true for shear thinning fluid. Similarly, the absolute value of skin friction in  $y$ -direction  $\left(\frac{U_w}{V_w}\right) Re_y^{1/2}C_{fy}$  is reduced by increasing the values of  $We_1$  and  $We_2$  in case of shear thinning fluid and it enhances in case of shear thickening fluid. In **Table 8.4**, an increasing behavior of Nusselt number is detected for Prandtl number, temperature ratio parameter, radiation parameter, Biot number and viscosity ratio parameter in case of both shear thinning and shear thickening fluids.

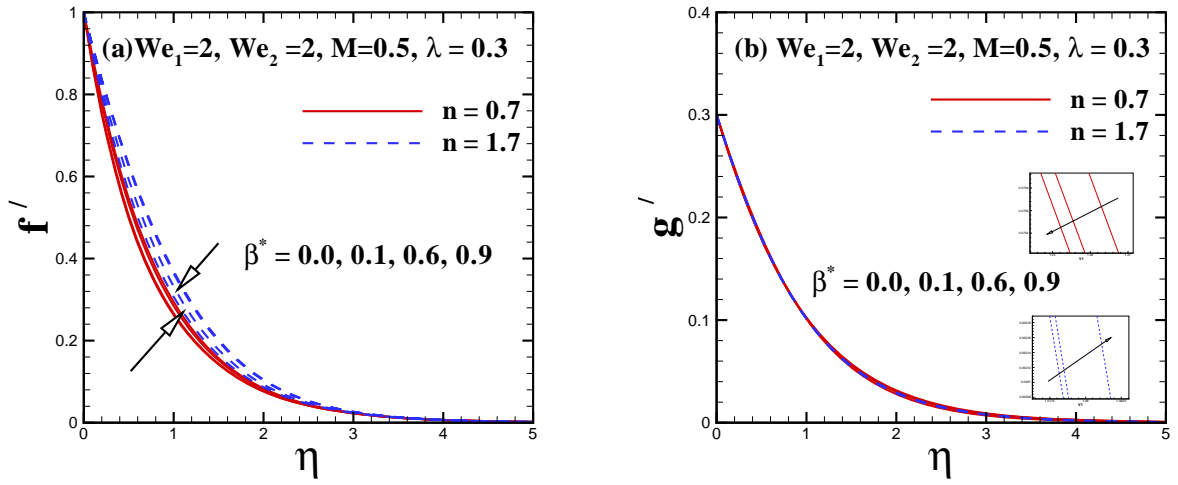


Fig. 8.2: Impact of viscosity ratio parameter  $\beta^*$  on the velocity distribution.

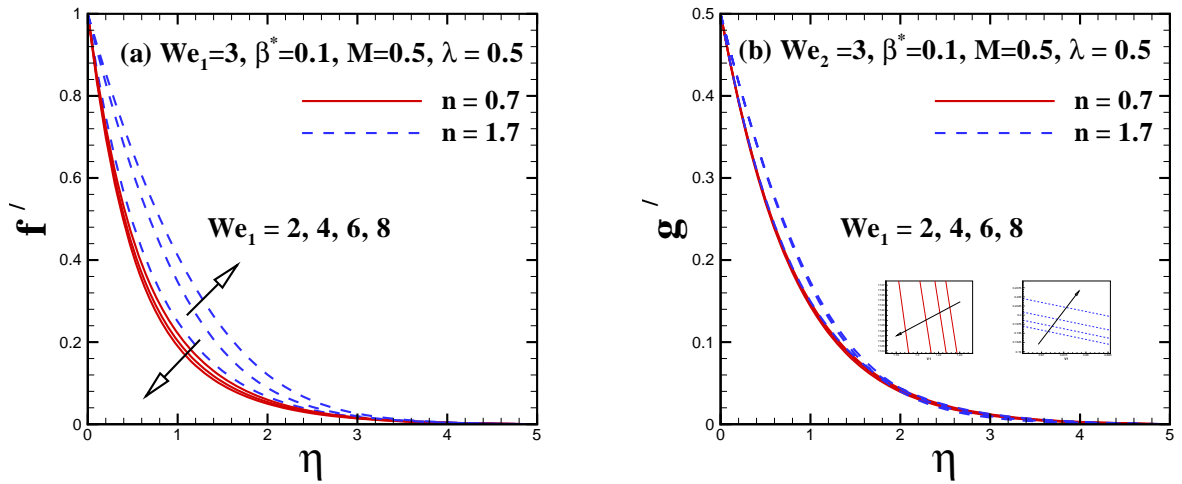


Fig. 8.3: Impact of Weissenberg number  $We_1$  on the velocity distribution.

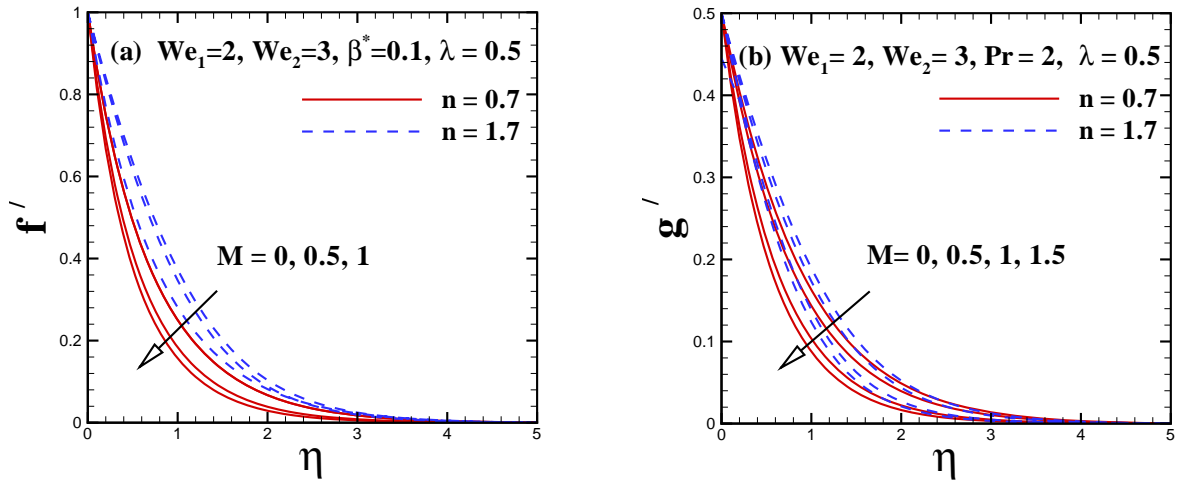


Fig. 8.4: Impact of the magnetic parameter  $M$  on the velocity distribution.

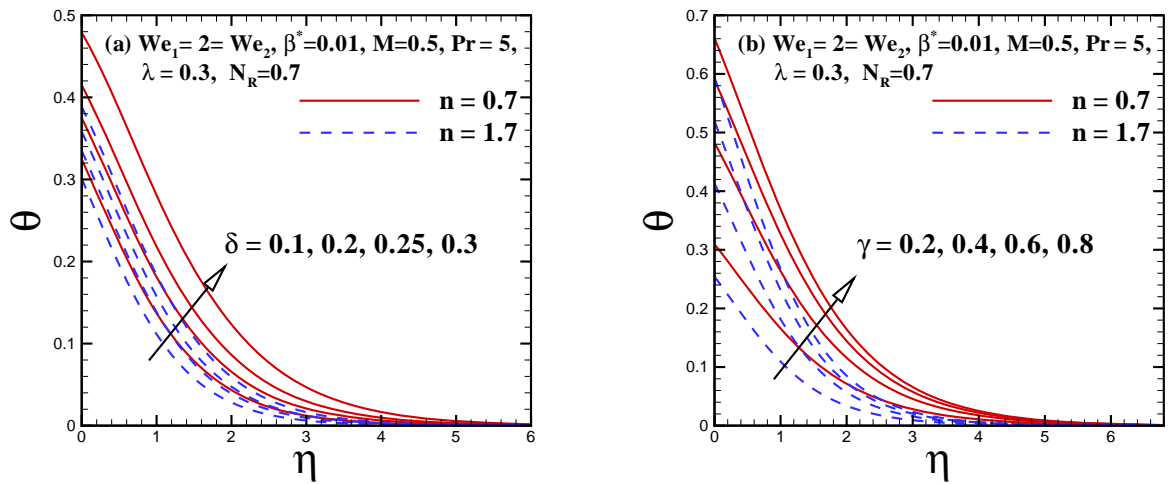
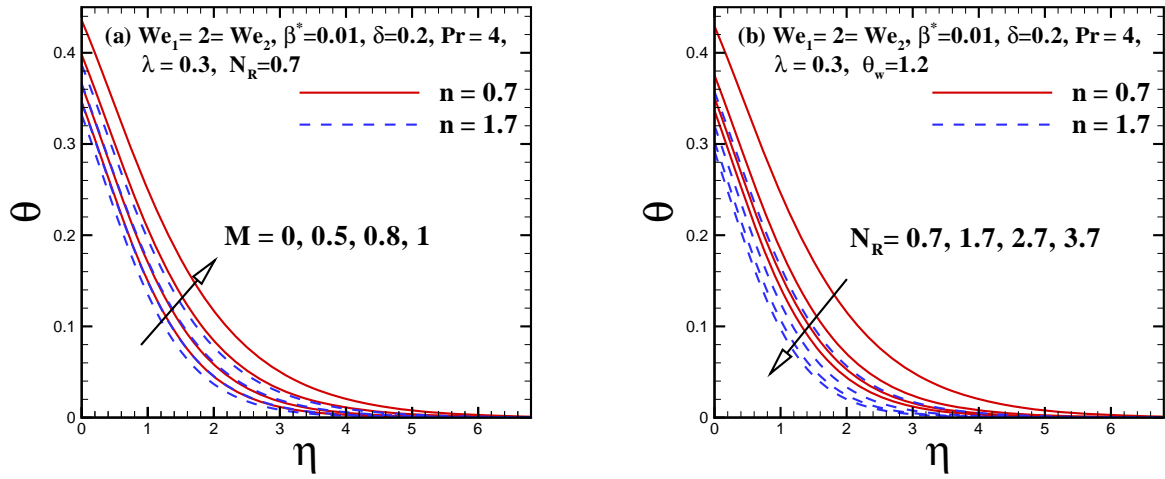
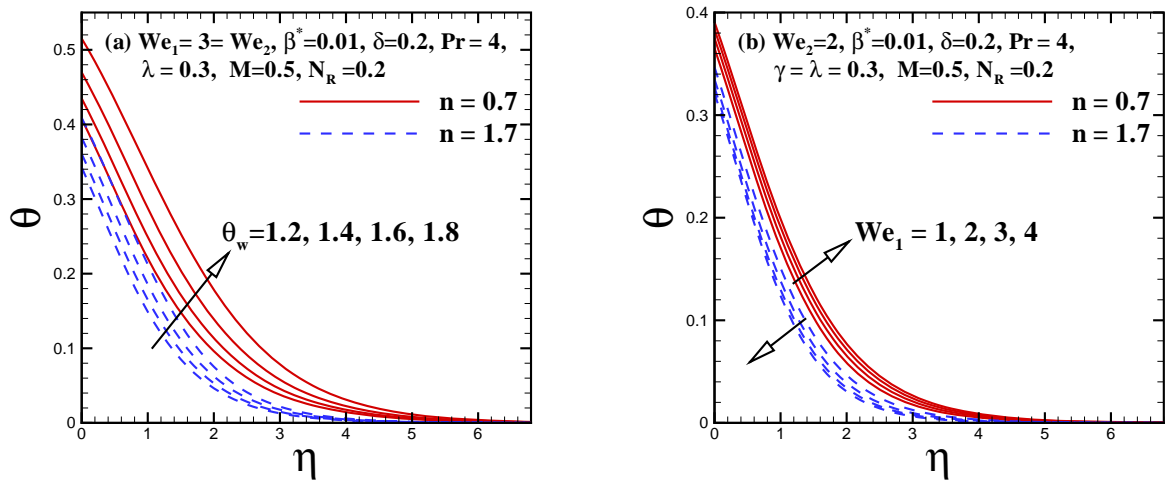


Fig. 8.5: Impact of heat generation/absorption parameter  $\delta$  and Biot number  $\gamma$  on the temperature distribution.





**Fig. 8.6:** Impact of the magnetic parameter  $M$  and radiation parameter  $N_R$  on the temperature distribution.



**Fig. 8.7:** Impact of the temperature ratio parameter  $\theta_w$  and Weissenberg number  $We_1$  on the temperature distribution.

**Table 8.1:** Comparison of skin friction coefficient  $f''(0)$  for different values of  $\lambda$ .

$\lambda$	Ariel (HPM)[90]	Ariel (Exact)[90]	Hayat et al.[91]	Khan et al. [92]	Present study
0	1	1	1	1	1
0.1	1.017027	1.020264	1.020260	1.020264	1.021368
0.2	1.034587	1.039497	1.039495	1.039497	1.040403
0.3	1.057470	1.057956	1.057955	1.057956	1.058713
0.4	1.070529	1.075788	1.075788	1.075788	1.076429
0.5	1.088662	1.093095	1.093095	1.093095	1.093641
0.6	1.106797	1.109946	1.109947	1.109946	1.110416
0.7	1.124882	1.126397	1.126398	1.126397	1.126803
0.8	1.142879	1.142488	1.142489	1.142488	1.142840
0.9	1.160762	1.158253	1.158254	1.158253	1.158560
1.0	1.178511	1.17372	1.173721	1.173720	1.173988

**Table 8.2:** Comparison of skin friction coefficient  $-g''(0)$  for different values of  $\lambda$ .

$\lambda$	Ariel (HPM)[92]	Ariel (Exact) [92]	Hayat <i>et al.</i> [93]	Khan et al. [94]	Present study
0	0	0	0	0	0
0.1	0.070399	0.066847	0.066847	0.0668485	0.067168
0.2	0.158231	0.148737	0.148737	0.1487382	0.149165
0.3	0.254347	0.243360	0.243359	0.2433607	0.243812
0.4	0.360599	0.349209	0.349209	0.3492087	0.349651
0.5	0.476290	0.465205	0.465205	0.4652046	0.465622
0.6	0.600833	0.590529	0.590529	0.5905229	0.590916
0.7	0.733730	0.724532	0.724532	0.7245312	0.724887
0.8	0.874551	0.866683	0.866683	0.8666822	0.867007
0.9	1.022922	1.016539	1.016540	1.016538	1.016833
1.0	1.178511	1.173721	1.173722	1.173720	1.173988

**Table 8.3** : Simulated results of skin friction coefficient for different values of  $\beta^*$ ,  $M$ ,  $We$  and  $\lambda$  when  $Pr = 1.5$ ,  $\gamma = 0.3$ ,  $\theta_w = 1.5$  and  $N_R = 1$ .

$M$	$We_1$	$We_2$	$\lambda$	$\beta^*$	$Re_x^{1/2} C_{fx}$		$\left(\frac{U_w}{V_w}\right) Re_y^{1/2} C_{fy}$	
					$n = 0.7$	$n = 1.7$	$n = 0.7$	$n = 1.7$
0	2.0	3.0	0.3	0.1	-0.96576	-1.23795	-0.235881	-0.260041
0.5					-1.05705	-1.38301	-0.275319	-0.304764
1.0					-1.28613	-1.77192	-0.368224	-0.417119
0.5	3.0				-1.00816	-1.48675	-0.27389	-0.307439
	4.0				-0.971859	-1.57466	-0.272806	-0.309481
	5.0				-0.943704	-1.65085	-0.271948	-0.311099
	2.0	4.0			-1.05673	-1.38407	-0.271584	-0.312067
		5.0			-1.05641	-1.38509	-0.267719	-0.319361
		6.0			-1.05609	-1.38604	-0.263946	-0.326424
		3.0	0.5		-1.08077	-1.43047	-0.491202	-0.596501
			0.8		-1.11272	-1.50366	-0.838253	-1.177371
			1.0		-1.13227	-1.55324	-1.082581	-1.659611
			0.3	0.2	-1.07179	-1.36512	-0.276514	-0.302914
				0.6	-1.12406	-1.2825	-0.280966	-0.294813
				0.9	-1.15806	-1.2019	-0.284034	-0.287698

**Table 8.4** : Simulated results of Nusselt number for different values of  $\beta^*$ ,  $Pr$ ,  $\theta_w$ ,  $N_R$  and  $\gamma$  when  $M = 0.3$ ,  $We_1 = 2$ ,  $We_2 = 3$  and  $\lambda = 0.3$ .

Pr	$\theta_w$	$N_R$	$\gamma$	$\beta^*$	$Re^{-1/2}Nu_x$	
					$n = 0.7$	$n = 1.7$
2.0	1.5	0.7	0.3	0.1	0.212502	0.214189
	4.0				0.225145	0.227655
	6.0				0.234926	0.237297
	8.0				0.241992	0.244088
2.0	1.4				0.205926	0.208535
	1.6				0.222134	0.222603
	1.9				0.276641	0.271983
	2				0.305472	0.299078
		1.7			0.257005	0.254897
		2.7			0.278454	0.274306
		3.7			0.294968	0.289157
		0.7	0.6		0.390918	0.396423
			0.9		0.523059	0.537322
			1.2		0.615242	0.638114
				0.4	0.212726	0.213903
				0.6	0.212859	0.213679
				0.8	0.212982	0.213417

## Chapter 9

# Local Non-similar Solutions of Convective Flow of Carreau Fluid

In this chapter we study a realistic methodology to inspect the non-similar solutions for the two-dimensional steady Carreau fluid flow in the presence of applied magnetic field and mixed convection within the sight of infinite shear rate viscosity. With the help of local non-similar method, we presented the non-linear PDEs for the flow and heat transfer analysis. The leading PDEs are converted into non-linear ODEs by using the local non-similarity method (LNM). The final resulting non-dimensional set of coupled non-linear ODEs are then solved with the help of `bvp4c` function in MATLAB. This investigation covers numerous physical aspects of flow and heat transfer. Major outcomes in the form of velocity enhancement and temperature reduction for the higher values of buoyancy parameter ( $\xi$ ) are observed. On the other hand, for increasing values of thermal radiation parameter  $N_R$  the temperature of the fluid increases while for larger values of suction/injection parameter the temperature of the fluid reduces. Parallel variation of buoyancy parameter and Weissenberg number show a slight difference regarding local similar and local non-similar solution while computing the local skin friction number. The enhancement in buoyancy parameter causes enhancement in local skin friction as well as local Nusselt number. Additionally, this investigation is validated through a comparison with previous results.

## 9.1 Problem Statement

The impact of magnetic field in stagnation point flow of a Carreau fluid with heat transfer analysis is considered. The fluid flow in this case is due to a mixed convection and porosity of the plate. Here Cartesian coordinates system is utilized. Since  $x$ -axis is a coordinate dignified the horizontal axis and  $y$ -axis is along the normal to the porous plate. We assume that the fluid moves with constant velocity  $U_0$ . Moreover, a uniform magnetic field of strength  $B_0$  is applied normal to the plate and the induced magnetic field is neglected under low magnetic Reynolds number assumption. Furthermore, heat transfer analysis is completed along the thermal radiation effects.

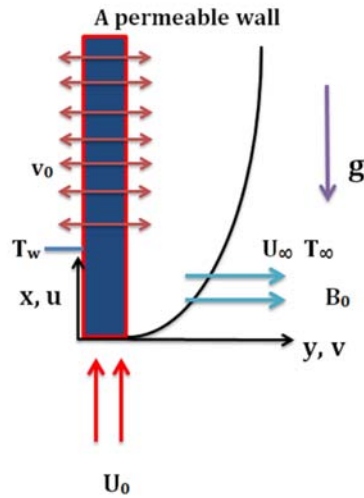


**Figure 9.1:** Physical configuration and coordinate system.

Using the Carreau fluid model proposed by Carreau [1] in 1975, the governing equation describing the conservation of mass, momentum and energy are given by

$$\frac{\partial u}{\partial x} + \frac{\partial v}{\partial y} = 0, \quad (9.1)$$

$$\begin{aligned}
u \frac{\partial u}{\partial x} + v \frac{\partial u}{\partial y} &= U_\infty \frac{dU_\infty}{dx} + \nu \left( \frac{\partial^2 u}{\partial y^2} \right) \left[ \beta^* + (1 - \beta^*) \left\{ 1 + \Gamma^2 \left( \frac{\partial u}{\partial y} \right)^2 \right\}^{\frac{n-1}{2}} \right] \\
&+ \nu(n-1)(1-\beta^*)\Gamma^2 \left( \frac{\partial^2 u}{\partial y^2} \right) \left( \frac{\partial u}{\partial y} \right)^2 \left\{ 1 + \Gamma^2 \left( \frac{\partial u}{\partial y} \right)^2 \right\}^{\frac{n-3}{2}} \\
&+ \frac{\sigma B_0^2}{\rho} (U_\infty - u) + \beta g(T - T_\infty), \tag{9.2}
\end{aligned}$$

$$u \frac{\partial T}{\partial x} + v \frac{\partial T}{\partial y} = \alpha_1 \frac{\partial^2 T}{\partial y^2} - \frac{1}{\rho c_p} \frac{\partial q_r}{\partial y}, \tag{9.3}$$

along with the corresponding BCs defined as follows

$$u = 0, \quad v = -v_0 \text{ (constant)}, \quad T = T_w \quad \text{at} \quad y = 0, \tag{9.4}$$

$$u \rightarrow U_\infty, \quad T \rightarrow T_\infty \quad \text{as} \quad y \rightarrow \infty. \tag{9.5}$$

With a specific end goal to improve our calculation and analysis, we follow the following dimensionless transformations

$$\Psi(x, \eta) = \sqrt{\nu x U_0} f(x, \eta), \quad \theta(x, \eta) = \frac{T - T_\infty}{T_w - T_\infty}, \quad \eta = y \sqrt{\frac{U_0}{\nu x}}. \tag{9.6}$$

Equation (9.1) is indistinguishably satisfied by means of stream function  $\Psi(x, y)$  such that

$$u = \frac{\partial \Psi}{\partial y}, \quad v = -\frac{\partial \Psi}{\partial x}, \quad \xi = \frac{Gr_x}{Re_x^2}. \tag{9.7}$$

The velocity components are then defined as

$$u = U_0 f'(\eta), \quad v = -\sqrt{\frac{U_0 \nu}{x}} \left( \frac{1}{2} f + x \frac{\partial f}{\partial x} + x \frac{\partial f}{\partial \eta} \frac{\partial \eta}{\partial x} \right). \tag{9.8}$$

Radiative heat flux utilized in Eq. (9.3) is specified by the Roseland approximation [80]

To convert Eqs. (9.2 – 9.3) into ordinary differential equations, we utilized Eqs. (9.6 – 9.8).

Thus, we obtain the following system of equations:



$$\begin{aligned} & \left[ \beta^* + (1 - \beta^*) \left\{ 1 + We^2(f'')^2 \right\}^{\frac{n-3}{2}} \left\{ 1 + nWe^2(f'')^2 \right\} \right] f''' + \frac{1}{2}ff'' + \xi\theta - M(f' - 1) \\ & = \xi \left( \frac{\partial f}{\partial \eta} \frac{\partial f'}{\partial \xi} - \frac{\partial f}{\partial \xi} \frac{\partial^2 f}{\partial \eta^2} \right), \end{aligned} \quad (9.9)$$

$$\frac{1}{Pr} \left( 1 + \frac{4}{3N_R} \right) \theta'' + \frac{1}{2}f\theta' = \xi \left( \frac{\partial f}{\partial \eta} \frac{\partial \theta}{\partial \xi} - \frac{\partial \theta}{\partial \eta} \frac{\partial f}{\partial \xi} \right), \quad (9.10)$$

with related boundary conditions

$$f'(\xi, 0) = 0, \quad f(\xi, 0) = 2s - 2\xi \frac{\partial f}{\partial \xi}, \quad \theta(\xi, 0) = 1 \quad \text{at} \quad \eta = 0, \quad (9.11)$$

$$f'(\xi, \infty) = 1, \quad \theta(\xi, \infty) = 0 \quad \text{as} \quad \eta = \infty. \quad (9.12)$$

The additional parameters are expressed

$$\begin{aligned} \xi &= \frac{Gr_x}{Re_x^2}, \quad Gr_x = \frac{g\beta(T_w - T_\infty)x^3}{v}, \quad Re_x = \frac{U_0x}{v} \\ We &= \left( \frac{\Gamma^2 U_0^2}{vx} \right)^{1/2}, \quad M = \frac{\sigma B_0^2 x}{\rho U_0} \\ N_R &= \frac{kk^*}{4\sigma^* T_\infty^3}, \quad s = \frac{v_0 x}{(vUx)^{1/2}}. \end{aligned} \quad (9.13)$$

where  $\xi$  is known as a stream wise coordinate. For  $\xi > 0$  means assisting the flow and  $\xi < 0$  means buoyancy opposite force of the flow. It is observed that after transformation, Eqs. (9.9) to (9.10) still contain  $\frac{\partial}{\partial \xi}$  term and its clear that this issue is non-similar boundary layer issue and may be comprehended utilizing local non-similarity method.

## 9.2 Local Non-similar Solution Method

One, most of the time utilized idea in the arrangement of non-similar boundary layers is the rule of local similarity. As indicated by this perception, the right-hand sides of Eqs. (9.9) and

(9.10) are expected to be necessarily small so it might approaches to zero, coming about an arrangement of ordinary differential equations is simplified. Therefore, first level of truncation or the local similarity solution is attractive for calculation but indicates the numerical outcomes of unclear accuracy. This is because of doubt on whether to disregard the right-hand side of the conditions or not when  $\xi$  is not small. To overwhelmed such a problem Sparrow and Yu [93] proposed the local non-similarity method to find the solution of the non-similar boundary layer equations. To get the local non-similar arrangement of Eqs. (9.9) to (9.12), first we remove the term  $\partial/\partial\xi$  by describing the new dependent variables.

Let the new dependent variable are

$$g = \frac{\partial f}{\partial \xi}, \quad \varphi = \frac{\partial \theta}{\partial \xi}, \quad z = \frac{\partial g}{\partial \xi} \quad \text{and} \quad \chi = \frac{\partial \varphi}{\partial \xi}. \quad (9.14)$$

After substituting the above variables, Eqs. (9.9) to (9.12), become

$$\left[ \beta^* + (1 - \beta^*) \left\{ 1 + We^2(f'')^2 \right\}^{\frac{n-3}{2}} \left\{ 1 + nWe^2(f'')^2 \right\} \right] f''' + \frac{1}{2} f f'' + \xi \theta - M (f' - 1) = \xi (f' g' - g f''), \quad (9.15)$$

$$\frac{1}{Pr} \left( 1 + \frac{4}{3N_R} \right) \theta'' + \frac{1}{2} f \theta' = \xi (\phi f' - g \theta') \quad (9.16)$$

and the boundary conditions are

$$f'(\xi, 0) = 0, f(\xi, 0) = 2s - 2\xi g(\xi, 0), \theta(\xi, 0) = 1, \quad (9.17)$$

$$f'(\xi, \infty) = 1, \theta(\xi, \infty) = 0. \quad (9.18)$$

Since  $g$  and  $\varphi$  are two extra unknown functions, it is necessary to find two more equations to find  $g$  and  $\varphi$ . Secondary equation for  $g$  and  $\varphi$  with their BCs are resulting by taking the derivative of the above Eqs. (9.15) to (9.16) with respect to  $\xi$  and this leads to

$$\begin{aligned}
& \left[ \beta^* + (1 - \beta^*) \left\{ 1 + We^2(f'')^2 \right\}^{\frac{n-3}{2}} \left\{ 1 + nWe^2(f'')^2 \right\} \right] g''' \\
& + f''' \frac{1}{2} (1 - \beta^*) (n - 1) \left\{ 1 + We^2(f'')^2 \right\}^{\frac{n-5}{2}} We^2 f'' g'' \left\{ 3 + nWe^2(f'')^2 \right\} \\
& \quad \left\{ 2We^2 f'' g'' + (f'')^2 \frac{\partial}{\partial \xi} (We^2) \right\} \\
& + \frac{1}{2} g f'' + \frac{1}{2} f g'' - M(g') + \theta + \xi \phi = \xi (g' g' - g g'') + (f' g' - g f''), \quad (9.19)
\end{aligned}$$

$$\frac{1}{Pr} \left( 1 + \frac{4}{3N_R} \right) \phi'' + \frac{1}{2} g \theta' + \frac{1}{2} f \phi' = f' \phi - \theta' g + \xi (g' \phi - g \phi'), \quad (9.20)$$

with the associated boundary conditions

$$g'(\xi, 0) = 0, g(\xi, 0) + 2\xi z(\xi, 0) = 0, \varphi(\xi, 0) = 0, g'(\xi, \infty) = 0. \quad (9.21)$$

Eqs. (9.20) to (9.22) serve as auxiliaries to the governing equations (9.15) to (9.18). It would be noticed that, this type of local non-similarity solution is also recognized as second level of truncation or referred as two equations non-similarity method [94]. To transmit this method to the third level of truncation (or three equations model) in a same way, we again take the derivative of the auxiliary equations (9.20) to (9.22) with respect to  $\xi$ , while the representing equations and their boundary conditions are obtained with approximation [95]. This provides the following equations and boundary conditions

$$\begin{aligned}
& \left[ \beta^* + (1 - \beta^*) \left\{ 1 + We^2(f'')^2 \right\}^{\frac{n-3}{2}} \left\{ 1 + nWe^2(f'')^2 \right\} \right] z''' \\
& + g'''(1 - \beta^*) \left( \frac{n-3}{2} \right) \left\{ 1 + We^2(f'')^2 \right\}^{\frac{n-5}{2}} \left\{ 1 + nWe^2(f'')^2 \right\} \left\{ 2We^2 f'' g'' + (f'')^2 \frac{\partial}{\partial \xi}(We^2) \right\} \\
& \quad + g'''(1 - \beta^*) \left\{ 1 + We^2(f'')^2 \right\}^{\frac{n-3}{2}} \left\{ n(f'')^2 \frac{\partial}{\partial \xi}(We^2) + 2nWe^2 f'' g'' \right\} \\
& + g'''(1 - \beta^*) \left( \frac{n-3}{2} \right) \left\{ 1 + We^2(f'')^2 \right\}^{\frac{n-5}{2}} \left\{ 1 + nWe^2(f'')^2 \right\} \left\{ 2We^2 f'' g'' + (f'')^2 \frac{\partial}{\partial \xi}(We^2) \right\} \\
& \quad + f'''(1 - \beta^*) \left( \frac{n-3}{2} \right) \left( \frac{n-5}{2} \right) \left\{ 1 + We^2(f'')^2 \right\}^{\frac{n-7}{2}} \left\{ 2We^2 f'' g'' + (f'')^2 \frac{\partial}{\partial \xi}(We^2) \right\}^2 \\
& \quad \quad \quad \left\{ 1 + nWe^2(f'')^2 \right\} \\
& \quad + f'''(1 - \beta^*) \left( \frac{n-3}{2} \right) \left\{ 1 + We^2(f'')^2 \right\}^{\frac{n-5}{2}} n \left\{ 2We^2 f'' g'' + (f'')^2 \frac{\partial}{\partial \xi}(We^2) \right\}^2 \\
& \quad + g'''(1 - \beta^*) \left\{ 1 + We^2(f'')^2 \right\}^{\frac{n-3}{2}} n \left\{ 2We^2 f'' g'' + (f'')^2 \frac{\partial}{\partial \xi}(We^2) \right\} \\
& \quad + f'''(1 - \beta^*) \left( \frac{n-3}{2} \right) \left\{ 1 + We^2(f'')^2 \right\}^{\frac{n-5}{2}} n \left\{ 2We^2 f'' g'' + (f'')^2 \frac{\partial}{\partial \xi}(We^2) \right\} \\
& \quad + f'''(1 - \beta^*) \left\{ 1 + We^2(f'')^2 \right\}^{\frac{n-3}{2}} (2n f'' g'' \frac{\partial}{\partial \xi}(We^2) + 2n We^2 g'' g'' + 2n We^2 f'' z'' \\
& + 2n f'' g'' \frac{\partial}{\partial \xi}(We^2) + n f''^2 \frac{\partial^2}{\partial \xi^2}(We^2)) + \frac{1}{2} z f'' + \frac{1}{2} g g'' + \frac{1}{2} g g'' + \frac{1}{2} f z'' - M z' + 2\phi + \xi \chi \\
& = f' z' + g'^2 - g'' g - f'' z + \xi [2g' z' - g'' z - z'' g], \tag{9.22}
\end{aligned}$$

$$\begin{aligned}
& \frac{1}{\text{Pr}} \left( 1 + \frac{4}{3N_R} \right) \chi'' + \frac{1}{2} (z\theta' + 2g\phi' + f\chi') = 2g'\phi - 2\phi'g \\
& \quad + f'\chi - \theta'z + \xi (\phi z' + g'\chi - z\phi' - g\chi'), \tag{9.23}
\end{aligned}$$

$$z'(\xi, 0) = 0, \quad 5z(\xi, 0) + 2\xi \frac{\partial z}{\partial \xi}(\xi, 0) = 0, \quad \chi(\xi, 0) = 0, \quad z'(\xi, \infty) = 0, \quad \chi(\xi, \infty) = 0. \tag{9.24}$$

With a specific end goal to formulate the three-equations model, first we neglect term  $\xi \frac{\partial g}{\partial \xi}$

and  $\xi \frac{\partial \phi}{\partial \xi}$  in the second level of truncation while,  $\xi \frac{\partial z}{\partial \xi}$  and  $\xi \frac{\partial \chi}{\partial \xi}$  are neglected in the third level of truncation. The method of reasoning for this diminishment is like the idea in determining the local similarity model; however, with an essential difference in the results. In local similarity model, it is proposed that derivatives including  $\partial/\partial \xi$  are small when  $\xi$  is not small. Correspondingly, in diminishing Eqs. (9.15) to (9.16), it was hypothesized that the differentiation of the auxiliary functions  $[\frac{\partial z}{\partial \xi}$  and  $\frac{\partial \chi}{\partial \xi}]$  are adequately small for  $\xi$  values not almost zero with the goal that they might be dismissed [93]. On account of local similarity method, the result is that a piece of the momentum and energy equations itself is lost, yet for the local non-similarity method, the decline is presented in auxiliary equations (Eqs. (9.15) to (9.16)), so that the non-similarity terms in the auxiliary equations are reserved. As a consequence, the local non-similarity methodology would produce more precise outcomes contrasted with the local similarity method [94]. Hence, the governing equations and its auxiliary equations could be united as

$$\left[ \beta^* + (1 - \beta^*) \left\{ 1 + We^2(f'')^2 \right\}^{\frac{n-3}{2}} \left\{ 1 + nWe^2(f'')^2 \right\} \right] f''' + \frac{1}{2} f f'' + \xi \theta - M(f' - 1) = \xi(f'g' - gf''), \quad (9.25)$$

$$\frac{1}{Pr} \left( 1 + \frac{4}{3N_R} \right) \theta'' + \frac{1}{2} f \theta' = \xi(\phi f' - g\theta'), \quad (9.26)$$

$$\left[ \beta^* + (1 - \beta^*) \left\{ 1 + We^2(f'')^2 \right\}^{\frac{n-3}{2}} \left\{ 1 + nWe^2(f'')^2 \right\} \right] g''' + f''' \frac{1}{2} (1 - \beta^*) (n - 1) \left\{ 1 + We^2(f'')^2 \right\}^{\frac{n-5}{2}} We^2 f'' g'' \left\{ 3 + nWe^2(f'')^2 \right\} \left\{ 2We^2 f'' g'' + (f'')^2 \frac{\partial}{\partial \xi} (We^2) \right\} + \frac{1}{2} g f'' + \frac{1}{2} f g'' - M(g') + \theta + \xi \phi = \xi(g'g' - gg'') + (f'g' - gf''), \quad (9.27)$$

$$\frac{1}{Pr} \left( 1 + \frac{4}{3N_R} \right) \phi'' + \frac{1}{2} g \theta' + \frac{1}{2} f \phi' = f' \phi - \theta' g + \xi(g' \phi - g \phi'), \quad (9.28)$$

$$\begin{aligned}
& \left[ \beta^* + (1 - \beta^*) \left\{ 1 + We^2(f'')^2 \right\}^{\frac{n-3}{2}} \left\{ 1 + nWe^2(f'')^2 \right\} \right] z''' \\
& + g'''(1 - \beta^*) \left( \frac{n-3}{2} \right) \left\{ 1 + We^2(f'')^2 \right\}^{\frac{n-5}{2}} \left\{ 1 + nWe^2(f'')^2 \right\} \left\{ 2We^2 f'' g'' + (f'')^2 \frac{\partial}{\partial \xi}(We^2) \right\} \\
& \quad + g'''(1 - \beta^*) \left\{ 1 + We^2(f'')^2 \right\}^{\frac{n-3}{2}} \left\{ n(f'')^2 \frac{\partial}{\partial \xi}(We^2) + 2nWe^2 f'' g'' \right\} \\
& + g'''(1 - \beta^*) \left( \frac{n-3}{2} \right) \left\{ 1 + We^2(f'')^2 \right\}^{\frac{n-5}{2}} \left\{ 1 + nWe^2(f'')^2 \right\} \left\{ 2We^2 f'' g'' + (f'')^2 \frac{\partial}{\partial \xi}(We^2) \right\} \\
& \quad + f'''(1 - \beta^*) \left( \frac{n-3}{2} \right) \left( \frac{n-5}{2} \right) \left\{ 1 + We^2(f'')^2 \right\}^{\frac{n-7}{2}} \left\{ 2We^2 f'' g'' + (f'')^2 \frac{\partial}{\partial \xi}(We^2) \right\}^2 \\
& \quad \quad \quad \left\{ 1 + nWe^2(f'')^2 \right\} \\
& \quad + f'''(1 - \beta^*) \left( \frac{n-3}{2} \right) \left\{ 1 + We^2(f'')^2 \right\}^{\frac{n-5}{2}} n \left\{ 2We^2 f'' g'' + (f'')^2 \frac{\partial}{\partial \xi}(We^2) \right\}^2 \\
& \quad \quad + g'''(1 - \beta^*) \left\{ 1 + We^2(f'')^2 \right\}^{\frac{n-3}{2}} n \left\{ 2We^2 f'' g'' + (f'')^2 \frac{\partial}{\partial \xi}(We^2) \right\} \\
& \quad + f'''(1 - \beta^*) \left( \frac{n-3}{2} \right) \left\{ 1 + We^2(f'')^2 \right\}^{\frac{n-5}{2}} n \left\{ 2We^2 f'' g'' + (f'')^2 \frac{\partial}{\partial \xi}(We^2) \right\} \\
& \quad + f'''(1 - \beta^*) \left\{ 1 + We^2(f'')^2 \right\}^{\frac{n-3}{2}} (2n f'' g'' \frac{\partial}{\partial \xi}(We^2) + 2nWe^2 g'' g'' + 2nWe^2 f'' z'' \\
& + 2n f'' g'' \frac{\partial}{\partial \xi}(We^2) + n f''^2 \frac{\partial^2}{\partial \xi^2}(We^2)) + \frac{1}{2} z f'' + \frac{1}{2} g g'' + \frac{1}{2} g g'' + \frac{1}{2} f z'' - M z' + 2\phi + \xi \chi \\
& = f' z' + g'^2 - g'' g - f'' z + \xi [2g' z' - g'' z - z'' g], \tag{9.29}
\end{aligned}$$

$$\begin{aligned}
& \frac{1}{\text{Pr}} \left( 1 + \frac{4}{3N_R} \right) \chi'' + \frac{1}{2} (z\theta' + 2g\phi' + f\chi') = 2g'\phi - 2\phi'g \\
& \quad + f'\chi - \theta'z + \xi (\phi z' + g'\chi - z\phi' - g\chi'), \tag{9.30}
\end{aligned}$$

$$\begin{aligned}
f'(\xi, 0) &= 0, f(\xi, 0) = 2s - 2\xi g(\xi, 0), \theta(\xi, 0) = 1, \\
f'(\xi, \infty) &= 1, \theta(\xi, \infty) = 0, \\
g'(\xi, 0) &= 0, g(\xi, 0) + 2\xi z(\xi, 0) = 0, \varphi(\xi, 0) = 0, g'(\xi, \infty) = 0, \chi(\xi, 0) = 0 \\
z'(\xi, 0) &= 0, 5z(\xi, 0) + 2\xi \frac{\partial z}{\partial \xi}(\xi, 0) = 0, z'(\xi, \infty) = 0, \chi(\xi, \infty) = 0.
\end{aligned} \tag{9.31}$$

### 9.2.1 Parameters of Engineering Interest

The skin friction coefficient  $C_{fx}$  and Nusselt number  $Nu_x$  are defined as

$$C_{fx} = \frac{\tau_w}{\rho u_w^2(x)}, \quad Nu_x = \frac{xq_w}{k(T_w - T_\infty)} \tag{9.32}$$

where  $\tau_w$  is the surface shear stress and  $q_w$  the surface heat flux are given by

$$\begin{aligned}
\tau_w &= \mu_0 \left( \frac{\partial u}{\partial y} \right) \left[ \beta^* + (1 - \beta^*) \left\{ 1 + \Gamma^2 \left( \frac{\partial u}{\partial y} \right)^2 \right\}^{\frac{n-1}{2}} \right], \\
q_w &= -k \frac{\partial T}{\partial y} + q_r|_{z \rightarrow 0}.
\end{aligned} \tag{9.33}$$

Using Eq. (9.33), we obtain

$$\begin{aligned}
\text{Re}_x^{1/2} C_{fx} &= f''(\xi, 0) \left[ \beta^* + (1 - \beta^*) \left\{ 1 + We^2 \left( f''(\xi, 0) \right)^2 \right\}^{\frac{n-1}{2}} \right], \\
\text{Re}_x^{-1/2} Nu_x &= -\theta'(\xi, 0) \left[ 1 + \frac{4}{3N_R} \right],
\end{aligned} \tag{9.34}$$

where  $\text{Re}_x = \frac{U_0 x}{\nu_f}$  is the local Reynolds number.

## 9.3 Validation of Results and Discussion

Remembering the true objective to see the physical outcomes of the issue, numerical simulation of the heat transfer in the existence of thermal radiation and mixed convection is investigated. Also the stagnation point and MHD flow of a Carreau fluid in the presence of infinite shear rate viscosity is discovered. The local non-similar ordinary differential equations (9.26) to (9.31) are highly nonlinear in nature. Therefore, Eqs. (9.26) to (9.31) with related boundary conditions (9.32) have been solved numerically by utilizing `bvp4c` function in MATLAB. The outcomes which are given by plots are used to achieve the parametric study of the non-dimensional parameters, specifically magnetic parameter  $M$ , suction parameter  $s$ , Weissenberg number  $We$ , Prandtl number  $Pr$ , thermal radiation parameter  $N_R$ , viscosity ratio parameter  $\beta^*$  and buoyancy parameter  $\xi$ . For numerical inspection, we fixed the values to the governing parameters as  $We = 0.1$ ,  $n = 1.2$ ,  $\beta^* = 0.9$ ,  $s = 1$ ,  $Pr = 1$ ,  $N_R = 0.1$ ,  $M = 0.2$ ,  $A_1 = \frac{\partial}{\partial \xi}(We)$ ,  $A_2 = \frac{\partial^2}{\partial \xi^2}(We)$  and  $\xi = 0.1$ . We fixed these values in the whole study with  $A_1$  and  $A_2$  are treated as a constant in the present analysis. Moreover, the exactness of our numerical outcomes is checked with distributed outcomes by Minkowczyk and sparrow [94] and Mohammad *et al.* [95] for particular cases through **table 9.1**. And a decent agreement is accounted between these outcomes.

### 9.3.1 Flow and Thermal Characteristics

The effect of buoyancy parameter  $\xi$  on velocity  $f'(\eta)$  and temperature  $\theta(\eta)$  profiles in presence of thermal radiation  $Nr$  and magnetic field  $M$  are revealed in **Fig. 9.2**. It is important to note that the increasing values of buoyancy parameter  $\xi$  increase the fluid velocity  $f'(\eta)$  but in **Fig. 9.3** opposite behavior is observed for the temperature profile  $\theta(\eta)$ . Moreover momentum and thermal boundary layer thickness decline by enhancing the values of buoyancy parameter  $\xi$ . Since variation of  $\xi$  actually means a variation of distance along the surface. This demonstrates that an assisting buoyancy force acts like a favorable pressure gradient. The special effects of buoyancy force play a significant role on the movement of liquid by another consolidated porous medium.

**Fig. 9.4** illustrates the influence of  $\beta^*$  on dimensionless velocity profile  $f'(\eta)$  for a stable value of velocity ratio parameter  $\beta^*$  from 0.1 to 0.9. According to this, we observed that in



case of raise in velocity of the fluid is marked with increasing values of the viscosity ratio parameter  $\beta^*$ . Also increasing values of viscosity ratio parameter  $\beta^*$  decreases the boundary layer thickness. **Fig. 9.5** is deliberated to see the impact of  $\beta^*$  on temperature profile  $\theta(\eta)$ . It is noticed from this **Fig.** that increasing values of  $\beta^*$  decreased the temperature profile  $\theta(\eta)$ .

The influence of the magnetic parameter  $M$  on the velocity profile  $f'(\eta)$  has been portrayed in **Fig. 9.6**. It is clear from **Fig. 9.6** that the velocity profile  $f'(\eta)$  decreases for magnetic parameter  $M$ . Actually  $M$  indicates the ratio of electromagnetic force and the viscous force. Fixed numbers of  $M$  from 1 to 2 signifies the rise in the Lorentz force. This is a drag-like force that makes more protection from transport phenomenon and fluid velocity and in addition boundary layer thickness lessens.

**Figs. 9.7** and **9.8** illustrate the impact of suction parameter  $s$  on dimensionless velocity  $f'(\eta)$  and temperature profiles  $\theta(\eta)$  in the existence of thermal radiation  $N_R$  and buoyancy force  $\xi$  effects. In present **Figs.** solutions are noted for  $s = 1, 2, 3$  and  $4$ . We noticed that higher values of suction parameter  $s$  increases the velocity profile  $f'(\eta)$  and it is also observed that in **Fig. 9.8** higher values of  $s$  decrease the temperature profile  $\theta(\eta)$ . In the existence of suction, the hot fluid is pressed near the wall thus diminishes the thickness of thermal boundary layer and thins out the thermal boundary layers. Subsequently the nearness of suction diminishes the momentum boundary layer thickness yet expands the thermal boundary layer thickness.

The influence of Weissenberg number  $We$  on velocity profile  $f'(\eta)$  can be observed from **Fig. 9.9**. Here we taken only the assisting flow ( $\xi > 0$ ). This is clear from **Fig. 9.9** that velocity profile  $f'(\eta)$  decreases by increasing the Weissenberg number  $We$ . Actually, Weissenberg number  $We$  is the relation of relaxation time of the fluid and a certain process in which time growths the viscosity of liquid. Consequently, there is a decrease in the velocity of fluid .

The significance of thermal radiation  $N_R$  on the dimensionless velocity  $f'(\eta)$  and temperature profiles  $\theta(\eta)$  has been revealed in **Figs. 9.10** and **9.11** in the presence of magnetic field  $M$  and uniform suction  $s$ . It is noticed that the increasing values of thermal radiation  $N_R$  decreases the velocity profile  $f'(\eta)$ . Meanwhile it is noticed that temperature profile  $\theta(\eta)$  increases because of the fact that thermal radiation is linearly proportional with temperature, increase in  $N_R$  will enhances the temperature distribution in the boundary layer region.

**Fig. 9.12** represents the temperature profile  $\theta(\eta)$  for the Prandtl number  $Pr$ . Here tem-

perature decreases with the raise in  $Pr$ . Physically the lower Prandtl number shows fluids with high thermal conductivity and this generates thicker thermal boundary layer structures than that for the larger Prandtl number. **Figs. 9.13** and **9.14** are drawn to see the impact of different parameters on skin friction coefficient  $Re^{1/2}C_{fx}$ . In **Fig. 9.13**, boosting up the values of thermal radiation parameter  $N_R$ , the skin friction decreases. **Fig. 9.14** is drawn to see the behavior of Weissenberg number on the skin friction coefficient. An increase the Weissenberg number decreases the skin friction coefficient. **Fig. 9.15** shows the impact of thermal radiation parameter on Nusselt number. Rise in  $N_R$  increases the Nusselt number. Similarly in **Figs. 9.16** and **9.17** increasing values of Prandtl number  $Pr$  and buoyancy parameter  $\xi$  increase the Nusselt number  $Re^{-1/2}Nu_x$ .

**Table 9.2** is drawn to see the difference between the local similar solution and non similar solutions. By varying the different values of  $\xi$  and  $We$ , we get the values which provide us a clear difference for small values of  $\xi$  between similar and non similar solution.

**Table 9.3** displays the combined effects of the buoyancy parameter  $\xi$ , Weissenberg number  $We$ , magnetic parameter  $M$  and the  $\beta^*$  on the wall shear stress  $Re^{1/2}C_{fx}$ . The local skin friction is increased for the higher values of the buoyancy parameter  $\xi$  for both shear thinning and thickening fluids. Moreover, it is observed that the local Nusselt number  $Re^{-1/2}Nu_x$  is reduced with  $M$ , as the strong magnetic field reduces the extent of heat transfer rate.

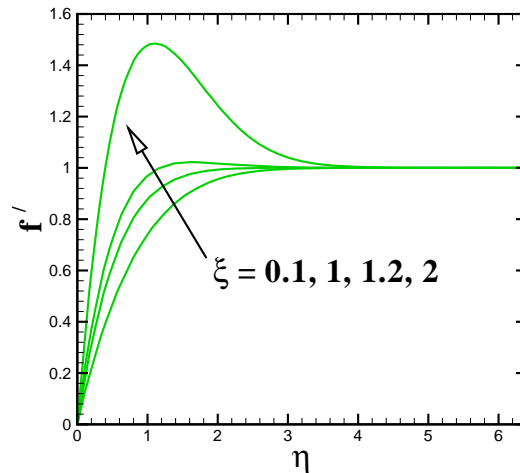


**Fig. 9.2:** Effect of  $\xi$  on  $f'(\eta)$

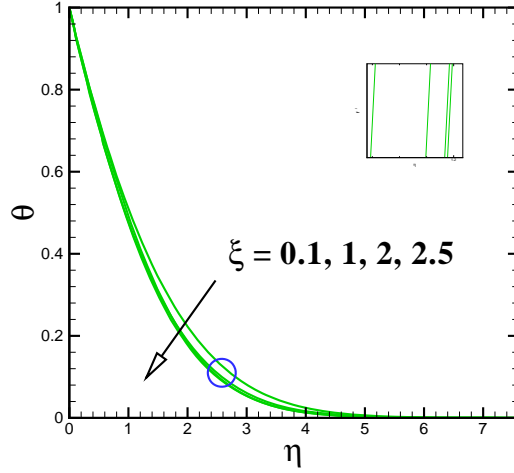


**Fig. 9.3:** Effect of  $\xi$  on  $\theta(\eta)$ .

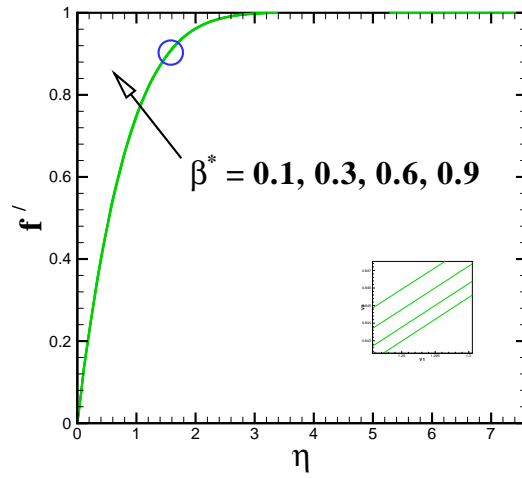


**Fig. 9.4:** Effect of  $\beta^*$  on  $f'(\eta)$ .

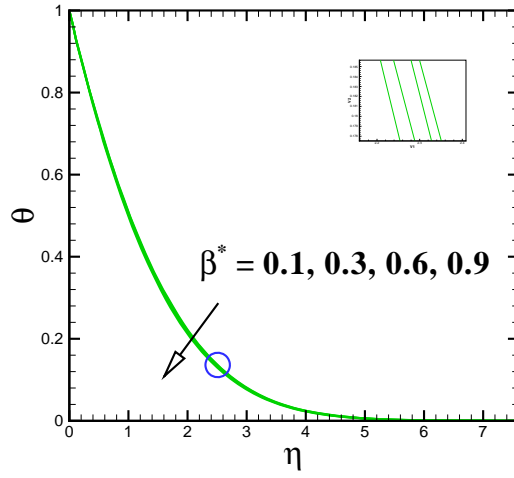


**Fig. 9.5:** Effect of  $\beta^*$  on the  $\theta(\eta)$ .

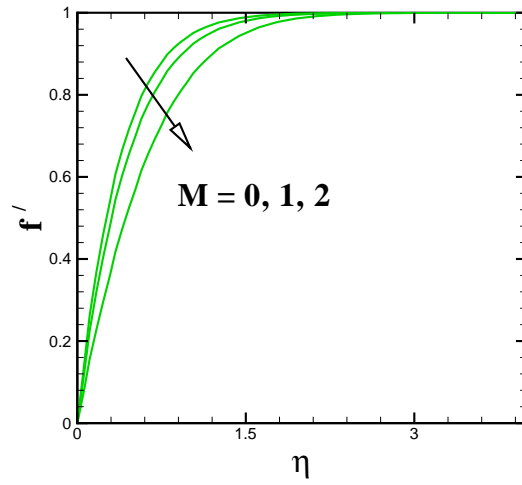


**Fig. 9.6:** Effect of  $M$  on  $f'(\eta)$ .

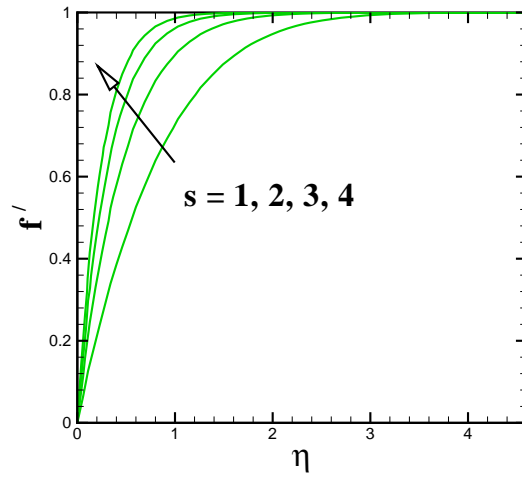


**Fig. 9.7:** Effect of  $s$  on  $f'(\eta)$ .

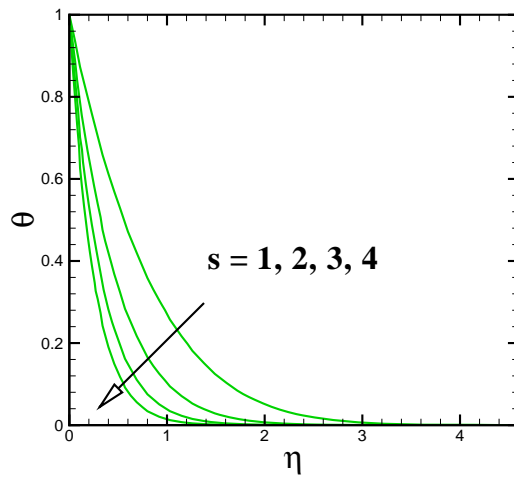


**Fig. 9.8:** Effect of  $s$  on  $\theta(\eta)$ .

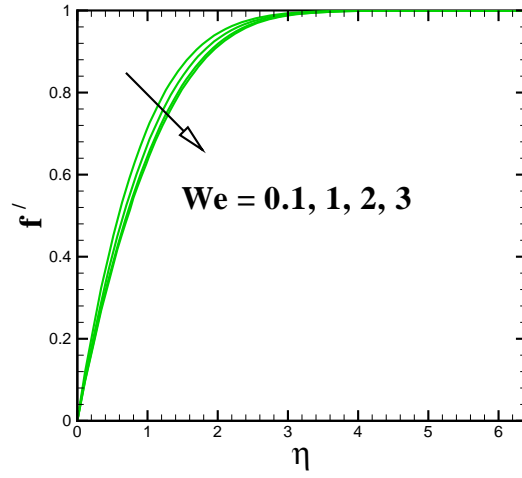


**Fig. 9.9:** Effect of  $We$  on  $f'(\eta)$ .

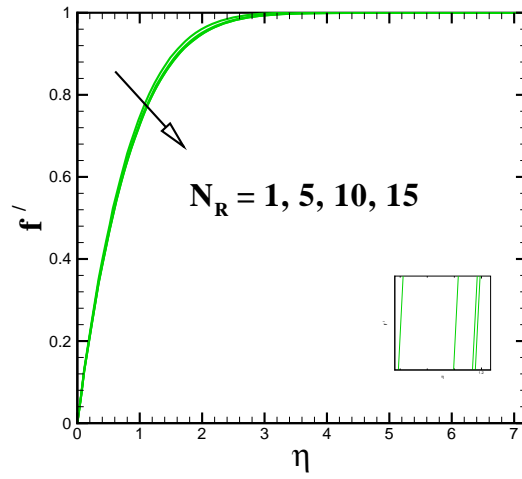


**Fig. 9.10:** Effect of  $N_R$  on  $f'(\eta)$ .

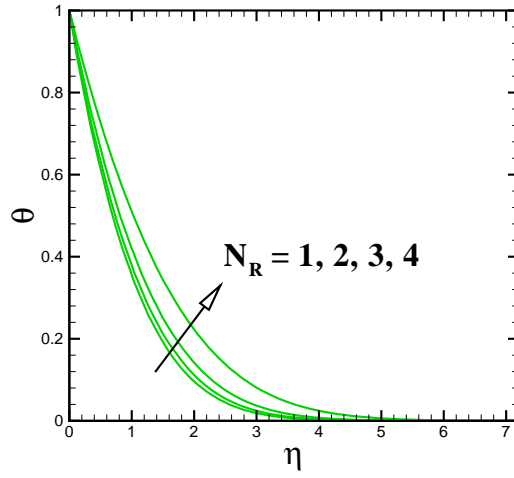


**Fig. 9.11:** Effect of  $N_R$  on  $\theta(\eta)$ .

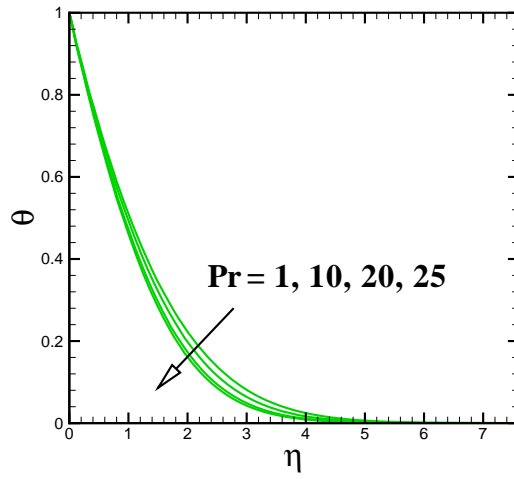


**Fig. 9.12:** Effect of  $Pr$  on  $\theta(\eta)$ .

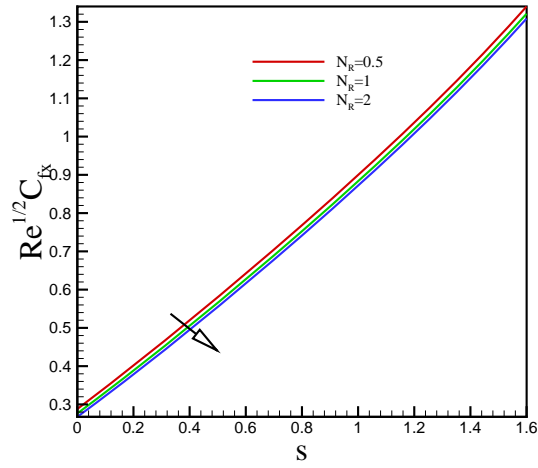


**Fig. 9.13:** Effect of  $N_R$  on the skin friction coefficient  $Re^{1/2}C_{f_x}$ .

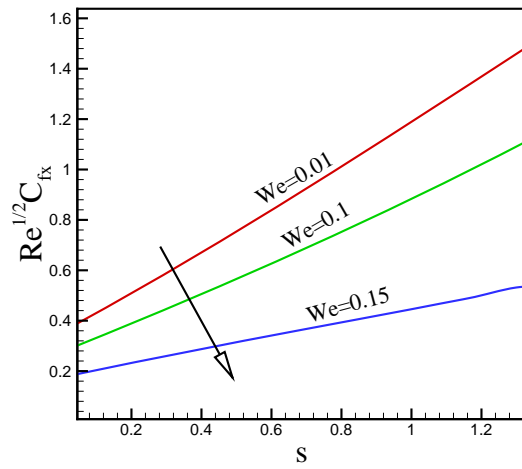


**Fig. 9.14:** Effect of  $We$  on the skin friction coefficient  $Re_x^{1/2}C_{f_x}$ .



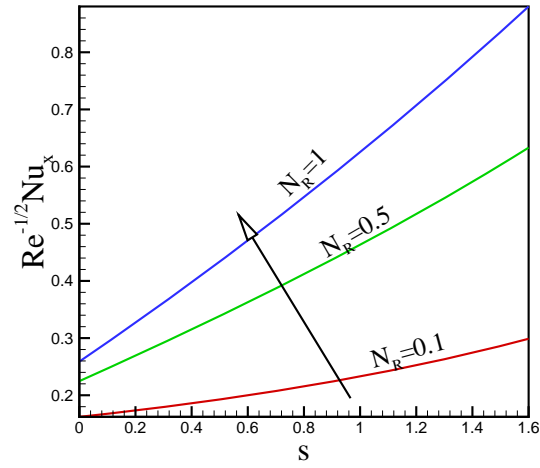


**Fig. 9.15:** Effect of thermal radiation parameter  $N_R$  on  $Re_x^{-1/2} Nu_x$ .

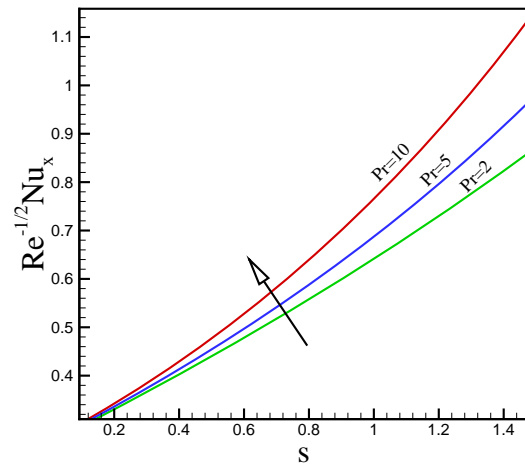


**Fig. 9.16:** Effect of  $Pr$  on the Nusselt number  $Re_x^{-1/2} Nu_x$ .

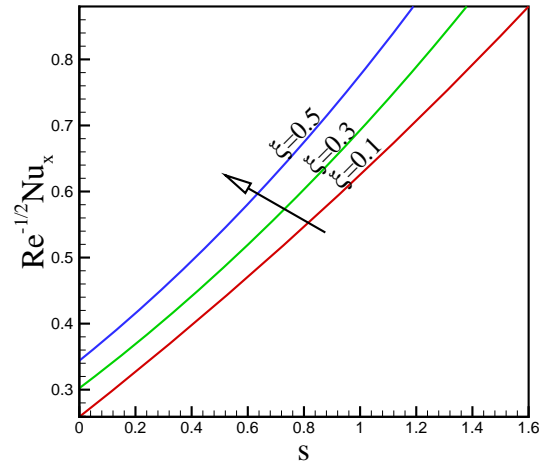


**Fig. 9.17:** Effect of  $\xi$  on the Nusselt number  $\text{Re}_x^{-1/2} Nu_x$ .

**Table 9.1:** Comparison of  $f''(\xi, 0)$  and  $-\theta'(\xi, 0)$  for different  $\xi$ , when  $We = 0$ ,  $n = 1$ ,  $\beta^* = 0$ ,  $s = 0$  and  $M = 0$ .

$\xi$	Minkowczyk and Sparrow [94]		Mohammad <i>et.al</i> [95]		Present analysis	
	$f''(\xi, 0)$	$-\theta'(\xi, 0)$	$f''(\xi, 0)$	$-\theta'(\xi, 0)$	$f''(\xi, 0)$	$-\theta'(\xi, 0)$
0	0.33206	0.29268	0.3320573	0.2926804	0.336152	0.2926804
0.4	0.73916	0.35774	0.7391622	0.3577421	0.756096	0.393098
1	1.21795	0.41054	1.2179529	0.4105355	1.229612	0.439667
1.5	1.56566	0.44106	1.5656630	0.4410137	1.553340	0.465358
2.5	2.18819	0.48619	2.1881869	0.4861908	2.082919	0.500098
5.0	3.52696	0.56067	3.5269162	0.5606733	3.065828	0.548641
7.0	4.47647	0.60283	4.4764563	0.6028282	3.682789	0.571250

**Table 9.2:** Comparison of local similar and non-similar solutions.

$(\xi, We)$	$Re_x^{1/2} C_{fx}$	$Re_x^{1/2} C_{fx}$
	Local similar solution	Local non-similar solution
(0, 0.1)	0.3332	0.3322
(0.4, 0.2)	1.1296	0.7640
(1.0, 0.3)	2.4250	1.3031

**Table 9.3:** Surface drag force  $Re^{1/2}C_{fx}$  and heat transfer rate  $Re^{-1/2}Nu_x$  for different values of  $\beta^*$ ,  $M$ ,  $We$  and  $\xi$ , when  $Pr = 1$ ,  $s = 0.1$ ,  $n = 1.2$  and  $N_R = 0.1$

$\xi$	$M$	$We$	$\beta^*$	$Re_x^{1/2} C_{fx}$		$Re_x^{-1/2} Nu_x$	
				$n = 0.2$	$n = 1.2$	$n = 0.2$	$n = 1.2$
0	0.1	0.1	0.1	1.103666	1.097716	1.165848	1.165621
			0.2	1.235347	1.230015	1.180536	1.175999
			0.4	1.360804	1.357905	1.195692	1.185011
	0			1.420915	1.417158	1.198884	1.187337
			0.1	1.360804	1.357905	1.195692	1.185011
			0.2	1.296216	1.294104	1.192176	1.182400
	0.2	0.2		1.319936	1.288553	1.193129	1.182272
			0.4	1.424149	1.269513	1.196981	1.181784
			0.6	1.634509	1.245230	1.203404	1.181046
	0.2	0.1	0.1	1.296216	1.294104	1.192176	1.182400
			0.3	1.295788	1.294183	1.190420	1.182831
			0.9	1.294642	1.294428	1.185205	1.184127

## Chapter 10

# Conclusions and Future Research

This thesis studies the various types of boundary layer flows of a non-Newtonian fluid model in the presence of infinite shear rate viscosity. For this purpose, a detailed mathematical modeling of Carreau viscosity model in the presence of infinite shear rate viscosity for different geometries was performed. These formulation enabled us to solve and analyze the diverse features of this model in the presence of infinite shear rate viscosity. Additionally, the heat and mass transfer characteristics of Carreau fluid were also analyzed. Two numerical approaches namely RK-Fhelberg and Matlab built-in routine bvp4c were adopted to obtain solutions.

To conclude this thesis, we précis its main contributions and suggest a number of directions for further research.

### 10.1 Conclusions

In the current thesis, boundary layer flows with heat and mass transfer of the non-Newtonian Carreau fluid model were considered. Boundary layer equations for steady  $2D$  and  $3D$  Carreau fluid flows were derived in the presence of infinite shear rate viscosity. The governing nonlinear partial differential equations of the laminar boundary layer flows were converted into nonlinear ordinary differential equations using suitable transformations. The emerging leading non-linear equations have been solved numerically by means of Runge-Kutta Fhelberg and bvp4c methods. The obtained numerical results have been displayed graphically and some exciting features like, multiple solutions are also established. Basically numerical outcomes were obtained to depict

the characteristics of fluid velocity, temperature and concentration fields.

The following conclusions are drawn in this thesis:

- It was noted that the momentum and thermal boundary layers thicknesses were higher for shear thickening ( $n > 1$ ) fluid when compared with shear thinning fluid ( $0 < n < 1$ ).
- By uplifting the power-law index  $n$  in both shear thinning ( $0 < n < 1$ ) and shear thickening ( $n > 1$ ) fluids, a decrease in the skin friction coefficient was observed.
- By uplifting Weissenberg number  $We$ , the skin friction coefficient was decreased and Nusselt number was increased.
- The velocity distribution was decreased by increasing viscosity ratio parameter  $\beta^*$  for both hydro-magnetic and hydrodynamic flows and quite the opposite was true for temperature distribution.
- By increasing the wedge angle parameter  $\beta$ , a reduction was observed in the momentum and thermal boundary layer thicknesses.
- It was observed that by increasing the velocity ratio parameter  $\lambda$ , velocity profile was increased and opposite trend was noted in temperature profile.
- An amazing feature of present work is that for second solution of velocity, temperature and concentration showed a higher boundary layer thickness as compared to first solution.
- This investigation has explored that an enhancement in the magnetic parameter  $M$  showed a rise in temperature of the fluid while an opposite behavior was observed for the fluid velocity.
- The magnitude of local skin friction  $Re^{1/2}C_{fx}$  was improved by enhancing magnetic parameter  $M$ .
- It was important to observe that rate of heat transfer was increased due to the higher velocity slip parameter  $\delta_1$  and magnetic parameter  $M$  for both solutions.
- The outcomes indicate that the higher values of heat generation/absorption parameter  $\delta$  upraised the fluid temperature.

- It seems that the greater values of temperature ratio parameter  $\theta_w$  raised the rate of heat transfer.
- The momentum boundary layer thickness was increased by increasing Grashof number and viscosity ratio parameter.
- It is significant to observe that the rate of heat transfer was improved due to higher Grashof number  $Gr_1$  for both solutions.
- It is found that the nanoparticles concentration at the wall was raised by Grashof number  $Gr_1$  for both the first and second solutions.

## 10.2 Future Research Directions

There is a lot of freedom for further work with respect to this thesis. Inside this assemblage of work we have explored the numerical solutions and mathematical modelling for non-Newtonian Carreau fluid in the presence of infinite shear rate viscosity. In addition, we have studied theoretically, the qualities of heat and mass transfer to the Carreau fluid due to stretching/shrinking sheets. Absolutely there is a lot of work remaining in this exceptionally fascinating non-Newtonian fluid model. Here, we will list some but not all of the many possible extensions. Firstly, the choice of different geometries, like, flows over curved stretching surface, flows in channel, flows over rotating disk may also be future considerations. Additionally, a transient nature can be captured for such flows for Carreau fluid model. Secondly, it could be interesting to study the Carreau fluid flows with infinite shear rate viscosity via advance numerical schemes like finite volume or finite element methods etc.

# Bibliography

- [1] P.J. Carreau, Rheological equations from molecular network theories, *Trans. Soc. Rheol.*, **116** (1972) 99 – 127.
- [2] M.S. Tshehla, The flow of Carreau fluid down an incline with a free surface, *Int. J. Phys. Sci.*, **6** (2011) 3896 – 3910.
- [3] B.I. Olajuwon, Convection heat and mass transfer in a hydromagnetic Carreau fluid past a vertical porous plate in presence of thermal radiation and thermal diffusion, *Therm. Sci.*, **15** (2011) 241 – 252.
- [4] M.G. Reddy, P. Polarapu and S. Bandari, Effects of magnetic field and ohmic heating on viscous flow of a nanofluid towards a nonlinear permeable stretching sheet, *J. Nanofluids*, **5** (2016) 459 – 470.
- [5] Hashim and M. Khan, Critical values in flow patterns of Magneto-Carreau fluid over a circular cylinder with diffusion species: Multiple solutions, *J. Taiwan Inst. Chem. Eng.*, **77** (2017) 282 – 292.
- [6] I.L. Animasaun and I. Pop, Numerical exploration of a non-Newtonian Carreau fluid flow driven by catalytic surface reactions on an upper horizontal surface of a paraboloid of revolution, buoyancy and stretching at the free stream, *Alex. Eng. J.*, **56** (2017) 647 – 658.
- [7] T. Hayat, S. Qayyum, M. Waqas and B. Ahmed, Influence of thermal radiation and chemical reaction in mixed convection stagnation point flow of Carreau fluid, *Results Phys.*, **7** (2017) 4058 – 4064.



- [8] S. U. S. Choi and J. A. Eastman, Enhancing thermal conductivity of fluids with nanoparticles, *ASME Pub. Fed.*, **231** (1995) 99 – 106.
- [9] J. Buongiorno and L.W. Hu, Nanofluid coolants for advanced nuclear power plants, *Proceedings of ICAPP*, **5** (2005) 15 – 19.
- [10] K.V. Wong and O.D. Leon, Applications of nanofluids: Current and future, *Adv. Mech. Eng.*, **2010** (2010) 1 – 12.
- [11] T. Hayat, M. Waqas, A. Alsaedi and M. I. Khan, Radiative flow of micropolar nanofluid accounting thermophoresis and Brownian moment, *Int. J. Hydro. Energy*, **42** (2017) 16821 – 16833.
- [12] M.I. Khan, A. Kumar, T. Hayat, M. Waqas, R. Singh, Entropy generation in flow of Carreau nanofluid, *J. Mole. Liq.*, **278**, 15 (2019) 677 – 687.
- [13] J. Buongiorno, Convective transport in nanofluids, *ASME J. Heat Transf.*, **128** (2006) 240 – 250.
- [14] M.I. Khan, A. Alsaedi, S. Qayyum, T. Hayat, M.Imran Khan, Entropy generation optimization in flow of Prandtl Eyring nanofluid with binary chemical reaction and Arrhenius activation energy, *Colloids and Surfaces A: Phys. Eng. Asp.*, **570** 5 (2019) 117 – 126.
- [15] O. D. Makinde and A. Aziz, Boundary layer flow of a nanofluid past a stretching sheet with a convective boundary condition, *Int. J. Therm. Sci.*, **50** (2011) 1326 – 1332.
- [16] W. Ibrahim and O.D. Makinde, The effect of double stratification on boundary layer flow and heat transfer of nanofluid over a vertical plate, *Comput. Fluids*, **86** (2013) 433 – 441.
- [17] M. Sheikholeslami, S. Abelman and D.D. Ganji, Numerical simulation of MHD nanofluid flow and heat transfer considering viscous dissipation, *Int. J. Heat Mass Transf.*, **79** (2014) 212 – 222.
- [18] K.B. Pavlov, Magneto hydrodynamic flow of an incompressible viscous fluid caused by the deformation of a plane surface. *Magnetohydrodynamic*, **4** (1974) 146 – 147.

- [19] H.I. Andersson, MHD flow of a viscoelastic fluid past a stretching surface, *Acta Mech.*, **95** (1992) 227 – 230.
- [20] M. Khan, M. Irfan and W.A. Khan, Impact of nonlinear thermal radiation and gyrotactic microorganisms on the magneto-Burgers nanofluid, *Int J Mech Sci.*, **130** (2017) 375 – 382.
- [21] M. Waqas, M.I. Khan, T. Hayat and A. Alsaedi, Numerical simulation for magneto Carreau nanofluid model with thermal radiation: a revised model, *Comput. Meth. Appl. Mech. Eng.*, **324** (2017) 640 – 653.
- [22] M. Khan, A. Hussain, M.Y. Malik, T. Salahuddin and F. Khan, Boundary layer flow of MHD tangent hyperbolic nanofluid over a stretching sheet: a numerical investigation, *Results Phys.*, **7** (2017) 2837 – 2844.
- [23] BC. Sakiadis, Boundary layer behavior on continuous solid flat surfaces, *J. AICHE*, **7** (1961) 26 – 28.
- [24] L. Crane, Flow past a stretching plate, *Z Angew Math Phys.*, **21** (1970) 645 – 647.
- [25] R. Cortell, Effects of viscous dissipation and radiation on the thermal boundary layer over a nonlinearly stretching sheet, *Phys. Lett. A*, **372** (2008) 631 – 636.
- [26] V.R. Prasad, B.Vasu, O.A. Bég and R.D. Parshad, Thermal radiation effects on magneto-hydrodynamic free convection heat and mass transfer from a sphere in a variable porosity regime, *Comm. Nonlinear Sci. Numer. Simu.*, **17** (2012) 654 – 671.
- [27] M. Sheikholeslami, D.D. Ganji, M.Y. Javed and R. Ellahi, Effect of thermal radiation on magnetohydrodynamics nanofluid flow and heat transfer by means of two phase model, *J. Magn. Magn. Mater.*, **374** (2015) 36 – 43.
- [28] Y. Lin, B. Li, L. Zheng and G. Chen, Particle shape and radiation effects on Marangoni boundary layer flow and heat transfer of copper-water nanofluid driven by an exponential temperature, *Powd. Tech.*, **301** (2016) 379 – 386.
- [29] M. Atlas, R.Ul. Haq and T. Mekkaoui, Active and zero flux of nanoparticles between a squeezing channel with thermal radiation effects, *J. Mol. Liq.*, **223** (2016) 289 – 298.

- [30] Rashid, R.Ul. Haq and Q.M.A. Mdallal, Aligned magnetic field effects on water based metallic nanoparticles over a stretching sheet with PST and thermal radiation effects, *Physica E*, **89** (2017) 33 – 42.
- [31] M. Usman, T. Zubair, M. Hamid, R.Ul. Haq and W. Wang, Wavelets solution of MHD 3-D fluid flow in the presence of slip and thermal radiation effects, *Phys. Fluids*, **30** **023** **104(2018)**; doi: 10.1063/1.5016946.
- [32] F.A. Soomro, R.Ul. Haq and Q.M.A. Mdallal, Heat generation/absorption and nonlinear radiation effects on stagnation point flow of nanofluid along a moving surface, *Results Phys.*, **8** (2018) 404 – 414.
- [33] S. Mukhopadhyay, K. Bhattacharyya and G.C. Layek, Steady boundary layer flow and heat transfer over a porous moving plate in presence of thermal radiation, *Int. J. Heat Mass Transf.*, **54** (2011) 2751 – 2757.
- [34] R.B. Bird, C.F. Curtiss, R.C. Armstrong and O. Hassager, Dynamics of Polymeric Liquids, John Wiley and Sons Inc., *New York, USA*, (1987).
- [35] P.S. Gupta and A.S.Gupta, Heat and mass transfer on a stretching sheet with suction or blowing, *Canad. J. Chem. Eng.*, **55** (1977) 744 – 746.
- [36] L.E. Erickson, V.G. Fox and L.T. Fan, Heat and mass transfer on a moving continuous flat plate with suction or injection, *Am. Inst. Chem. Eng.*, **15** (1969) 327 – 333.
- [37] K. Vajravelu, Viscous flow over a nonlinearly stretching sheet, *Appl. Math. Comput.*, **124(3)** (2001) 281 – 288.
- [38] R. Cortell, Fluid flow and radiative nonlinear heat transfer over a stretching sheet, *J. King Saud Uni. Sci.*, **26** **(2)** (2014) 161 – 167.
- [39] R. Cortell, Viscous flow and heat transfer over a nonlinearly stretching sheet, *Appl. Math. Comput.*, **184** (2007) 864 – 873.
- [40] M. A. Hamad and M. Ferdows, Similarity solutions to viscous flow and heat transfer of nanofluid over nonlinearly stretching sheet, *Appl. Math. Mech. Eng.*, **33(7)** (2012) 923 – 930.

- [41] N.S. Akbar, S. Nadeem, R. Ul. Haq and S. Ye, MHD stagnation point flow of Carreau fluid toward a permeable shrinking sheet: dual solutions, *Ain Sha. Eng. J.*, **5** (2014) 1233–1239.
- [42] M. Khan, Hashim and A. Hafeez, A review on slip-flow and heat transfer performance of nanofluids from a permeable shrinking surface with thermal radiation: dual solutions, *Chem. Eng. Sci.*, **11** (2017) 1 – 11.
- [43] C. Sulochana, G.P. Ashwinkumar and N. Sandeep, Transpiration effect on stagnationpoint flow of a Carreau nanofluid in the presence of thermophoresis and Brownian motion, *Alex. Eng. J.*, **55(2)** (2016) 1151 – 1157.
- [44] C. Sulochana, G.P. Ashwinkumar and N. Sandeep, Joule heating effect on a continuously moving thin needle in MHD Sakiadis flow with thermophoresis and Brownian moment, *Eur. Phys. J. Plus*, **132** (2017) 387. [https://doi.org/ 10.1140/epjp/i2017-11633-3](https://doi.org/10.1140/epjp/i2017-11633-3).
- [45] C. Sulochana and S.P. Samrat, Unsteady MHD radiative flow of a nano liquid past a permeable stretching sheet: an analytical study, *J. Nanofluids*, **6(4)** (2017) 711 – 719(9).
- [46] C. Sulochana, S.P. Samrat and N. Sandeep, Thermal radiation effect on MHD nanofluid flow over a stretching sheet, *Int. J. Eng. Res. Africa*, **23** (2016) 89 – 102.
- [47] Hashim, M. Khan, A.S. Alshomrani and R.Ul. Haq, Investigation of dual solutions in flow of a non-Newtonian fluid with homogeneous-heterogeneous reactions: critical points, *Eur. J. Mech.*, **6(8)** (2018) 30 – 38.
- [48] Hashim, M. Khan and A.S. Alshomrani, Numerical simulation for flow and heat transfer to Carreau fluid with magnetic field effect: dual nature study, *J. Mag. magn. Mater*, **443** (2017) 13 – 21.
- [49] H. Schlichting, K. Gersten, Boundary Layer Theory, *Berlin: Springer-Verlag*; 2000.
- [50] L.G. Leal, Advanced transport phenomena: fluid mechanics and convective transport processes, New York: *Camb. Uni. Press*, 2007.
- [51] D.R. Hartree, On an equation occurring in Falkner and Skan’s approximate treatment of the equations of the boundary layer, *Proc. Camb. Philos. Soc.*, **33** (1937) 223 – 239.

- [52] K.A. Yih, Uniform suction/blowing effect on forced convection about a wedge: uniform heat flux, *Acta Mech.*, **128** (1998) 173 – 181.
- [53] A. Ishaq, R. Nazar and I. Pop, MHD Boundary-layer flow of a micropolar fluid past a wedge with variable wall temperature, *Acta Mech.*, **196** (2008) 75 – 86.
- [54] C.S.K. Raju and N. Sandeep, Falkner-Skan flow of a magnetic-Carreau fluid past a wedge in the presence of cross diffusion effects, *Eur. Phys. J. Plus*, **131** (2016) 267.
- [55] C.S.K. Raju and N. Sandeep, Nonlinear radiative magnetohydrodynamic Falkner-Skan flow of Casson fluid over a wedge, *Alex. Eng. J.*, **55** (2016) 2045 – 2054.
- [56] M. Khan and M. Azam, Unsteady heat and mass transfer mechanisms in MHD Carreau nano fluid flow, *J. Mol. Liq.*, **225** (2017) 554 – 562.
- [57] M. Khan and M. Azam, On unsteady Falkner-Skan flow of MHD Carreau nanofluid past a static/moving wedge with convective surface condition, *J. Mol. Liq.*, **230** (2017) 48 – 58.
- [58] K.R. Rajagopal, A.S Gupta and T.Y. Na, A note on the Falkner-Skan flows of a non-Newtonian fluid, *Int. J. Non Linear Mech.*, **18(4)** (1982) 313 – 320.
- [59] B.L. Kuo, Application of the differential transformation method to the solutions of Falkner-Skan wedge flow, *Acta Mech.*, **164** (2003) 161 – 174.
- [60] M. Khan and Hashim, Boundary layer flow and heat transfer to Carreau fluid over a nonlinear stretching sheet, *AIP Adv.*, **5** (2016) 101203.
- [61] M. Khan and Hashim, Impact of heat transfer analysis on Carreau fluid flow past a static/moving wedge, *Therm. Sci.*, 2016 : 169.
- [62] K. Hiemenz, Die Grenzschicht an einem in den gleichförmigen Flüssigkeitsstrom eingetauchten geraden Kreiszyylinder, *Ding Polym J.*, (1911) 321.
- [63] R. Nazar, N. Amin, D. Filip and I. Pop, Stagnation point flow of a micropolar fluid towards a stretching sheet, *Int. J. Non Linear Mech.*, **39** (2004) 1227 – 1235.
- [64] M. Farooq, M. I. Khan, M. Waqas and T. Hayat, MHD stagnation point flow of viscoelastic nanofluid with nonlinear radiation effects, *J. Mol. Liq.*, **221** (2016) 1097 – 1103.

- [65] R. Cortell, Heat transfer in a fluid through a porous medium over a permeable stretching surface with thermal radiation and variable thermal conductivity, *Can. J. Chem. Eng.*, **90**(5) (2012) 1347 – 1355.
- [66] K. Khellaf and G. Lauriat, Numerical study of heat transfer in a non-Newtonian Carreau fluid between rotating concentric vertical cylinders, *J. Non-Newtonian Fluid Mech.*, **89** (2000) 45 – 61.
- [67] M. S. Tshehla, The flow of Carreau fluid down an inclined with a free surface, *Int. J. Phys. Sci.*, **6** (2011) 3896 – 3910.
- [68] F. M. Abbasi, T. Hayat and A. Alsaedi, Numerical analysis for MHD peristaltic transport of Carreau-Yasuda fluid in a curved channel with Hall effects, *J. Magn. Magn. Mater.*, **382** (2015) 104 – 110.
- [69] E.M. Sparrow, H. Quack and C. J. Boerner, Local non-similarity boundary layer solutions, *AIAA J.*, **8** (21) (1970) 1936 – 1942.
- [70] I. Muhaimin, R. Kandasamy, P. Loganathan and P. P. Arasu, Local non-similarity solution for the impact of the buoyancy force on heat and mass transfer in a flow over a porous wedge with a heat source in the presence of suction/injection, *J. App. Mech. Tech. Phy.*, **53** (2012) 231 – 241.
- [71] T. S. Chen, Parabolic system local non similarity method in handbook of numerical heat transfer, *Wiley-interscience, New York*, (1988).
- [72] M. Massoudi, Local non-similarity solutions for the flow of a non- newtonian fluid over a wedge, *Int. J. non-lin. Mech.*, **36** (2001) 961 – 976.
- [73] L.F. Shampine, I. Gladwell and S. Thompson, Solving ODEs with MATLAB, (1st Edn.), *Cambridge University Press, Cambridge*, (2003)
- [74] R. Sajjad, T. Hayat, R. Ellahi, T. Muhammad and Alsaedi A, Stagnation-point flow of second grade nanofluid towards a nonlinear stretching surface with variable thickness, *Results Phys.*, **7** (2017) 2821 – 2830.

- [75] T. Hayat, R. Sajjad, R. Ellahi, T. Muhammad and B. Ahmad, Numerical study for Darcy-Forchheimer flow due to a curved stretching surface with Cattaneo-Christov heat flux and homogeneous-heterogeneous reactions, *Results Phys.*, **7** (2017) 2886 – 2892.
- [76] R. Ellahi, E. Shivanian, S. Abbasbandy and T. Hayat, Numerical study of magnetohydrodynamics generalized Couette flow of Eyring-Powell fluid with heat transfer and slip condition, *Int. J. Numer. Math. Heat Fluid Flow*, **26(5)** (2016) 1433 – 1445.
- [77] Hashim and M. Khan, A revised model to analyze the heat and mass transfer mechanisms in the flow of Carreau nanofluids, *Int. J. Heat Mass Transf.*, **103** (2016) 291 – 297.
- [78] S. Rosseland, Astrophysik und Atom-Theoretische Grundlagen, *Springer Verlag*, (1931) 41 – 44.
- [79] A. Shahzad and R. Ali, Approximate analytic solution for magneto-hydrodynamic flow of a non-Newtonian fluid over a vertical stretching sheet, *Canad. J. Appl. Sci.*, **2(1)** (2012) 202 – 215.
- [80] T. R. Mahapatra and A. G. Gupta, Heat transfer in stagnation point flow towards a stretching sheet, *Heat Mass Transf.*, **38** (2002) 517 – 521.
- [81] R. Nazar, N. Amin, D. Filip and I. Pop, Unsteady boundary layer flow in the region of the stagnation point on a stretching sheet, *Int. J. Eng. Sci.*, **42** (2004) 1241 – 1253.
- [82] A. Ishak, R. Nazr and I. Pop, Mixed convection boundary layers in the stagnation-point flow toward a stretching vertical sheet, *Meccanica*, **41** (2006) 509 – 518.
- [83] W. A. Khan and I. Pop, Boundary-layer flow of a nanofluid past a stretching sheet, *Int. J. Heat Mass Transf.*, **53** (2010) 2477 – 2483.
- [84] C. Y. Wang, Free convection on a vertical stretching surface, *J. Appl. Math. Mech. (ZAMM)*, **69** (1989) 418 – 420.
- [85] R. S. R. Gorla and I. Sidawi, Free convection on a vertical stretching surface with suction and blowing, *Appl. Sci. Res.*, **52** (1994) 247 – 257.

- [86] W. A. Khan, M. Irfan and M. Khan, An improved heat conduction and mass diffusion models for rotating flow of an Oldroyd-B fluid, *Results Phy.*, **7** (2017) 3583 – 3589.
- [87] C. Y. Wang, Stagnation flow towards a shrinking sheet, *Int. J. Nonlinear. Mech.*, **43** (2008) 377 – 382.
- [88] N. A. Yacob and A. Ishak, Stagnation point flow towards a stretching/shrinking sheet in a micropolar fluid with a convective surface boundary condition, *Transport Phenomena, Can. J. Chem. Eng.*, **90** (2012) 621 – 626.
- [89] R. S. R. Gorla and B. J. Gireesha, Dual solutions for stagnation-point flow and convective heat transfer of a Williamson nanofluid past a stretching/shrinking sheet, *Heat Mass Transf.*, **52** (2016) 1153 – 1162.
- [90] P. D. Ariel, The three-dimensional flow past a stretching sheet and the homotopy, *Comput. Math. Appl.*, **54** (2017) 920 – 925.
- [91] T. Hayat, I. Ullah, T. Muhammad, A. Alsaedi and S. A. Shehzad, Three-dimensional flow of powell-Eyring nanofluid with heat and mass flux boundary conditions, *Chin. J. Phy.*, **25** (7) (2016) 074701.
- [92] M. Khan, M. Irfan, W. A. Khan and A.S. Alshomrani, A new modeling for 3D Carreau fluid flow considering nonlinear thermal radiation, *Results Phy.*, **7** (2017) 2692 – 2704.
- [93] E. M. Sparrow and H. S. Yu, Local non-similarity thermal boundary layer solutions, *ASME J.*, **93** (4) (1971) 328 – 334.
- [94] W. J. Minkowycz and E. M. Sparrow, Numerical solution scheme for local nonsimilarity boundary layer analysis, *Numer. Heat Transf.*, **1** (1978) 69 – 85.
- [95] R. Mohamad, R. Kandasamy and M. Ismoen, Local non-similarity solution for MHD mixed convection flow of a nanofluid past a permeable vertical plate in the presence of thermal radiation effects, *Appl. Comput. Math.*, **4**(6) (2015).
- [96] I. Lashgari, J.O. Pralits, First instability of the flow of shear-thinning and shear-thickening fluids past a circular cylinder, *J. Fluid Mech.*, **701** (2012) 201 – 227.



Turnitin Originality Report

numerical study of carreau fluid with infinite shear rate viscosity  
From DRSM (DRSML)

by Humara Sardar . 

- Processed on 28-Jan-2020 10:13 PKT
- ID: 1247537096
- Word Count: 32166

Similarity Index  
19%  
Similarity by Source

Internet Sources:  
9%  
Publications:  
14%  
Student Papers:  
12%

*Handwritten signature and date:*  
30/01/2020  
Focal person (Turnitin)  
Quaid-i-Azam University  
Islamabad

*Handwritten signature:* Masood Khan  
PROFESSOR  
Department of Mathematics  
Quaid-i-Azam University  
Islamabad

**sources:**

- 1 1% match (Internet from 12-Dec-2019)  
<https://www.science.gov/topicpages/s/solving+fluid+flow.html>
- 2 1% match (publications)  
Hashim, Masood Khan. "Critical values in flow patterns of Magneto-Carreau fluid over a circular cylinder with diffusion species: Multiple solutions", Journal of the Taiwan Institute of Chemical Engineers, 2017
- 3 1% match (publications)  
Hashim, Masood Khan, Ali Saleh Alshomrani. "Numerical simulation for flow and heat transfer to Carreau fluid with magnetic field effect: Dual nature study", Journal of Magnetism and Magnetic Materials, 2017
- 4 1% match (publications)  
Hashim, Masood Khan, Noor Ul Huda, Amir Hamid. "Non-linear radiative heat transfer analysis during the flow of Carreau nanofluid due to wedge-geometry: A revised model", International Journal of Heat and Mass Transfer, 2019
- 5 1% match (publications)  
Masood Khan, Muhammad Azam. "Unsteady heat and mass transfer mechanisms in MHD Carreau nanofluid flow", Journal of Molecular Liquids, 2017
- 6 1% match (publications)  
Masood Khan, Hashim, Abdul Hafeez. "A review on slip-flow and heat transfer performance of nanofluids from a permeable shrinking surface with thermal radiation: Dual solutions", Chemical Engineering Science, 2017
- 7 1% match (publications)  
Hashim, Masood Khan. "A revised model to analyze the heat and mass transfer mechanisms in the flow of Carreau nanofluids", International Journal of Heat and Mass Transfer, 2016
- 8 1% match (publications)  
Masood Khan, Muhammad Azam, Asif Munir. "On unsteady Falkner-Skan flow of MHD Carreau nanofluid past a stationary wedge with convective surface condition", Journal of Molecular Liquids, 2017
- 9 1% match (student papers from 14-May-2018)  
Submitted to Higher Education Commission Pakistan on 2018-05-14
- 10 < 1% match (student papers from 06-Jun-2018)  
Submitted to Higher Education Commission Pakistan on 2018-06-06
- 11 < 1% match (student papers from 02-Jan-2015)  
Submitted to Higher Education Commission Pakistan on 2015-01-02
- 12 < 1% match (publications)  
Hashim, Masood Khan, Ali Saleh Alshomrani, Rizwan Ul Haq. "Investigation of dual solutions in flow of a non-Newtonian fluid with homogeneous-heterogeneous reactions: Critical points", European Journal of Mechanics - B/Fluids, 2018